Wireless Surgical Capsule Robots for the Gastrointestinal Tract

Towards small scale therapeutic functions without on-board computation

Kaan Esendag

School of Electrical and Electronic Engineering
(Formerly Department of Automatic Control and Systems Engineering)
University of Sheffield

This dissertation is submitted for the degree of
Doctor of Philosophy

March 2025

Declaration

I, Kaan Esendag, confirm that the Thesis is my own work. I am aware of the University's Guidance on the Use of Unfair Means (www.sheffield.ac.uk/ssid/unfair-means). This work has not previously been presented for an award at this, or any other, university.

Kaan Esendag
March 2025

Abstract

Capsule robots provide an alternative route of entry to the gastrointestinal tract with minimal discomfort to patients. There are many examples of therapeutic capsules, but a gap exists in their capability in carrying out complex surgical functions such as manipulation in a suitable capsule size. There are two major factors for that limit the size of capsules; small scale actuators and on-board computation and communication required to control them. Controlling soft actuation wirelessly with an on-board pneumatic source of pressure could help with miniaturisation of efficient small scale actuators due to their scalability. An untethered robotic capsule that can provide volumetric expansion using a chemical reaction without on-board electronic components was designed along with a theoretical model for predicting the inflation behaviour. The expansion is based on the reaction between chemicals that are safe for ingestion, operated with thermal input provided by alternating magnetic fields from outside the body. Additionally, a new amplifier design that can deliver power to simple receiver circuits in parallel was presented. This allows the control of a wireless capsule that can use the electrical power for applications such as heating a target location, powering small motors bidirectionally and turn on LEDs without the use of a microcontroller. The design was tested for up to 6 addressable components, and an analysis on the limitations of this approach has been carried out. An example design of a capsule robot capable of anchoring itself to the intestinal tissues, use its manipulator arm to target a specific location and heat the location to patch wounds, or destroy pathogens or cancer cells was presented. Together, the wireless soft actuator and the wireless powering method should benefit further miniaturisation of therapeutic capsule robots capable of more complex in-vivo surgical functionality.

Table of contents

List of figures

List of tables

Chapter 1

Introduction

1.1 Background

Gastrointestinal (GI) related diseases have a high morbidity and mortality rates, with colorectal cancer being the second most common cause of deaths by cancer [10, 11]. Many advances have been made in the field of medical robotics from laparoscopic surgery robots, to active catheters for improved minimally invasive GI operations, to fully untethered solutions like capsule robots. Capsule robots have the unique ability to carry out operations without any incision at all, but the current commercially available capsule robots are only used for GI inspection [12–15]. There are many examples of capsules in active development to add therapeutic functions like active drug delivery [10, 16–22], sampling [1, 2, 23–26], anchoring [27–29], balloon expansion applications for anchoring [30], stopping haemostasis [31], obesity treatment [4], prostate treatment [32], dilation of intestinal strictures [33] and improve visuals during surgical operations [34, 35]. The key problem in improving the functionality of capsule robot is the lack of small and efficient actuators [1], as well as energy density and size efficiency of batteries [10]. This results in a capsule size outside the limitations of sizes allowed to be self administered without assistance or anaesthetics applied. There are two key areas that might help reduce the size of therapeutic capsules and allow higher degree of complexity to the operations that may be carried out with them. One is a method of wirelessly controlling on-board pneumatic sources [36] as electrochemical approach for soft robotics may prove to be a good scalable solution to small actuators [37]. The second problem is in the wireless control itself, as even though Wireless Power Transfer (WPT) can provide an unlimited supply of power [35] to the capsule, the capsule still needs a separate data transfer method for controlling actuation which could lead to larger capsule dimensions [38–40]. A method of control that does not require a microcontroller or data transfer but can still achieve addressable actuation of multiple components may solve this issue and work well with scalable small scale actuators.

1.2 Aim

As a result of this study, the concept of a novel electronics-free volume-changing capsule device using a mechanism of wirelessly regulating a chemical reaction to control the volume of produced gas has been developed. The simulation of physical interactions that lead to the inflation and deflation of the capsule that was validated with a comparison to the measured results from the experiments provide a good platform for development of capsules using wireless soft actuators for medical procedures. To address the problem of microcontroller-less solutions to small scale actuator control, a new modular amplifier circuit called the Poly-Sinusoidal Resonance Generator (PSRG) that can generate multiple sinusoidal magnetic fields at different frequencies, achieving Parallel Wireless Power Transfer (P-WPT) has been developed. It has been shown that up to 6 addressable components can be controlled independently and concurrently using the PSRG system. The Transmission (Tx) and Receiver (Rx) side analysis of WPT using the PSRG, a range of Tx coils and a range of Rx circuits for various powering applications such as heating up a Surface-Mount Device (SMD) Resistor, lighting up an LED, powering a motor with bidirectional control has been tested. The analysis highlights the limitations of the new approach and provides guidelines for developing capsules. A capsule robot design within endoscopic size requirements (11 mm diameter) that shows how an ingestible surgical robot can use the 6 frequencies for a robot to navigate to the site of surgery, anchor to the tissue, and use its manipulator and heater for a cauterization application in the gastrointestinal system has been presented as an example. Together, the two contributions may give rise to small scale therapeutic capsule robots capable of carrying out more complex surgical functions.

1.3 Thesis Structure

The thesis has been written in a thesis by publication format where Chapter 2 is a general literature review, Chapter 3 is a published journal paper converted to a single column thesis format, Chapter 4 is an unpublished work written in a standard journal paper structure, and Chapter 5 is a general conclusion. In the list of publications below, all publications due to work undertaken during the PhD have been included, but only the first author papers appear in the thesis where the entire contents of both of the works were conducted by myself. The second author paper mainly contains work done by the first author, where I advised the project in methodology and helped to carry out experiments, the abstracts contain overlapping information, and in the fourth author paper, my contributions have redundant information due to a similar magnetic induction system being used in Chapter 3.

1.4 List of Publications

First Author Journal Papers:

- **Kaan Esendag**, Mark E. McAlindon, Daniela Rus, Shuhei Miyashita and Dana D. Damian, "A Chemical Reaction Driven Untethered Volume Changing Robotic Capsule for Tissue Dilation", Transactions on Medical Robotics and Bionics, 20 September 2024. (Thesis Chapter 3)
- "Addressable Parallel Wireless Power Transfer for Capsule Robots". (Thesis Chapter 4, Unpublished)

Second Author:

- Bella Boyd, **Kaan Esendag**, Liu Du, Shuhei Miyashita, Dana Damian, "A Wirelessly Powered Robotic Capsule Chain for Gut Microbiota Sampling". (Unpublished)

Abstracts:

- **Kaan Esendag**, Mark McAlindon, Daniela Rus, Shuhei Miyashita and Dana Damian, Development of an Untethered Inflatable Capsule Robot for Stricture Dilation - a Preliminary Study, Hamlyn Symposium, 2023. (Accepted and Presented)
- Bella Boyd, **Kaan Esendag**, Shuhei Miyashita and Dana D. Damian, Development of a Near-Field Wireless Power Transfer System for Controlling Electronic Motors within Capsule Endoscopes, Hamlyn Symposium 2024. (Accepted)

Fourth Author:

- Jialun Liu, Xiao Chen, Quentin Lahondes, **Kaan Esendag**, Dana Damian, Shuhei Miyashita, Origami Robot Self-folding by Magnetic Induction, 2022 IEEE/RSJ International Conference on Intelligent Robots and Systems (IROS), pp 2519 - 2525.

Chapter 2

Literature Review

2.1 Overview

Gastrointestinal (GI) related diseases have a high morbidity rate [10], including colorectal cancer, which is the second most common cause of death in both sexes, resulting in a high mortality rate [11]. An open surgery is carried out by a surgeon if a high degree of access is necessary for the procedure, but it is the most invasive method out of all the options. An alternative method to surgical procedures in the GI tract can be performed with laparoscopic instruments, which is relatively less invasive to open surgeries, but the patient still needs to be put under general anaesthetic. The last two decades has seen rise in usage of surgical robots to assist minimally invasive surgeries [41], providing no difference between open surgery while causing less blood loss [42]. The operation times are longer, but earlier discharge time from hospitals make up for it in the impact to hospital resources. Even though cost to benefit ratio of robotic assisted minimally invasive surgery is high [43], general purpose robotic surgery machines are still very expensive compared to single task robotic tools, therefore less accessible to low-income parts of the human population. Additionally, regardless of how innovative the surgical robots get, they still need re-training of staff to be operational [44].

Endoscopy provides a less invasive method of access to the GI system through the natural orifices, requiring no incision and optionally some local anaesthetic applied. Endoscopic procedures include active inspection, microbiota sampling, biopsy, treatment for inflammation, Crohn's Disease and polyp removal, which is well suited for early stage cancer treatment. Endoscopic procedures are also relatively quick where a colonoscopy inspection can take 20 minutes [45] and a surgical procedure like polyp removal can take 50 minutes [46]. Regardless of whether an endoscopy or colonoscopy is being carried out, the latter half of the small intestine is difficult to access. A double Balloon endoscopy is usually used to access these difficult to reach areas, but the duration required to carry out the procedure is longer [47] and general anaesthetics are needed, which can have complications and can be risky in some demographic groups [48].

Untethered capsule endoscopy is a good solution to be able to reach all parts of GI without any invasiveness or requirement for anaesthetic, but a gap exists between capabilities of traditional endoscopy and wireless capsules [49–51]. Most capsules currently available in public use are only used for inspection without a surgical function. Passive capsules may not reach all parts of intestine if the patient's peristalsis movement is slow and the capsule does not have a large enough battery on board [10], given that passive transit via peristalsis can take 0.5-1.5 hours in the stomach, 20-40 hours in the small intestine and 3-4 hours in the large intestine [14]. The longest time is spent in the small intestine, which can have a length of around 5 m and the crawling speed of a passive capsule navigating through peristalsis is around 1-2 cm/min [52]. A majority of the cases still require an endoscopy after the capsule inspection and mostly are used for pre-screening [10]. The biggest limiting factor for improving the capabilities of capsule robots is medical requirements such as the dimensions of the capsule.

Similar to endoscopic requirements of up to 11 mm diameter, the largest FDA approved capsule size commercially available is size 000, which is also 11 mm diameter and 26-28 mm length [10, 53]. The esophagus diameter is around 20-30 mm in diameter [52], which may allow larger capsules to be delivered with surgical assistance, but can be considered a choking hazard for self-administration. The small intestine diameter is roughly 25-30 mm [27] and large intestine diameter is around 48 mm [53], which should be considered when designing the capsule robot function. A larger capsule may be suitable for a colonoscopic procedure, but not endoscopic. The capsules should also be resistance to stomach acid, which can have a pH of 1-3.5 [14]. For active control of wireless capsules, the distance to the peritoneal cavity from neutral position, 30.9 mm [54], which should be considered as the minimum distance the capsule can be controlled from outside the body. For destroying cancer cells through hyperthermia, a temperature of 45 °C is needed to be applied [55, 56]. There are many challenges to be overcome before therapeutic capsules that can fulfil the robotic capsule surgeon concept can be commercially available [57][58].

2.2 Capsule Robots

2.2.1 Overview

There are commercially available wireless capsules like PillCam for small and large bowel inspection [12, 13], which are currently only for passive inspection. Capsules devices can be broken down into active and passive devices in two aspects; navigation and therapeutic functionality [14]. Devices that navigate passively will rely on peristalsis for locomotion, and passive devices in terms of functionality will rely on mechanism that do not require active control by the surgeon. One approach to active navigation is using a robotic arm assisted control of capsule robots that include a permanent magnet inside for tethered [59] or untethered [15] solutions, which could allow better visual control to the operator. Similar results for magnetic manipulation can be achieved using electromagnetic coil systems instead [60, 61]. Another option for active locomotion is using the electromechanical approach by including a set of motor-actuated clamping mechanisms that work in a sequence to crawl in the intestines [29, 62], or using a worm-like mechanism [63].

2.2.2 Drug Delivery

Drug delivery is a common field of capsule robot research due to the lack of site-specific administration of drugs with traditional capsules, which can be difficult to rely on passive dissolution of the capsule as peristalsis can vary from patient to patient [10]. A variety of straightforward, mechanical or magnetically driven mechanisms has been tested for capsule based drug delivery applications. A shape-programmable, bistable mechanism was tested where the magnetically driven mechanism collapses to release the drug [16]. Another capsule uses an energy stored in a capacitor to open a hatch to release the drug, triggered by a reed switch in the presence of an external permanent magnet outside the body [17]. One approach uses a state-switching mechanism that can wirelessly generate heat to trigger the release of drugs and also be used for hyperthermia [18]. A soft magnet based mechanism has been tested for drug delivery in addition to an inspection module and reported to be able to deliver a volume of 0.78 ml, which is 26% of a conventional capsule endoscopy [19]. For a more controlled approach, a magnetic piston has been developed that uses electromagnetic coils inside the capsule that can actuate a permanent magnet based piston to release the drug when powered from outside the body [20]. This capsule has been tested to release the drug in regular intervals for over 5 hours. Some therapeutic functions such as active monitoring of gut health status can be carried out without the need of actively moving mechanical parts, resulting in a small form factor [21]. The gastric resident capsule can wirelessly communicate to transmit diagnostic information from inside the GI tract and control delivery modules to administer drug over time depending on internal conditions [22]. Apart from antibiotics, helicobacter pylori (H. pylori) can be treated with visible light using Phototherapy [64]. A capsule with LEDs was developed for the treatment of H. pylori in the stomach, which although was shown to be effective, it required at least 3 capsules at the same time [65].

2.2.3 Sampling

Another therapeutic function that could benefit from targeted operation is sampling, as faeces sampling is the most common method, but lacks site-specific information, and an open surgery is invasive [66]. Avoiding cross-contamination is important for sampling for two reasons; to avoid contamination of the sampled contents with samples from other areas and to avoid spread of a diseases or pathogens, like cancer, from one area to others. The type of tool that should be developed for the capsule depends on the type of sampling that needs to be carried out. For microbiota sampling, a brush or an intake mechanism can be used to collect viscous intestinal fluids. One passive solution to microbiota sampling uses an osmotic capsule whose pump relies on the pressure differential for sample collection while a permanent magnet from outside the body is used to keep the capsule fixed at the target location [26]. Given that the capsule does not have active actuation mechanisms, the final design was small enough to fit inside a capsule size 00 with an enteric coating for protection against stomach acid. Another approach uses a Shape Memory Alloy (SMA) spring to open a sampling hatch with 800 mN of force. The source of heat for the actuation of the SMA is provided by a high drain current battery, driven by an IC controlled with a wireless module [25]. The capsule was tested to confirm that the sealing works and enough sample can be collected for analysis.

For biopsy, a sample of tissue can be acquired with a needle, gripper or cutter. A rotating cutter was used with a torsion spring with a rotating permanent magnet based mechanism to collect tissue samples [1]. A magnetically-driven biopsy gripper can be made with a gear set [23] or with an extending piston mechanism [24], but the gripper being directly attached to the gear set results in a very small reach area and the piston mechanism has to extend towards the target by 9 mm since the gripping motion is tied to the extension. A biopsy needle can be made with a purely magnet-driven mechanism where the magnetic force is used for navigation, and a gradient magnetic field is used to control the rotation of a biopsy needle that is used as a linear actuator to collect the sample and retract back [2]. In all the cases, the range of the sampling mechanism cannot be controlled due to a lack of manipulators, which means that capsule has to rely on being directly next to the sampling area where the entire capsule body needs to be controlled to do the sampling.

2.2.4 Anchoring

The capability of anchoring is also an important feature for robotic capsule to have. In the GI tract, the constant motion of peristalsis can make it difficult to carry out tasks that require precision, which anchoring can help alleviate this issue. Anchoring can be achieved using mechanical legs [27], which can also help with other functions such as visual feedback and drug release [28]. Potentially, robots that use a clamping mechanism [29] could be used to also anchor using the same mechanism as the locomotion is based on fixing the robot in place. Even though mechanical legs can achieve high anchoring forces, they are more prone to tearing the intestinal tissues due to the smaller surface area of the legs providing a greater pressure onto the tissue [27]. An alternative solution can be to use balloons instead that will evenly spread the pressure to the intestinal tissue. Balloons can be used for applications like controlling intestinal bleeding [31], dilation of prostate [32], intestinal stricture dilation [33], obesity treatment [4] and improve visual feedback to the surgeon during an operation [34, 35]. Since balloons need a pneumatic pressure source, they also need a method of on-board gas generation [36] which can be based on chemical reactions. A capsule robot for the treatment of haemostasis uses a wirelessly powered and controlled micromotor to pump an acid into a base to produce Carbon Dioxide (CO_2) gas. It was reported that the capsule was deemed effective in stopping the bleeding while providing a holding force of 1.46 N. It has also been shown that changing the outer texture of a balloon can improve the anchoring force, reporting a maximum of 2.1 N [30]. A ballooning capsule robot for the treatment of obesity also uses a chemical reaction as a basis of inflation but also introduces a deflation module to manually deflate the capsule [4]. Even though the maximum volume reached with this capsule is as high as 300 mL, and the deflation can take place within 10 seconds, the final capsule size ended up quite large with a diameter of 30 mm and a length of 80 mm.

2.2.5 Size Considerations

There are a range of commercially available wireless endoscopy capsules for inspection that are typically around 11 mm diameter, 26 mm length [67, 68], but can go up to 12 mm diameter and 32 mm length [10]. Most of these capsules are passive, some like ANKON can be magnetically navigated using a robot-arm assisted device, but all lack a therapeutic function outside of inspection. The type of therapeutic function and the degree of active actuation it requires has a direct relationship with the final size of the capsule. Table 2.1 highlights that capsules that has both visual feedback and therapeutic function does not fit into the capsule 000 dimensions. Individual inspection capsules and individual therapeutic capsules can be within single 000 capsule size, but not both at the same time, which means with the current technological limitations, they have to be deployed as separate capsules. One solution could be to make multiple capsules [69] that can be individually swallowed and self-assembled in the stomach [70], navigated in the intestinal tract without breaking formation [71], docked and undocked at will [72] and form joints as a part of a 2-Degree of Freedom (DOF) manipulator [3] for targeted therapeutic function with visual feedback. It

Table 2.1 Capsule Size and Therapeutic Function Comparison

Citation	**Diameter (mm)**	**Length (mm)**	**Visual Feedback**	**Therapeutic Function**	**Fits in 000**
[10, 67, 68]	$\leq$11	$\leq$28	Yes	Inspection (Commercially Available)	Yes
[1]	9	24	No	Cutter-Based Biopsy Sampling	Yes
[17]	9	26	No	Drug Delivery	Yes
[26]	<8.53	<23.3	No	Passive Microbiota Sampling	Yes
[22]	<11	<28	No	Diagnostic Monitoring and Drug Delivery	Yes
[65]	12	27	No	Photodynamic Therapy	No
[38]	14	31	No	Bidirectional Communication	No
[29]	14	46.8	Yes	Clamper-Based Locomotion and Inspection	No
[23]	13	32	Yes	Gripper-Based Biopsy Sampling	No
[24]	14	32	No (Reserved Space)	Gripper-Based Biopsy Sampling	No
[19]	12	33	Yes	Inspection and Drug Delivery	No
[20]	16	25	No	Drug Delivery	No
[28]	16	50	No (Reserved Space)	Anchoring and Drug Delivery	No
[4]	30	80	No	Balloon-Based Obesity Treatment	No
[31]	13	14,35,12	No	Balloon-Based Haemostasis Treatment	No
[34]	12	32	No	Balloon-Based Visual Improvement	No
[39]	26	26	Yes	Active Visual Inspection	No
[25]	12	45	No	Active Microbiota Sampling	No
[2]	15	32	No (Reserved Space)	Needle-Based Biopsy Sampling	No

should also be considered that as the number of components to be self-assembled increases, it becomes harder to correctly self-assemble the device and the multi-joint modelling becomes more difficult as the DOF increase [73]. Either way, lack of small and efficient actuators [1], as well as energy density and size efficiency of batteries [10] could be considered the main barrier in miniaturisation of capsule robots. As the scale of the robots get smaller, the accuracy and precision of the tools decreases [74], which is why more research needs to be carried out to improve mechanisms in the centi-to-millimetre scale.

2.3 Centi-to-millimetre Scale Mechanisms

2.3.1 Direct Magnetic Control

There are plenty of mechanisms in the centi-to-millimetre scale that can act as actuators including magnetic actuation, electromechanical actuation, electrothermal actuation and electrochemical actuation [10]. Direct magnetic force generated by an electromagnetic coil system [75–77] or a robotic arm assisted permanent magnet [78, 15] can be used to manipulate the rotation and position of capsule if a permanent magnet is included in the robot [60, 61]. If the capsule also has a magnetically-driven mechanism for a therapeutic function, the mechanism needs to be suitable to be used in conjunction with magnetic navigation [1, 23, 24, 79, 80]. The benefit of using purely magnetically-driven mechanism is that they are also scalable for further miniaturisation [1] as the fabrication and magnetic control methods improve. One of the important advantages of electromagnetic coil systems is that they can achieve more complex motion due to the fact that coils can be turned off, but permanent magnet based systems usually have a stronger magnetic field. Inclusion of a magnet also means that using a Hall-effect sensor array, the capsule's position can be localised [81] and navigated using a closed-loop control system [82]. There are other ways of localisation such as using a Radio Frequency (RF) receiver (Rx), but the GI tissue movements and non-uniform distance may prove challenging [58]. A Magnetic Resonance Imaging (MRI) machine can be used to localise a capsule robot [18], but it requires large magnetic fields and has limitations on the duration it can be used. Compared to RF, which can be used to transmit gyroscopic sensor data from the capsule, magnetic localisation cannot provide accurate rotational angle information, but it is unaffected by dielectric and frequency changes from tissues as magnetic permeability through the body does not change and can provide a higher accuracy of location [58]. The biggest limiting factor with magnetic navigation and magnetically-driven mechanisms is that magnetic field is a global stimulus. It acts on all devices in the working area which means it is difficult to achieve independent control or collaborative tasks between multiple robots [10]. If the capsule robot uses magnetism both for navigation and therapeutic function, then the robot needs to be carefully designed to either sequentially carry out the two tasks or use direct magnetic force for navigation and use a magnetic gradient for the mechanism [2].

2.3.2 Material Based Intelligence

Apart from magnetism, there are smart materials that may prove useful in the centi-to-millimetre scale actuation with electrical or thermal input. Electromechanical actuators, such as dielectric and piezoelectric actuators, are durable, have a fast response and are energy-efficient, but require high voltages to function while providing low force [37]. For example, a dielectric soft robot with a reconfigurable foot design requires voltages of around 5-8 kV [83]. For dielectric actuators, even what is considered low voltages can be as high as 300 V [84–86]. Piezoelectric actuators are similar to dielectric materials, but they can provide sub-micrometer precision at lower voltages [37, 8]. A curved piezoelectric structure can be used to create an insect-scale soft robot that can be operated at 8 V, but it was reported that for significant locomotion speed, higher voltages from 60 to 200 V are needed [87]. High voltages are still needed while providing a small range of motion [37, 8].

For controlling thermoresponsive materials, if you can supply electrical power, you can also supply heat through a resistive element through Joule heating [88]. For some materials, the Coefficient of Thermal Expansion (CTE) can be used as centi-to-millimetre scale actuators. CTE can be used as a reversible actuator, but they have limited bending angles and generate low forces [37]. When compared to dielectric actuators, CTE actuators have a fast actuation speed, requiring voltages as low as 2 V, but they require a high actuation temperature [86] which may not be suitable to be used in the body. Using silver nanowires (AgNW) and programmable distribution of heat, a soft caterpillar-inspired crawler was made that can be actuated using 10-30 mA, with a voltage range of 1-3 V and an actuation temperature of 45 °C [7], which is suitable for biomedical applications. The actuation time can be as low as 10 seconds if 30 mA is applied. Despite the advantages over dielectric materials, CTE based systems like Fibre bot which uses 4 thermally actuated wires as an active catheter, requires high temperatures of 80 °C for achieving good precision [8]. Most of these actuators are wired solutions [86, 8, 7], but it may be possible to implement them as untethered actuators using Wireless Power Transfer (WPT).

Another option of thermoresponsive materials that are suitable to be used as actuators are Shape Memory Materials (SMM) such as Shape Memory Polymers (SMP) and SMAs. SMMs are materials that can be shape-programmed under high temperatures by deforming the material into a fixed, pre-determined shape, which can be used as actuators under temperature changes [89]. There are many factors that affect the choice of SMM to be used as an actuator such as working temperature range, bending angle limit, torque, deformation ratio, actuator size, biocompatibility, magnetic field requirement, material fatigue and reversibility, which makes it hard to choose a single SMM for a biomedical robot actuator [89–91]. SMPs have higher shape deformability with a higher recoverable strain than SMAs [89, 91], but they require high deformation temperatures above 100 °C [88]. SMAs take longer to deform but can generate higher forces with a larger work capacity than SMPs [37]. Most important benefit of SMAs for being used as a robotic actuator is that they are reversible, while SMPs are usually not, and they require reprogramming between actuation cycles [37, 88, 91]. SMAs such as Nickel Titanium based ones are good for biomedical applications due to their excellent biocompatibility, but they permanently deform due to fatigue after multiple cycles which is not ideal to be used as robotic actuators [89]. There is an example of a reversible SMP, but it needs a temperature of 33-39 °C to shape change and 0 °C to reverse its shape [92]. SMMs results in environmental heating and the actuation has a delayed response due to the heating and cooling cycles [58]. A big challenge for using SMMs for biomedical applications is limitation that comes from the usable temperature range as the chosen SMM needs to not actuate at body temperature of 37 °C, but also the actuation temperature should not exceed the limits of cell necrosis of 45 °C to avoid tissue damage during actuation. There is only a very limited amount of SMAs that fits within this range, which majority of thermally activated SMAs do not fit criteria [90]. There are Magnetic SMAs (M-SMA), which under a specific working temperature, can be magnetically actuated instead of thermally, however they require large magnetic fields of around 1 T for actuation which may go beyond biomedical limits of <100 mT [90].

Poly(N-isopropylacrylamide-co-polyacrylamide) (PNIPAM) is a biocompatible [93] thermoresponsive hydrogel that can be used as an actuator by contracting due to dehydration under certain thermal conditions via releasing its water contents to the environment [94]. It can also reabsorb water from its environment as it cools down to expand, making it a reversible actuator. The transition temperature which is used for PNIPAM based actuators is called the lower critical solution temperature (LCST), which is usually between 30-35 °C [95], but it can be tuned to 40 °C while working in slightly acidic pH of 5.5 [96]. PNIPAM has been previously used in drug release and hyperthermia studies [93, 96, 97] by including the drug in the hydrogel and using its contraction to release the drug with the water. Relying on the environmental temperature for the actuation of PNIPAM results in a slow actuation time [98], but by embedding magnetic particles directly inside PNIPAM, heat can be generated directly inside PNIPAM [99]. This actuates PNIPAM faster and fully dehydrates it from the inside, resulting in a higher degree of contraction as when heated with environmental conditions, some water gets trapped inside. The de-actuation however cannot be controlled as it relies on passively cooling down [98] and addressability is hard to achieve with particle heating. Compared to other soft material actuators, hydrogels provide the slowest actuation speed and lowest force output amongst soft material actuators, and they need to be submerged in water for full reversible actuation and prevent the hydrogel from drying out, which limits robotic application potential [37].

Light can be used as source of actuation in applications such as self-folding polymer sheets [98, 100]. This would be impractical in the context of in-vivo medical applications as light cannot reach inside the body, but could be interesting to study their uses with wireless LED devices [101, 65].

2.3.3 Electrochemical Solutions

A potentially scalable solution could be the electrochemical approach to centi-to-millimetre scale actuators, where gas generation for pneumatics can be used to control soft elements on a robot [37]. A major challenge of soft robotics is that they require heavy, bulky and tethered sources of pneumatic pressure. There are a range of chemical reactions that can be used for generating a gas which becomes an on-board source of pneumatic pressure [36]. One option is using the reaction between citric acid [34] or acetic acid [31] and sodium bicarbonate, which produces CO_2 in gas form as a by-product, which can be used to inflate a balloon or a soft actuator. The chemical reaction could be triggered by removing the barrier between the two chemicals [4, 34] or a piston mechanism can be used to control the amount of one chemical being pumped into the other one to control the gas generation [31]. An electrically driven mechanism can be used to open a hatch for quick deflation [4] or wait for the actuator to deflate by itself as CO_2 gets absorbed into water to form carbonic acid over a long duration [102] without requiring any extra mechanism.

Electrolysis of water can also be used as a source of rapid gas generation, producing oxygen, which can be used as a reversible source of actuation [36, 37, 103]. Combined with a hydrogel, liquid metal electrodes can be used to make up a fully soft bubble actuator which uses a relatively low voltage of 15 V with an actuation speed of 14 seconds [103]. It could potentially be used reversibility if air vents are introduced and the hydrogel is submerged in water, but runs into the same limitations of hydrogels in biomedical applications.

Pneumatic pressure can also be generated by using the liquid-to-gas phase transition of low boiling point chemicals such as acetone or flourine-based engineered fluid Novec 7000 [37], which has a boiling point of 34 °C. Engineered fluids have been used previously to make artificial muscles [104], soft actuators [6], small pouches that can expand [105] and expanding intravascular capsules [5]. The heat can be generated in iron oxide particles distributed in the fluid under strong alternating magnetic fields [104, 105, 5] or with an Rx coil and WPT [6]. The soft actuator controlled with a Rx coil reported an actuation speed of 10 seconds when receiving a power of 1.33 W at a separation distance of 2 mm. A big challenge of using low boiling point fluids for transition is that they are not suitable to be used in the body if the boiling point is below the body temperature. Additionally, there is an extra challenge as more of the fluid transitions into a gas, the pressure inside increases which in turn increases the boiling point. The intravascular expanding capsule has reported that the boiling point has increased to 53 °C and can only keep inflated for up to 3 minutes [5]. Chemofluidic phase transition as a source of pneumatic pressure can have large energy densities [35, 5] and are easy to miniaturise, but they generally have a slow actuation speed [37], and it is difficult to control force with phase transition [5].

2.3.4 Structure Based Intelligence

Apart from advances made directly in the materials used for the robot, miniaturisation could also benefit from structure based mechanisms that could help in fabrication and control of centi-to-millimetre scale robots. Origami is the traditional art of folding paper to make 3D structures from flat-foldable structures. An advantage of flat foldability is that fabrication methods like photolithography can be used for fabricating microscale details on flat surfaces which can help decrease the scale of the robot [106]. Origami pattern generation is already a matured field with software like Origamizer that can use a tucking molecule design to generate a 2D flat foldable origami crease pattern from any given 3D model [107, 108]. The crease pattern can be designed to make continuos curved folds [109] and increasing the resolution of the pattern increases the accuracy of the generated shape[110]. The curve pattern of the origami can be generated to actively change the shape and therefore the function of the device [111]. If the robot is not made out of soft or foldable parts, any crease pattern can be converted into a rigid origami version by adding creases and removing panels from the design [112]. Rigid origami has already been shown to be effective in applications that require efficiently packed deployment size such as solar panels of satellites [113]. A limiting factor in using origami as a part of an actuator is that as the complexity of origami pattern increases, the computation needed to calculate the precise action necessary to control each fold also becomes harder [114]. Origami patterns can be auto generated and optimised through a genetic algorithm when given a fitness function, which can help optimise the generated structure for a specific actuation [115], which may help reduce the actuation complexity. Origami structures can be used to make metamaterials capable of shape, volume and stiffness control [116]. Using multiple units of cells, multi-DOF actuation can be achieved, which can be important for designing actuators for robotic joints. Origami structures have already seen uses in robotic applications such as creating a pop-up origami that is capable of multi-DOF manipulation from flat-foldable sheets [74] and an octopus-like origami arm design which is omnidirectional and magnetically controlled [117]. Origami can be made to self-fold using induction heating if copper is included as one of the flat layers [118]. It can be made degradable while also allowing robotics functions such as walking and swimming [60, 119]. Origami structures can also be paired well with centi-to-millimetre scale mechanisms such as SMAs to carry out tasks such as addressable self folding with Frequency Modulation (FM) and WPT [9, 120]. The same concept has been used to make a wireless small scale origami manipulator with 3 addressable components [121].

Similar to origami, Lamina Emergent Mechanisms (LEMs) are fabricated from planar materials [122]. They have motions that emerge out of the fabrication plane, providing compact and cost-effective devices, but the tasks are pre-determined at the fabrication stage and are tied to the fabrication process. Multilayer LEMs (MLEMs) can be used for achieving complex motions with a simple topology and low manufacturing cost while keeping a flat initial state, which can potentially be used for energy transform applications, converting electrical energy to thermal, then to mechanical energy [123]. For both origami and LEMs, repeated actuation may be a problem as the hinges of the creases are susceptible to damage [124]. The damage depends on the type of hinge used, but flexible hinges may be a solution.

A way to improve the use cases of structure based intelligence such as origami is by implementing technologies that can provide a form of embedded computation and sensing that can allow the structure to better interact with their environment [114]. Inkjet printing can be used to print electroactive tracks and carbon based electrothermal actuator that can self fold [125, 126]. Some electronic components can also be printed or made in a flexible thin-film form such as capacitors [127], transistors [125], matrix displays, microprocessors [128]. Mechanical memory can be embedded into origami design to perform bit operations, which is useful for embedded computation [129]. Origami structures can be used for creating resistors, capacitors and inductors, but the electronic characteristics are tied to the origami geometry which can change during actuation [130]. There is also flexible Printed Circuit Boards (PCBs), but they are prone to breaking or cracking under continuous actuation [131], which might not be favourable if they are meant to be part of an actuator. Thin-film electronics can also be made degradable, called transient electronics, using magnesium or magnesium oxide based components printed on silk [132]. The electronics can be wirelessly heated with a printed Rx coil and resistor, which dissolves the silk and oxidises the magnesium, which shows potential for in-vivo applications as magnesium oxide is safe for consumption [133].

Mixed with structure based intelligence, flexible electronics may provide a high degree of complexity in control of centi-to-millimetre scale biomedical robots.

2.4 Wireless Technologies

Many mechanisms in the centi-to-millimetre scale are either electrically or thermally controlled, which will need a method of wireless thermal generation and WPT techniques for untethered capsule robots. Heat can be generated using alternating magnetic fields in centimetre scale and above through eddy currents, in microscale through hysteresis and in nanoscale through Néel and Brownian relaxation [55], but this method is not addressable as all the particles in the vicinity will be heated. Since thermal energy can also be generated by resistive elements through joule heating with an electric current passing through [88], and can be made addressable through FM [9, 120], any improvements to WPT technologies should benefit both electroactive and thermoresponsive materials, which helps overcome energy challenges of robotics, especially in the centi-to-millimetre scale [134]. In the context of capsule robots, relying on batteries for power is considered a limiting factor for the duration that the capsule can be used for, on the quality of the visual feedback due to higher frame rate and resolution requiring more power, and also for including tools that consume additional power [10, 135]. Size limitations and battery technology cannot allow for inclusion of larger or higher energy density batteries on board, which is why WPT can be a good solution that can provide an unlimited supply of power [35]. A standard inspection capsule can have a power rating of 20 mW at 3 V, which can last 8-10 hours with a battery [58]. Some capsule robots however have shown up to 100-400 mW of power consumption, which is possible to be delivered using WPT systems [135, 35, 39]. There are a few methods of WPT suitable for in-vivo capsule applications. One of these methods is using Resonant Inductive Coupling (RIC) with Rx coil and a capacitor with a resonant frequency matched to the frequency of the applied magnetic field for maximum Power Transfer Efficiency (PTE) [136]. Additionally, RIC can also be used for sensing through the capacitive element of a sensor changing the resonant frequency [137]. This change can be detected from the included RF coil during in-vivo applications for diagnostic purposes during surgical operations any may even allow closed-loop control of surgical tools if included in a capsule robot. One of the drawbacks to RIC is that it is prone to parasitic elements affecting the resonant frequency such as patient's movements during operation as the body or the presence of inductive materials [35], which may affect the power delivery and require extra self-tuning circuits. Magnetic Resonant Coupling (MRC) is another WPT method that uses extra coils on the transmission (Tx) side and optionally on the Rx side as well, to create a stronger coupling between the Rx and Tx by strengthening the magnetic field [136, 138]. MRC can achieve higher PTEs compared to RIC and are less affected by misalignment conditions [138]. A 9 mm diameter Rx coil can receive 300 mW of power at a 70 mm separation distance using a 4 coil MRC setup [139]. Even though MRC can provide power at much larger distances compared to RIC, MRC usually requires higher operational frequencies that are harder to produce and need careful consideration of their Specific Absorption Rate (SAR) [136]. Apart from requiring more complex circuitry and optimisation variables on the Tx side, the Rx circuit might need more complex circuitry as well, especially if a 4 coil configuration is being used instead of 3, increasing the size requirements for on-board circuits. In either case, RIC and MRC are still the most suitable method for WPT for medical devices. When designing the Tx and Rx coil geometries, the WPT system can be optimised for maximum PTE [140], including for possible misalignment conditions [141]. Another solution to misalignment conditions is using 3D Rx coils [142–144] that can receive power in each rotation. They can be made into a size as small as 8 mm square [145], which should fit into a size 000 capsule, but the PTE of 3D coils decrease when one of the Rx coil is not in parallel with the Tx coil, because two diagonal Rx coils receive less power than one parallel Rx coil [142].

In most cases of WPT applications, a Class-E amplifier is used to supply the Tx coil with power due to its high efficiency [136]. Class-E amplifiers also need tuning and optimisation to adjust for the non-conducting gate voltages and to improve amplifier efficiency [146, 147]. Best efficiency can be achieved in zero voltage switching (ZVS) conditions, which can be reached by resonant frequency tuning the Tx side inductor as well [146]. If FM is being used for the application and the frequency of transmission needs to be actively changed, the capacitance needs to be actively switched as well, which is impractical in fast switching applications and can cause large voltage or current spikes in the circuitry. Another method is by adjusting the inductance which could be done with a saturable DC-feed inductor and can be digitally controlled. Using a resonant tank tuned class-E amplifier is also sensitive to parasitic elements like big metal objects around the surgical area or coil deformation can also affect the power transfer efficiency [143]. It was determined that 7 A through the Tx coil was enough to deliver power for a wireless endoscopy application, where the amplifier was provided with 120 V and the tuned resonant tank built-up a voltage of 4 kV.

Wireless power and data can be transferred at the same time by mixing two frequencies together in the same system [148] which has its own set of optimisation parameters as well [149]. The lower frequency acts as a carrier wave for power delivery, whereas the higher frequency wave acts as a binary form of communication through inducing noise, which is picked up on the receiver side and computed on the Rx side. The problem with on-board computation is that there needs to be extra space for communication and computation circuitry while also requiring additional power to be supplied to the rest of the functionality of the robot [40]. Bluetooth could provide communication for distance of up to 85 mm for in-vivo applications, but the PCB necessary to be present on board could be around 15 mm width and 40 mm height, which is outside capsule dimensions. A slightly smaller example of a Bluetooth module on board a capsule robot has a dimension of 11.6 mm length and 13.5 mm width, which is still outside the requirements [39]. Even without Bluetooth, an RF bidirectional communication circuitry could take up space that ends up with a capsule of 14 mm diameter and 31 mm length [38]. The diameter of the capsule is the biggest limiting factor as an active inspection capsule with camera feedback, LEDs and wireless communication can take up to 115 mA current and 2.5-3.3 V voltage consumption [39], which not only requires suitable circuitry to allow the functionality but also need space for a WPT Rx coil.

An alternative approach would be to use mechanisms that do not require computation and specific communication circuitry to be controlled, such as directly controlling SMA actuation with frequency matched Rx circuits and an FM WPT system to adjust the frequency being transmitted [9, 120, 121]. This method has only been shown to work up to 3 addressable components and addressability is only achieved here as SMA actuators have a delayed response [58], which is not comparable to the number of addressable components that can be achieved with digital computation. Superposition of multiple sine waves instead of FM is also possible to allow actuation at the same time, but it causes high peaks [121], which may be more difficult to produce. Multiple amplifiers and Tx coils could be used instead to create superposed magnetic fields, but this causes issues as each Tx coil will have mutual coupling between each other [150]. This is an issue for a resonant frequency based application because self-inductance of an inductor has a non-linear relationship with current, which means that the current passing through each Tx coil needs to be measured and actively tuned for the transmission of correct frequency, resulting in the complexity of the problem increasing with each added addressable component.

2.5 Conclusion

As summarised in Fig. 2.1 A, there is a range of options for performing surgical operations with varying degrees of invasiveness. Untethered capsule robots provides an alternative route of entry into the GI tract with minimal discomfort to the patient. Although most of the commercially available capsule robots are used for inspection, there is a range of therapeutic functions that can be found in the literature. The usual size of the capsule is correlated to the therapeutic function, as described in Fig. 2.1 B, where the more complex the function is, the

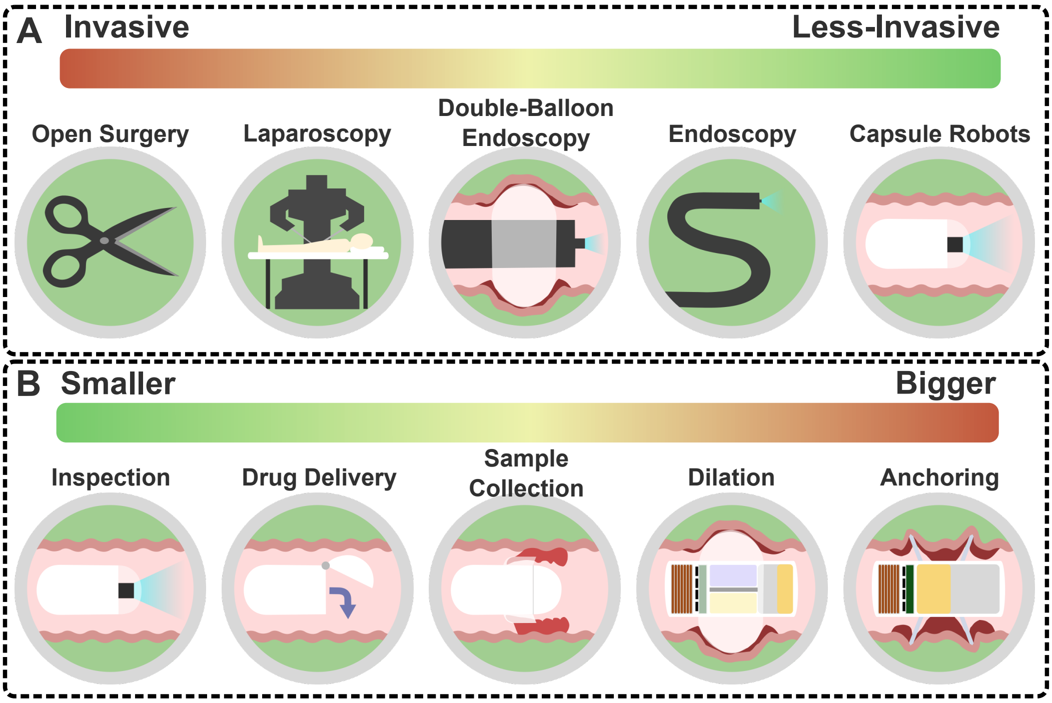

Fig. 2.1 Overview of capsule robots for the GI tract. (A) Shows a range of operations carried out in the GI tract in order of more to less invasive. (B) Shows a range of capsule robot applications in order of usual capsule size it can be achieved with.

bigger the usual size of the capsule. Capsules with mechanical movements that powered by electric motors seem to be the bigger capsules whereas inspection capsules with no moving parts or drug delivery capsules that rely on simple mechanisms tend to be the smallest.

Mechanisms whose function depends on magnetic force similar to the ones shown in Fig. 2.2 A and B can achieve a smaller size for a mechanical task due to the scalable nature of magnetism. Magnetic force can also be used to self-assemble multiple capsules into one, shown in Fig. 2.2 C, which may reduce the diameter of the capsule by splitting the internal components into multiple capsules that are ingested individually and self-assembled in the stomach. Even though magnetic force is useful for a single task and navigation, multiple mechanisms are difficult to control due to the magnetism being a global factor.

Pneumatic actuation may also be a good option that can be scalable and also useful for soft robotic applications for better tissue compliance in the GI tract. The source of pneumatic actuation may be a chemical reaction, but the release mechanism that relies on electromechanical components similar to Fig. 2.2 D may result in a large capsule size. An alternative approach is to use the liquid-to-gas boiling point transition to source the pneumatic actuation shown in Fig. 2.2 E, where the heat is provided by heating magnetite particles with an alternating magnetic field. However, this approach is not selective either given that the

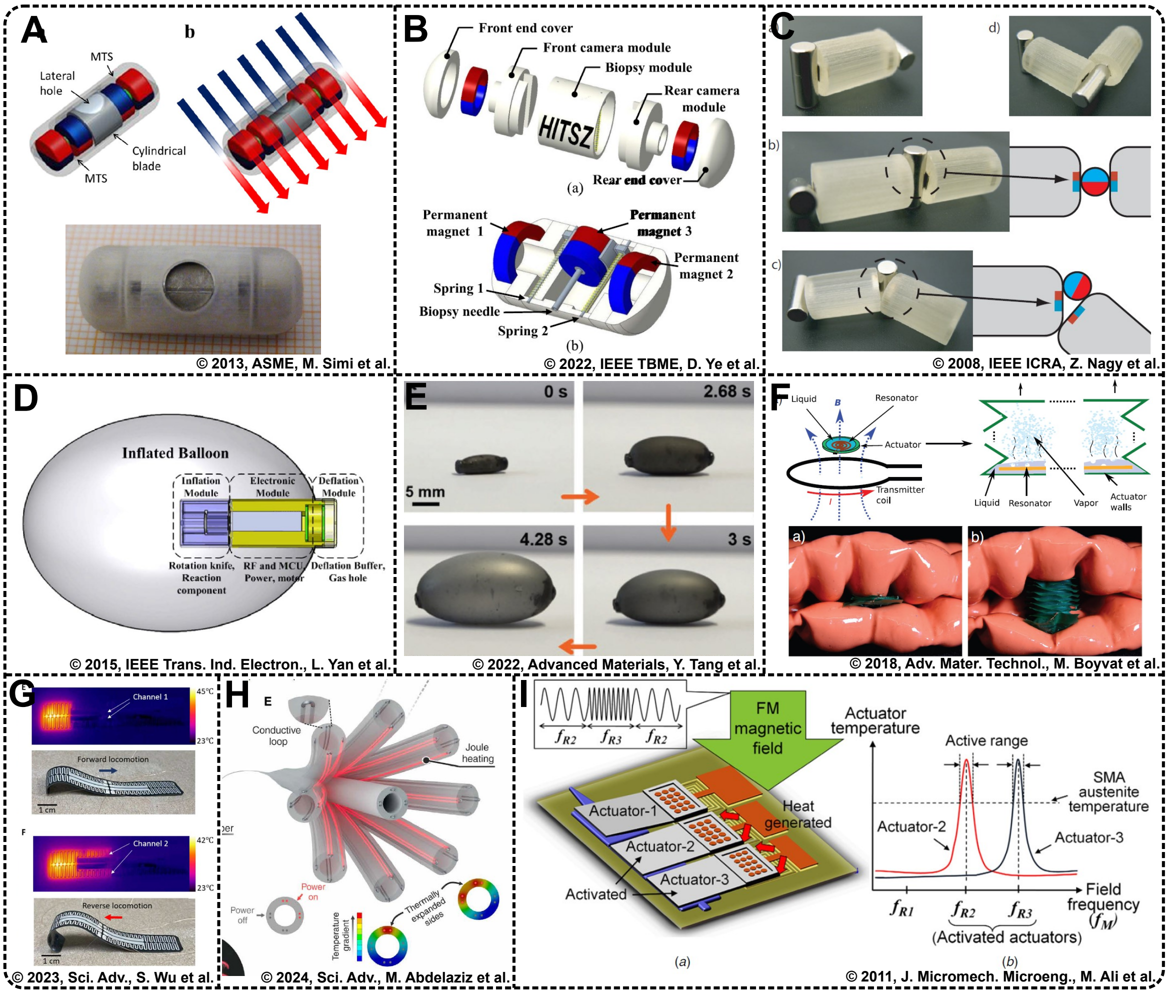

Fig. 2.2 Examples from the literature. (A) Magnetically actuated biopsy cutter [1]. (B) Magnetically actuated biopsy needle [2]. (C) Magnetic self-assembling capsules [3]. (D) Chemical reaction based inflating capsule [4]. (E) Liquid-gas transition based inflating capsule [5]. (F) Liquid-gas transition based inflation triggered by inductive coupling [6]. (G) CTE based caterpillar robot [7]. (H) CTE based precise surgical instrument [8]. (I) Selective inductive coupling with FM allowing addressable actuation of SMAs [9].

alternating magnetic field is also a global factor. Providing the heat with inductive coupling, as shown in Fig. 2.2 F, may enable addressability of a soft and scalable pneumatic actuation. One drawback of relying on the boiling point transition temperature is that it is difficult to control the force output of actuation. Using heat as a method of controlling the amount of chemicals released into a solution may be a good combination of the two directions.

Another approach with thermoresponsive control could be to use CTE. The traces can be programmable to control the heat distribution of the CTE element for robotic tasks, shown in Fig. 2.2 F, or multiple CTE elements may be used to make surgical instruments with high precision for targetted tasks, shown in Fig. 2.2 H. Both of these examples are wired, but WPT may enable untethered control.

RIC with FM enables multiple thermoresponsive components to be selectively controlled, shown in Fig. 2.2 I. This example uses the SMA actuator as part of the circuit, but since WPT can be converted into heat with any resistive element, it can be used to control other thermoresponsive mechanisms as well, including pneumatic actuation. One drawback of the FM approach is that even though it can allow addressability, the power transfer is not concurrent and independent. This means that only one component can be powered at a given time, limiting the power transfer capabilities.

To address this gap in literature, the first technical chapter of this thesis investigates a method of wireless pneumatic control using a dissolution medium for controlled release of chemicals, where the heat input is controlled with an alternating magnetic field outside the body. The second technical chapter investigates WPT with superposition using a new amplifier design, to allow concurrent and independent of RIC elements with a minimal electronics on-board. This could prove useful in closing the gap between capabilities of microcontroller-less solutions and digital computation, eventually leading to smaller scale mechanisms that can be used in therapeutic capsules. Eventually, combining the two technologies may lead to wireless control of centi-to-millimetre scale soft robots with multiple pneumatic actuators.

Chapter 3

Wireless Control of Chemical Reaction Driven Pneumatic Systems for Soft Robotics

Chapter source: Kaan Esendag, Mark E. McAlindon, Daniela Rus, Shuhei Miyashita and Dana D. Damian, "A Chemical Reaction Driven Untethered Volume Changing Robotic Capsule for Tissue Dilation", Transactions on Medical Robotics and Bionics, 20 September 2024.

3.1 Abstract

Robotic capsules provide an alternative route of entry to the gastrointestinal tract with minimal discomfort to patients. As capabilities of milli to micro robots progress, the potential of using robotic capsules not just for inspection, but for surgical procedures increase. To aid operations in the intestine, the capsule could be used to expand the site of surgery and anchoring to the intestinal walls to keep itself in place. This paper presents an untethered robotic capsule that can provide volumetric expansion using a chemical reaction without on-board electronic components. The expansion is based on the reaction between chemicals that are safe for ingestion, operated with magnetic fields and temperatures that are within safe limits. The capsule was able to expand greater than the diameter of the small intestine for 44 minutes and provided 0.27 N of anchoring force. A theoretical model of the reaction process was built and simulated to predict the behavior of the capsule expansion and validated through the experiments. The design and the simulation presented in this paper can be used for fabricating capsules to specific clinical needs. The work also opens up the possibility of

untethered technologies that are remotely and chemically programmed for in-vivo surgical applications.

3.2 Introduction

Robotic capsules provide alternative methods to minimally invasive procedures in the gastrointestinal tract such as endoscopy, colonoscopy and laparoscopy, which can further reduce the invasiveness. While the current state-of-the-art for robotic capsules fulfills the need for inspection [12], sample collection [2, 14] and targeted local drug administration [27, 68, 22, 97, 151], a gap still exists between the capabilities of robotic capsules and tethered surgical solutions [50, 49, 51]. Inclusion of small scale tools such as cutters [79], forceps [80], manipulators [74] and biopsy needles [2] in robotic capsules could enable untethered surgical procedures to be performed in the gastrointestinal tract. In order to use these tools in the small intestine, a capsule needs to dilate the site of surgery greater than the diameter of the small intestine (25-30 mm [27]), and anchor to the tissue for long periods of time as inspection can take around 20 minutes [45] and surgical procedures can take around 50 minutes [46].

As a method of dilation, robotic capsules featuring mechanical legs have been developed [28, 27]. The small contact surface area provided by the legs greatly increases the local pressure applied on the anchored tissue with the risk of tissue puncture. Capsules which dilate and maintain a compliant interface are safer in this regard. An example of an untethered inflatable ballooning mechanism is presented in [4], which uses a chemical reaction as its source of pressure, however little consideration is given to the controllability of the changing capsule volume. Moreover, inclusion of electronic components, motors or batteries generally results in large and overweight capsules. A completely electronics-free volume changing soft actuator was developed using the phase transition of low-boiling point liquids [104, 5], but the operation temperature goes beyond the limits of cell necrosis which is around 45 °C [56, 55] and the actuator can only be inflated for brief periods of time.

As contributions, this paper presents:

1. Concept of a novel electronics-free volume-changing capsule device using a mechanism of wirelessly regulating a chemical reaction to control the volume of produced gas.

2. Modeling of the chemical reaction process which causes the inflation and deflation of the capsule.

3. Validation of the performance in experiments and comparison with simulation results.

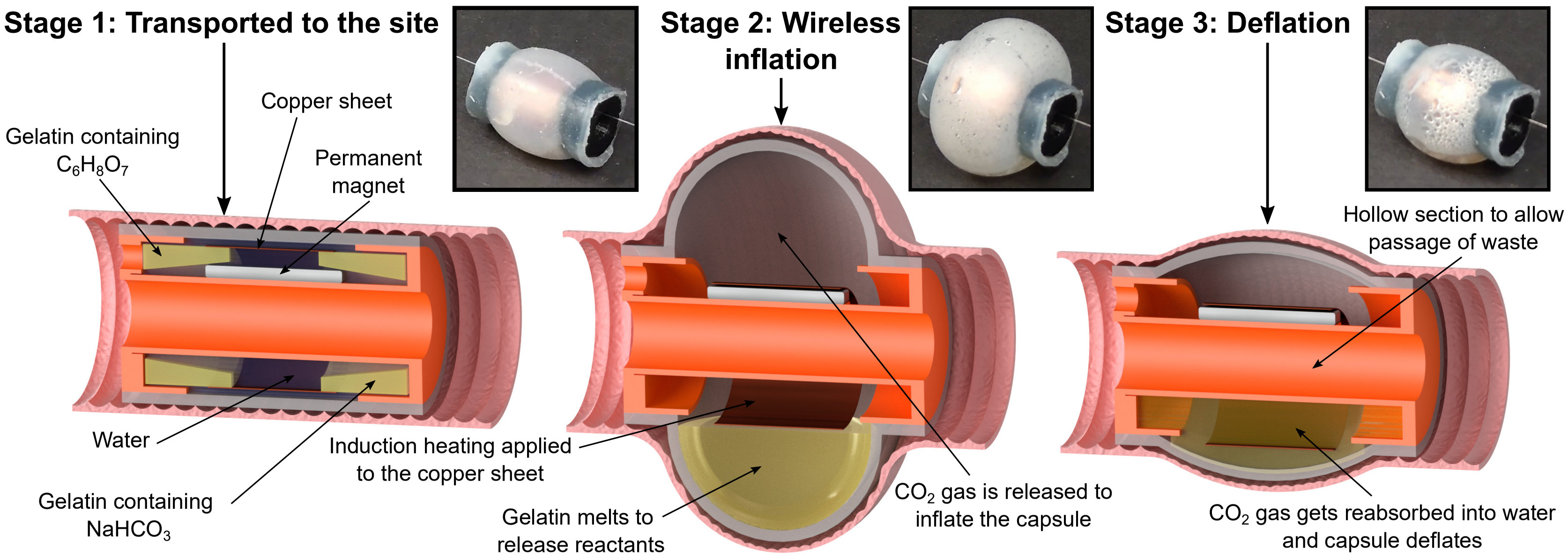

Fig. 3.1 CAD renders showing a cross-section view of the robotic capsule in a section of intestine, along with real images of the capsule. The concept diagram is broken down into three stages along a timeline. First the robotic capsule reaches the site of surgery, then induction heating is applied to control the actuation, the chemical reaction takes place to inflate the capsule, followed by the reabsorption of CO_2, deflating the capsule to leave the site of surgery.

3.3 Methods

3.3.1 Design Concept and Specification

The overview of the capsule operation is shown in Fig. 3.1. In stage 1, the capsule is navigated to the surgical site, using a magnet attached inside it. The capsule remote navigation was demonstrated using an Ankon AKC-1 [78] and an electromagnetic coil system. The capsule holds reactants for the gas-generating chemical reaction in gelatin rings, isolated from each other. The capsule also has a copper sheet wrapped around the gelatin rings and contains water which acts as a solvent. In stage 2, the capsule's inflation is wirelessly controlled through magnetic induction which generates thermal energy in the copper sheet and dissolves the gelatin. The release of reactants lead to the chemical reaction which produces carbon dioxide (CO_2) gas for capsule inflation. The reactants chosen for the chemical reaction are citric acid ($C_6H_8O_7$) and sodium bicarbonate ($NaHCO_3$), which are safe for consumption [152, 153]. The alternating magnetic field used in induction heating has a peak amplitude of 5 mT oscillating at 27 kHz which is considered to be low frequency and amplitude when compared with similar methods [104, 5, 136, 142]. The induction coil is located 4 cm below the capsule which is a similar distance compared to literature given that the peritoneal cavity from the neutral position is 30.9 mm [54, 77]. In stage 3, the capsule undergoes deflation. As the capsule cools down, the produced gas is absorbed into the water and the capsule deflates to its original volume. The inflation is controlled by a magnetic field below the Brezovich limit [55]. The proposed method hence provides a safer, novel and promising alternative for surgical in-vivo operations, especially those that require prolonged usage.

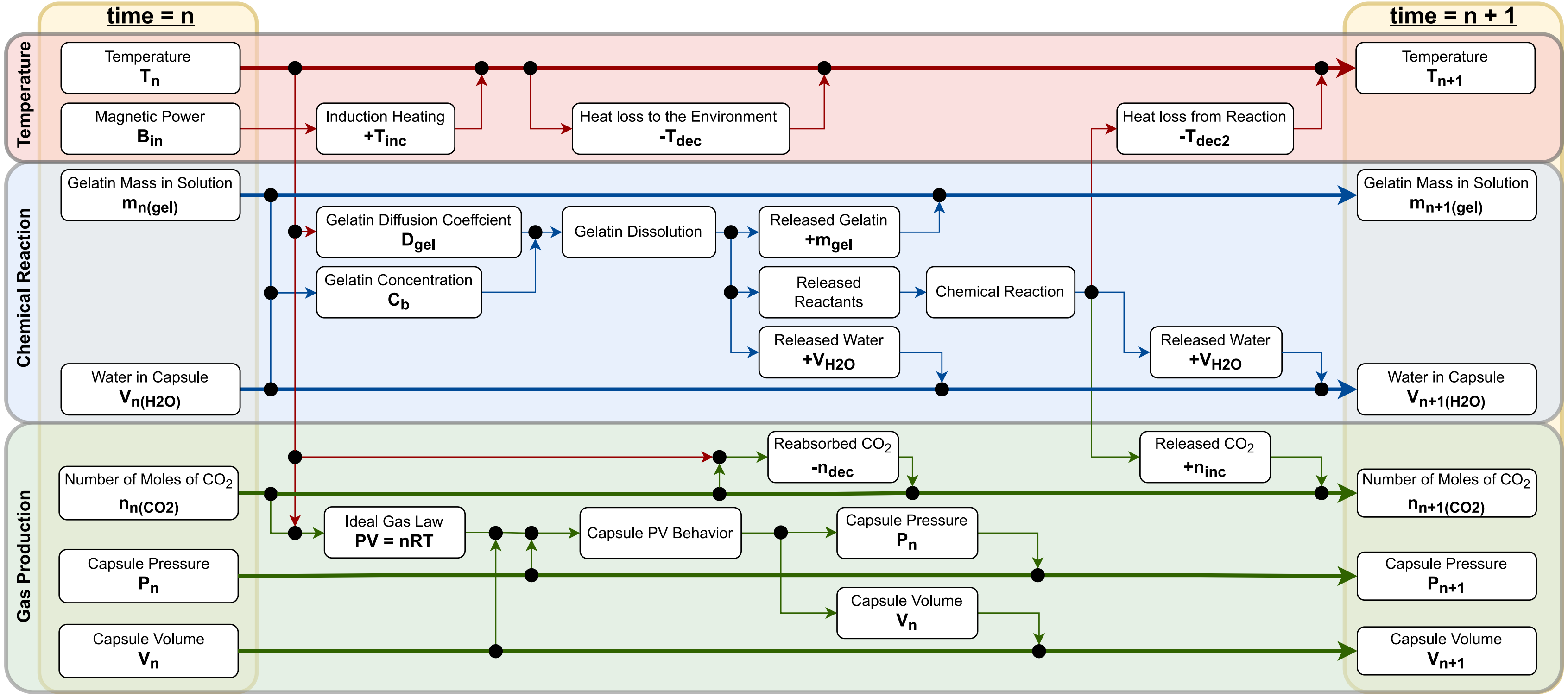

Fig. 3.2 Flow diagram of the simulation of inflation mechanism, showing the interaction between different variables of the theoretical model. The interaction is broken down into three aspects: temperature, chemical reaction and produced CO_2 modeled as an ideal gas inside the capsule. The inputs at time n are used to predict the outputs at time $n+1$.

3.3.2 The Volume Changing Mechanism

This section investigates the magnetic induction driven chemical reaction used to actuate the capsule and identify the underlying control variables. To control the rate and timing of the chemical reaction, each of the reactants is stored separately in solid rings of gelatin to prevent their mixing. When thermal energy is generated in the copper sheet, the gelatin rings slowly dissolve in water inside the capsule, gradually releasing reactants into the aqueous solution. The deflation of the capsule is due to the CO_2 gas being slowly reabsorbed into the water and broken down into carbonic acid (H_2CO_3). The interactions between these variables, separated into three aspects: temperature, chemical reaction and gas production, are explained in Fig. 3.2. In the following model, some parameters were determined, as specified below, from empirical measurements (see Fig. 3.8, Experiment A). The resulting model was then used to validate experimental results of Experiment B in Fig. 3.8.

Temperature

When alternating magnetic fields are applied to the capsule, eddy currents are produced in the copper sheet inside the capsule, which generate thermal energy by Joule heating. The energy generated by the eddy currents per unit mass of conductor, Q_e (J kg^{-1}), is [154]:

$$Q_e = \frac{\pi^2 \sigma {B_p}^2 h^2 f}{6\rho_c} \quad , \tag{3.1}$$

where σ is the conductivity of the copper sheet ($5.95 \times 10^7\, \Omega^{-1}\, \mathrm{m}^{-1}$), B_p is the peak magnetic flux density applied (T), h is the thickness of the copper sheet (m), f is the frequency of the magnetic waves (Hz) and ρ_c is the density of the copper sheet ($8960\, \mathrm{kg\, m^{-3}}$).

This energy can be multiplied by the frequency and the mass of the copper sheet to get the power input to the system, P_{in} (W), at any given time is:

$$P_{in} = \frac{\pi^2 \sigma {B_p}^2 h^2 f^2 m_c}{6\rho_c} \quad , \tag{3.2}$$

where m_c is the mass of the copper sheet (kg).

The power input to the system is multiplied by the duration the magnetic field is applied for. When the temperature of the capsule is T (°C), the temperature increase caused by eddy currents when there is no heat dissipation, ΔT (°C), can be described as:

$$\Delta T = \frac{P_{in} \Delta t}{m_c c_{p(c)}} = \frac{\pi^2 \sigma {B_p}^2 h^2 f^2 \Delta t}{6\rho_c c_{p(c)}} \quad , \tag{3.3}$$

where Δt is time (s) and $c_{p(c)}$ is the specific heat capacity of the conductor (389 J kg^{-1} °C^{-1}).

The system dissipates a portion of excess heat to the environment. While there exists many factors that affect the rate of heat loss, the rate was taken as a constant with reference the experiments. The change of temperature due to heat dissipation to the environment over Δt is:

$$\Delta T = T - T_{env} - (T - T_{env})e^{-2.80\times10^{-4}\Delta t} \quad , \tag{3.4}$$

where T_{env} is the environmental temperature (°C). The decay value was determined by applying induction heating to the capsule, recording the thermal loss, then curve fitting to the measured results (see Fig. 3.8, Experiment A conditions).

Chemical Reaction

Thermal energy input is needed to dissolve gelatin and the reactants it contains from a solid into a liquid. The dissolution rate of gelatin relies on the diffusion coefficient which is a function of its temperature, viscosity of solvent and hydrodynamic radius of the solute, where the latter two variables also depend on temperature. The Stokes-Einstein equation was used with the hydrodynamic radius of gelatin [155] and viscosity of water [156] at different temperatures, to calculate the diffusion coefficient of gelatin for a range of $35 \leqslant T_n < 60$ °C. The results were curve-fitted to get the diffusion coefficient of gelatin, D_{gel} (m^2 s^{-1}), which is defined by:

$$D_{gel} = 3.07 \times 10^{-12} e^{0.0369T} \quad . \tag{3.5}$$

Applying the Noyes-Whitney equation of dissolution, the dissolution rate of gelatin in water [157] was obtained. The mass of gelatin that will dissolve in water, m_{gel} (g), can be described as:

$$\Delta m_{gel} = \frac{A_{gel} D_{gel}}{d_{gel}} \left(C_s - \frac{m_{gel}}{V_{H_2O}} \right) \Delta t, \tag{3.6}$$

where A_{gel} is the surface area of the dissolving gelatin in contact with water (cm^2), D_{gel} is in cm^2 s^{-1}, d_{gel} is the diffusion distance between gelatin and water (cm), C_s is the saturation concentration of gelatin (g ml^{-1}) and V_{H_2O} is the volume of water inside the capsule (ml). d_{gel} and C_s were computationally determined to be 1.5×10^{-4} cm and 0.067 g ml^{-1} respectively, by incrementally changing d_{gel} and C_s, and comparing theoretical results with measured values from Fig. 3.8, Experiment A conditions, until the curves match.

When the gelatin dissolves, the reactants are released into the solvent, the amount of which can be determined using the ratio of ingredients that was used to make the gelatin rings. The gas-producing chemical reaction between $NaHCO_3$ and $C_6H_8O_7$ can be described as:

$$C_6H_8O_7(aq) + 3NaHCO_3(aq) \rightarrow Na_3C_6H_5O_7(aq) + 3H_2O(l) + 3CO_2(g) \quad , \tag{3.7}$$

where $Na_3C_6H_5O_7$ is trisodium citrate. The release of CO_2 increases the pressure inside the capsule which in turn expands the soft membrane, increasing the volume. Using the amount of $NaHCO_3$ that would be released through the gelatin ring dissolution, the number of moles of CO_2 gas inside the capsule, n_{CO_2} (mol), that will be produced as a product of the chemical reaction is derived as:

$$\Delta n_{CO_2} = \frac{m_{NaHCO_3}}{3M_{NaHCO_3}} \quad , \tag{3.8}$$

where m_{NaHCO_3} is the mass of $NaHCO_3$ released from the gelatin ring dissolution (g), M_{NaHCO_3} is the molar mass of $NaHCO_3$ (389 g mol^{-1}).

The chemical reaction also releases water, so the released water can be added back to the water already in the capsule:

$$\Delta V_{H_2O} = \frac{m_{NaHCO_3} 3M_{H_2O}}{3M_{NaHCO_3}} \quad , \tag{3.9}$$

where M_{H_2O} is the molar mass of H_2O (18 g mol^{-1}).

Even though the formation of CO_2, H_2O and trisodium citrate ($Na_3C_6H_5O_7$) is exothermic, the dissociation of $Na_3C_6H_5O_7$ into sodium and citrate ions as well as gas evolution from the formation of CO_2 are endothermic, which results in the overall chemical reaction to be endothermic.

The decrease in temperature due to the energy absorbed per mole of reaction can be given by:

$$\Delta T = Q_r \frac{m_{NaHCO_3}}{M_{NaHCO_3} c_{p(H_2O)} \rho_{H_2O} V_{H_2O}} \quad , \tag{3.10}$$

where Q_r is the resulting energy loss per mole of reaction (J), $c_{p(H_2O)}$ is the specific heat capacity of water (4182 J kg^{-1} °C^{-1}) and ρ_{H_2O} is the density of water (1 g ml^{-1}). Q_r was experimentally measured to be approximately 40 kJ by mixing the reactants and measuring the temperature drop.

Gas Production

As the n_{CO_2} increases, the pressure and volume increases. The change in product of absolute pressure and volume inside the capsule chamber, PV (Pa m^3), can be calculated using the ideal gas law:

$$\Delta PV = \Delta n_{CO_2} R \Delta T \quad , \tag{3.11}$$

where R is the ideal gas constant (8.31 J K^{-1} mol^{-1}).

The following formula describes the relationship between absolute pressure, P (Pa) and volume, V (m^3), that is valid for the current capsule design:

$$P = 102.3\,e^{7.71\times10^{-7}V} - 1.12\,e^{-0.548V} \quad . \tag{3.12}$$

The values were obtained by curve fitting to the data collected by applying a known volume of gas into the capsule for a range of $0 \leqslant V < 30$ ml and measuring the pressure.

In the capsule deflation stage, some of the CO_2 released is absorbed into the solution as H_2CO_3, which can be described as:

$$CO_2(g) + H_2O(l) \rightleftharpoons H_2CO_3(aq) \quad , \tag{3.13}$$

which is a reversible reaction that is dependent on temperature, pressure and concentration gradients. The rate of CO_2 reabsorption can be described as:

$$\Delta n_{CO_2} = n_{CO_2} - n_{CO_2} e^{n_{decay}\Delta t} \quad , \tag{3.14}$$

where n_{decay} is a variable that determines the reabsorption rate of CO_2. The formula for n_{decay} was estimated to be:

$$n_{decay} = -739\,e^{-0.630T} - 8.63\times10^{-4} e^{-2.54\times10^{-2}T} \quad . \tag{3.15}$$

This relation was drawn experimentally by monitoring volume, temperature and pressure of the capsule during deflation which were used to estimate the number of molecules of CO_2 for a range of $25 \leqslant T_n < 40\,°\mathrm{C}$ (data is presented in Experiment A in Section 3).

Time

In Fig. 3.2, the sequence of interactions in the simulation are represented between time T_n $\{n \in 1, 2, \ldots\}$ and T_{n+1}, where the Δt is $T_{n+1} - T_n$. The Δt used was 60 seconds. The output temperature at time $n+1$ can be defined by:

$$T_{n+1} = T_n + T_{inc} - T_{dec} - T_{dec_2} \quad , \tag{3.16}$$

where T_{inc} is the temperature increase due to eddy currents, T_{dec} is the heat loss to the environment and T_{dec_2} is the heat loss due to the chemical reaction.

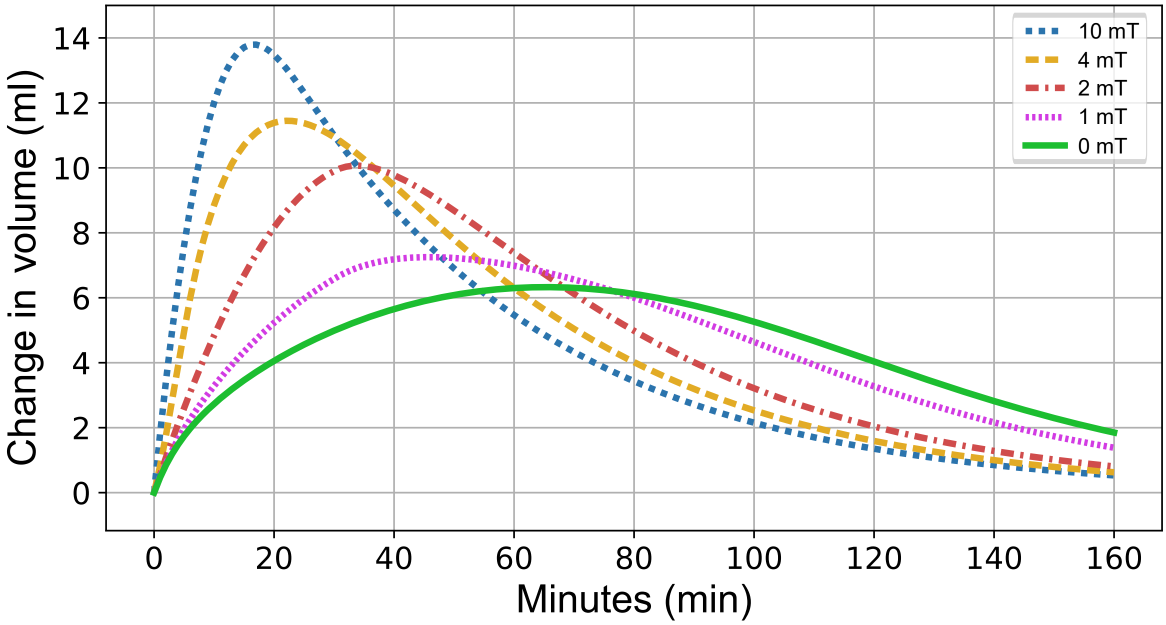

Fig. 3.3 Simulation results of the volume changing capsule reacting to a range of applied magnetic flux densities for 30 minutes of induction heating.

The number of moles of CO_2 inside the capsule at time $n+1$ can be defined by:

$$n_{n+1(CO_2)} = n_{n(CO_2)} + n_{inc} - n_{dec} \quad , \tag{3.17}$$

where n_{inc} is the increase of CO_2 due to reaction, and n_{dec} is the CO_2 decrease due to reabsorption.

The theoretical model can be used to simulate the volume output of the capsule actuation to optimize the design parameters. For example, with increasing temperature, the rate of CO_2 production increases whereas the rate of CO_2 reabsorption decreases. Fig. 3.3 shows how the capsule actuation changes with applied magnetic flux density for a range of 0 to 10 mT which highlights how one variable can change the output considerably. For example, the melting point of gelatin is lower than the body temperature, which results in the capsule still reaching a peak of 6 ml of volume increase without any external heat input, but it reaches this volume in 1 hour. Comparing this result with 10 mT input, the peak volume increases to 14 ml and happens at around 17 minutes, but the time spent at this peak is also reduced as well. Given that thermal input is an external, post-fabrication variable into the system, a single capsule design can be used for a range of clinical needs.

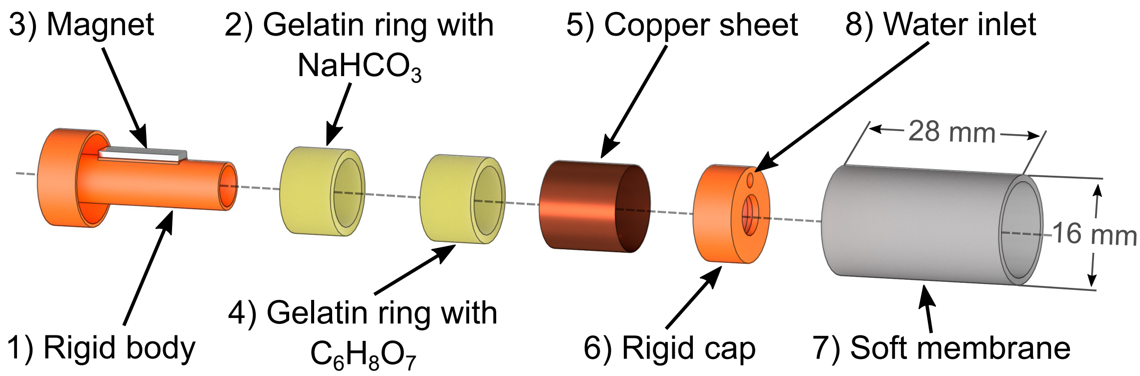

Fig. 3.4 Exploded view of the capsule showing the order of assembly.

3.3.3 Capsule Design

The solid components of the capsule and the assembly order is shown in Fig. 3.4. The inner component of the capsule is the rigid body, which limits the capsule to only expand radially. The hollow section in the center allows passage of food or surgical tools through. A neodymium magnet of $12.7 \times 3.2 \times 1.5$ mm length, width and height respectively, is glued offset towards one side of the capsule on the rigid body for navigation.

For the fabrication of both the gelatin rings, two mixtures of gelatin and water were prepared according to the gelatin ring ratios described in Table 3.1. The ratios were determined through systematic experimentation to yield a correct consistency that retains the reactants. The mixtures are heated in an oven at 60 °C until they are fully melted. Then the reactants are added to their respective mixtures and poured into ring-shaped molds separately. After refrigerating for about 10 minutes, the gelatin rings are inserted around the rigid body. A 0.1 mm thick copper sheet is wrapped around the rings. Then the rigid cap is glued on the other end of the rigid body with cyanoacrylate. Both the rigid body and rigid cap are made of PLA using FDM printing.

The soft membrane that forms the ballooning body outside the capsule is made out of 1 mm thick Ecoflex 00-30 (Smooth On Inc.). It is wrapped around the rest of the capsule and a knot is tied around the circular edges. A thin layer of cyanoacrylate is applied between the soft membrane and the rigid body while the knot prevents the membrane from slipping. The same process is repeated for the other end. Ecoflex 00-30 is a biocompatible silicon [158–160] that is chemically inert with weak acids like citric acid and carbonic acid. For the final step, the capsule is filled with 2 ml of water through the inlet in the rigid cap, then sealed off. The capsule is kept frozen to avoid the gelatin from spoiling and can be defrosted before deployment. The capsule has a diameter of 16 mm, a length of 28 mm, and a weight of 6.65 g.

Table 3.1 Gelatin ring proportions by mass

Gelatin ring with reactant	**Gelatin**	**Water**	**Reactant**
$C_6H_8O_7$ (mg)	170	384	128
$NaHCO_3$ Mass (mg)	102	460	153

3.4 Experimental Setup

An experimental setup that can provide an alternating magnetic field for at least 30 minutes was needed to test the actuation of the capsule. To provide alternating magnetic fields, a custom transmission coil was built for induction heating using braided litz wire, along with a Zero Voltage Switch (ZVS) circuit to supply alternating current. The litz wire was manufactured by winding 100 strands between two desk clamps and manually braiding them. Then the insulation coating are removed from the tips using sandpaper and then soldered. The specifications of the electronics design is shown in Table 3.2.

Table 3.2 Induction coil specifications

Description	**Value**
MOSFETs used for ZVS circuit	STP60NF06
Total capacitance of ZVS resonant tank	$2.2\,\mu$H
Induction coil inductance	$15.4\,\mu$H
Resonant frequency	27 kHz
Target's vertical distance from center of coil	4 cm
Current buildup in the resonant tank	20 A
Peak Magnetic Flux density measured at center	5.5 mT
Induction coil inner diameter	27 mm
Induction coil outer diameter	80 mm
Litz wire individual strand diameter	0.2 mm
Number of strands in litz wire	100
Litz wire diameter total	3 mm
Number of turns in a single layer	12

Instead of using a solenoid coil design where the capsule needs to be through the solenoid for high power transfer efficiency, a flat coil design shown in Fig. 3.5 (a) was chosen, where all coil turns are on the same level, so the magnetic fields can be concentrated on a smaller area. This means that the induction coil could be placed at the closest position to the capsule in a more targeted manner to reduce the risk of non-specific tissue heating. The area of the coil covered by the nth number of turns, A_n (m^2) is:

$$A_n = \pi(r_c + Nd_w)^2 \quad , \tag{3.18}$$

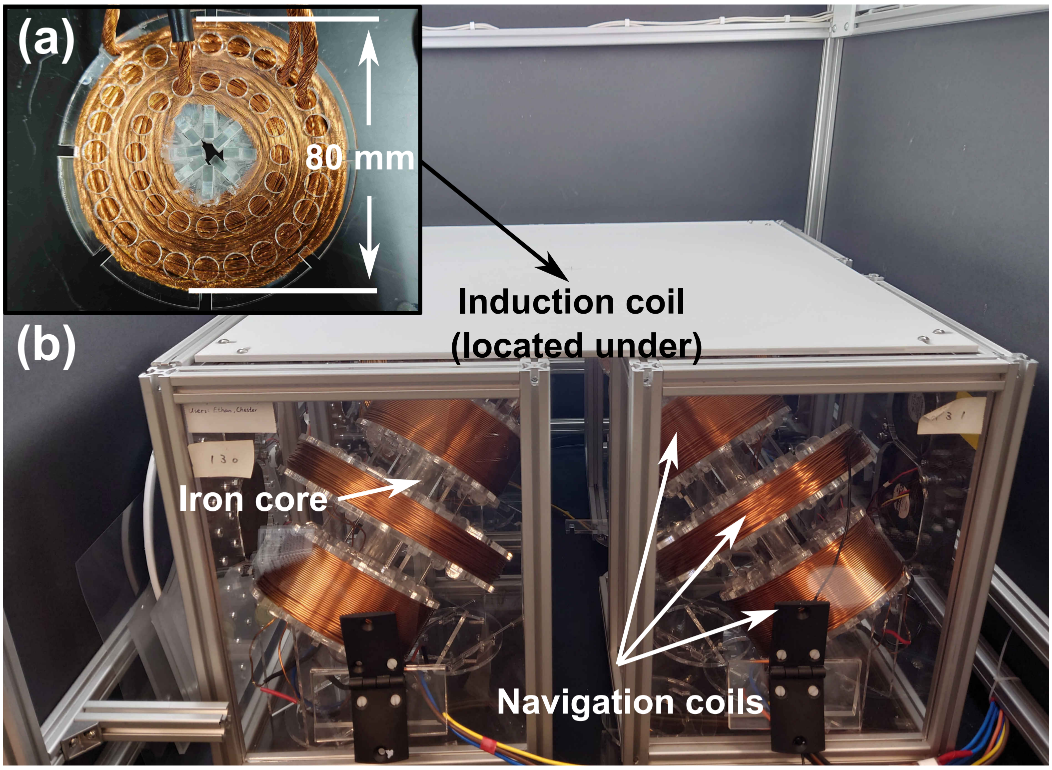

Fig. 3.5 (a) The induction coil for wireless heating. (b) The electromagnetic navigation coil system. The black arrow points at the location under which the induction coil is located.

where r_c is the inner radius of the coil (m), N is the number of turns equal to the n of A_n and d_w is the diameter of the litz wire (m). The inductance of a single layer coil, L (H), can be given by:

$$L = \frac{\mu_0(A_0 + A_1 + ... + A_n)}{d_w} \quad , \tag{3.19}$$

where μ_0 is the magnetic permeability of free space (H m^{-1}).

The temperature and volume variation of the capsule have been measured in experiments in which two variables were changed: the environmental temperature of the capsule and the dosage of reactants. The experimental setup is shown in Fig. 3.6.

Experiment A: The first set of experiments was conducted at room temperature of 24 °C in Tank A, and the ratio of the gelatin rings was as in Table 3.1. Tank A, shown in Fig. 3.6, is a water chamber made of PLA, designed to measure the volume expansion of the capsule. This chamber has a ceiling fixed in place to prevent the capsule from floating after expansion. The ceiling also has holes allowing liquid to rise, so the volume of gas released can be measured via displacement of water. Measurement lines are displayed on a frontal panel of the chamber to track the rise of the water level by a webcam. The coil is placed underneath the tank at a

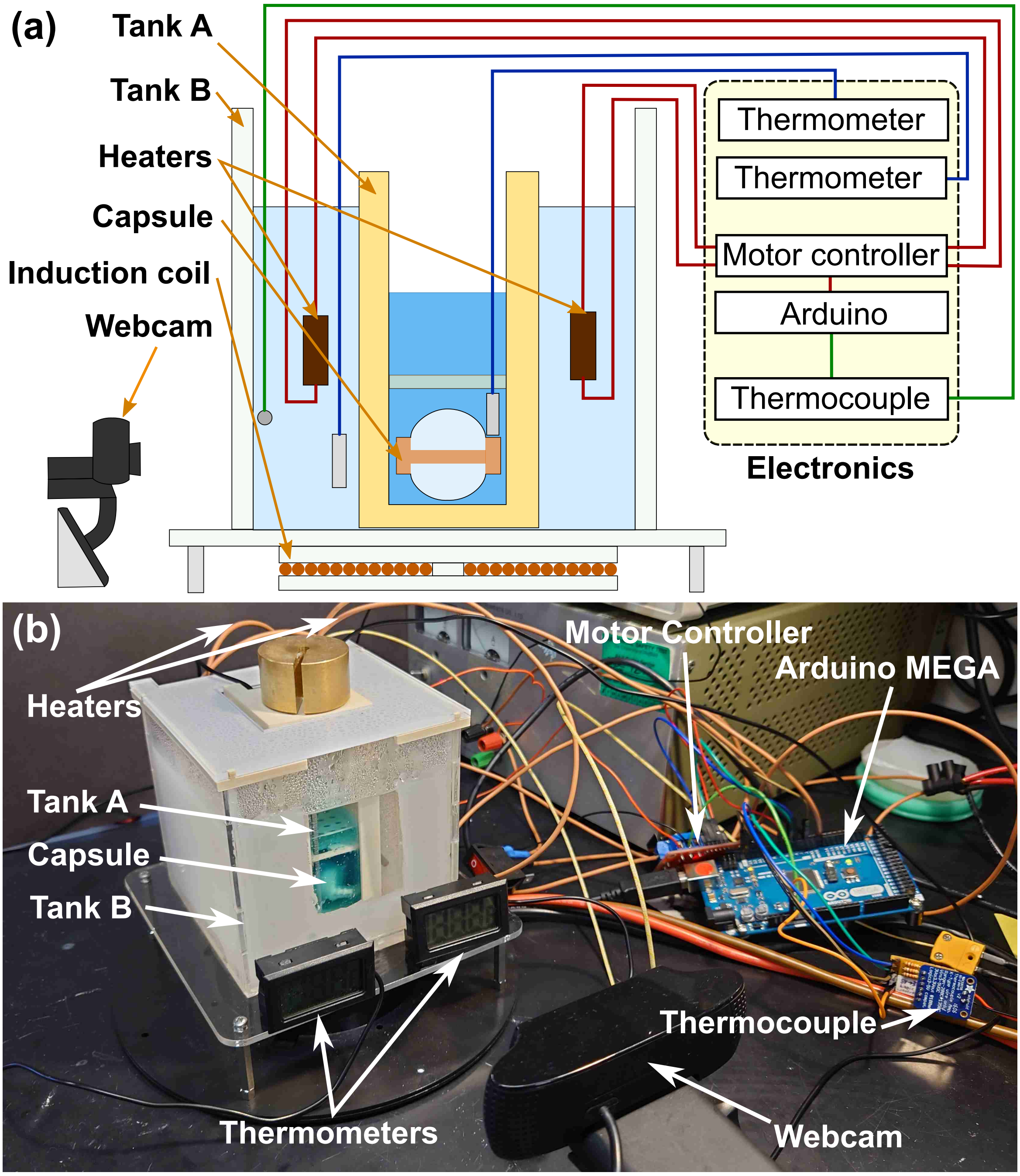

Fig. 3.6 (a) The experimental setup used in the trials, with a block diagram for the electronics. (b) The photo of the experimental setup.

distance of 4 cm. The temperature outside of the capsule, inside tank A was measured using an LCD thermometer. The water was dyed with blue dye for visual clearance.

Experiment B: The second set of experiments was carried out at the body temperature of 37 °C and the reactants of gelatin rings were 183 mg of $C_6H_8O_7$ and 220 mg of $NaHCO_3$. The amount of reactants were increaesed to test the validity of the simulated results, given that the simulation uses values derived from the results of Experiment A. The tank A apparatus was placed inside Tank B as in Fig. 3.6. Tank B is a water bath made from acrylic, insulated with a layer of Ecoflex, and the water inside was heated with two electrically insulated 5 W resistors of 22 Ω, connected to a motor controller. A digital thermocouple was used to measure the temperature of the water bath and an Arduino Mega microcontroller connected to the motor controller was used to regulate the temperature of the water bath at around 37 °C. An LCD thermometer was used to measure the temperature of the capsule inside tank A and an additional one was placed inside the water bath as control. The same setup for Experiment B was used for testing the time it takes for capsule inflation from frozen at body temperature without any extra heat input, instead of defrosting the capsule back to room temperature before the experiment like in Experiment A and B.

Another experiment was carried out to find out how the pressure and maximum diameter of the capsule changes with volume. A syringe filled with air was connected to the capsule and a pressure sensor (005PGAA5, Honeywell). The sensor collected the pressure data while the maximum diameter of the capsule was measured using a caliper. All experiments above consisted of five trials each. The data gathered was used to calculate the mean and standard deviation.

The capsule navigation in a human intestine phantom was tested using an electromagnetic coil system shown in Fig. 3.5 (b). This system is based on previous work carried out in the lab [75, 76] The system consists of 4 diagonal electromagnetic coils with an iron core at the centre of each coil and the induction coil used in the experiments is placed below the workspace. The electromagnetic coils are connected to motor controllers (Sabertooth 2x32, Dimension Engineering), controlling the current and therefore, the direction of magnetic field applied to the magnet inside the capsule. The total peak magnetic field that can be applied at the centre of the workspace is 10 mT when all motor controller outputs are set to the maximum output. In order to navigate the capsule, a rotational magnetic field is applied, shown in Fig. 3.7 (a), which is intended to roll the target. The capsule has an offset magnet, shown in Fig. 3.7 (b), which reacts to the rotational motion by slipping the back of the capsule outwards for the first half of the rotation. Then, the traction force holds the back of the capsule, pushing the front forwards. The rotation of the magnetic field is flipped to complete one full cycle of crawling.

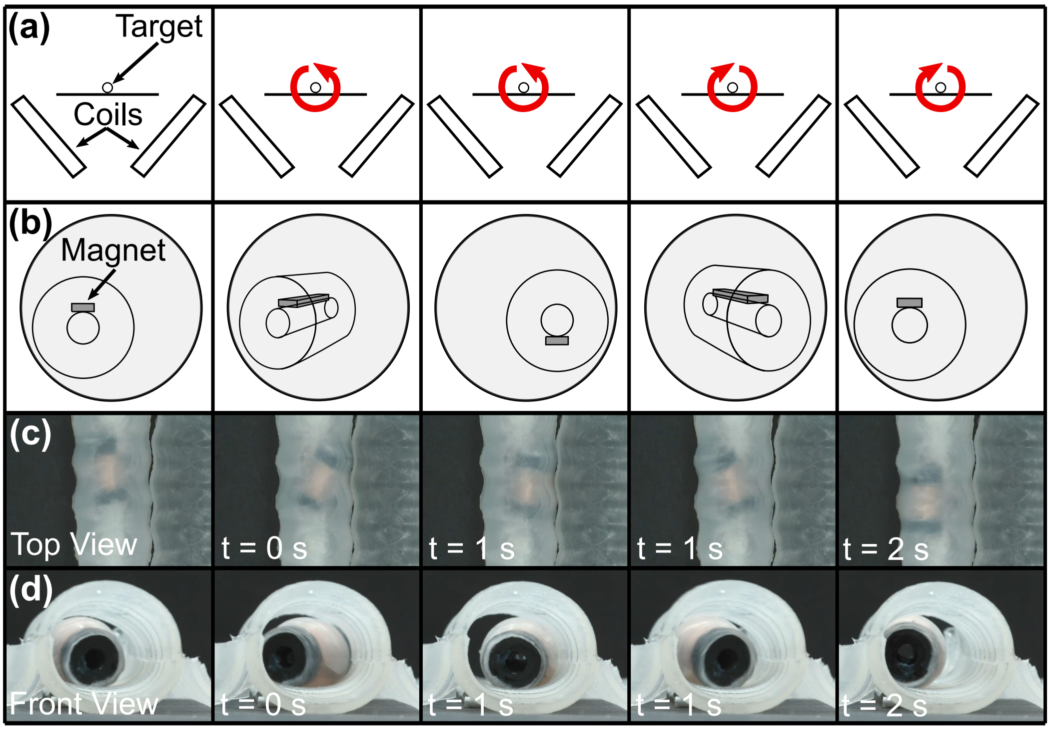

Fig. 3.7 Visual representation and demonstration of the capsule navigation. (a) Shows the navigation coil system applying a rotational motion to the target. (b) Shows the drawing of the capsule and the position of the magnet. (c) Shows the top view of the capsule during navigation and (d) shows the front view.

The intestine phantom was made from Ecoflex-30 with a diameter of 25 mm. The speed of navigation was derived from video tracking, shown in Fig. 3.7 (c-d). To carry out a demonstration of the capsule functionality, the capsule was inserted from one end of the phantom and navigated to the center. Induction heating was applied to the capsule for 30 minutes. After deflation, the capsule was navigated out again.

The navigation was also tested with an Ankon AKC-1 (Operated by Prof. Mark E. McAlindon). The capsule was placed inside a stomach model used for training purposes, filled with water, then the capsule was navigated to the exit using the magnetic guide.

Lastly, a single ex vivo trial was carried out in a sample of pig small intestine. The capsule was placed inside the intestine and tied with a knot at the bottom to prevent the capsule slipping out. The intestine was hung on an arm 4 cm away from the coil. The capsule design was modified to have a hook attached to the bottom to hang weights. When the volume reached maximum inflated size, the knot was removed and weights were incrementally hung until the capsule slipped out to get an estimate of the anchoring force. The capsule was placed back in position and left to continue with the deflation process. Both the phantom and pig intestine trials were carried out at room temperature.

3.5 Results and Discussion

Effects of temperature and reactant dose on capsule inflation

Fig. 3.8 shows the measured results from Experiment A and B while magnetic induction was applied for the first 30 minutes. During both trials, temperature next to the capsule and the change in volume of the capsule was measured.

The theoretical plots of temperature and volume from the simulation, generated with the same corresponding experimental conditions, are also presented in Fig. 3.8 (a) which show similar trends to their measured equivalents. The trials were carried out without a temperature limit and the maximum mean temperature reached during trials from Experiment B was 46.5 °C, which is slightly above hyperthermic limits. As the trials from Experiment A show that the capsule can operate below 45 °C, the capsule functionality would not be affected if a temperature limit was introduced.

The dilation profile of the capsule, measured across trials with both conditions in Fig. 3.8 (b) suggests that the actuation pattern is repeatable, with a maximum standard deviation of 1.67 ml for Experiment A and 2.36 ml for Experiment B. In particular, the maximum volume reached for Experiment A and B were 11 ml and 13.8 ml respectively. Temperature affects both the rate of dissolution and the rate of reabsorption, and the mass of reactants directly affects the amount of CO_2 produced. The theoretical plots of the volume of the capsule follow the measured trends both during inflation and deflation across the varying temperatures through the experiments. The results from this experiment validate the performance of the simulation, with two variables, temperature and mass of reactants, being tested. From the two trials carried out to test the capsule inflation at body temperature from frozen, it resulted that it takes around 5 minutes for the capsule to start inflating, and around 18 minutes for the capsule to reach the diameter of human intestine (30 mm) without extra heat input as opposed to 10 minutes with induction heating. This experiment suggests the time that could be used to navigate the capsule to the site of inflation could be suitable for the first half of the small intestine .e.g., alternative to double balloon endoscopy. Gelatin can be replaced with another material that has a higher melting point than body temperature and is insoluble in water to prevent any actuation before heat input. This comes at the cost of slower response time or higher induction coil power requirements. The same methodology presented in this paper can be used to characterize the inflation behavior with the new material.

Relationship between volume, pressure and diameter

Fig. 3.9 presents the relationship between pressure and volume of the capsule, measured at room temperature. The results were used to derive Eq. 3.12, which is valid when the capsule is inflating without a constraint. The measurements show that the capsule needs around 1 kPa at 5 ml of volumetric increase to overcome the resistance from the soft membrane, then levels off for volumes within the tested range. Fig. 3.10 shows how the maximum diameter of the soft membrane changes with volume of gas inside the capsule. Using the results, the diameter of the actuator when the capsule is inflated, d_a, was curve-fitted for a range of $0 \leqslant V < 30\,\text{ml}$ to derive the formula:

$$d_a = 34.37e^{9.74\times10^{-3}V} - 18.5e^{-0.112V} \quad , \tag{3.20}$$

where V is the volume of gas inside the actuator (ml). The equation can be used to predict the volume of gas necessary to reach the unconstrained diameter of a section of the gastrointestinal tract, which could be useful in the design of future models or in the implementation of a closed-loop control system.

Navigation and capsule demonstration

The capsule navigation was tested in the human intestine phantom, which is shown in Fig. 3.11. The offset magnet rolls the capsule and propels forwards as the center of gravity and the magnetic potential causes one side of the capsule to raise up and down as the capsule rolls. The crawling speed of the capsule in the phantom was determined to be $16.02\,\text{cm}\,\text{min}^{-1}$ from 10 trials. A review of capsule robot crawling speeds [57] shows that this speed is above average if the speeds of swimming robots are excluded. Fig. 3.11 (a-d) shows the capsule demonstration. The capsule is navigated to the center of the phantom where the induction coil is located. Induction heating is applied to inflate and anchor the capsule. The navigation coils were used to confirm that the capsule has inflated above the diameter of the phantom and anchored by trying to propel the capsule using magnetic fields and show that it does not move at this state. After deflation, the capsule stops anchoring and is moved further down the phantom using the navigation coils. The capsule navigation through the stomach model was tested with Ankon AKC-1 which is shown in Fig. 3.12. The capsule is navigated through the stomach model while it is filled with water. Ankon AKC-1 is capable of rotational movements to assists the inspection capabilities of its own inspection capsule. Even though basic navigation functionalities worked well, rotational capabilities were less effective, possibly due to the offset magnet that allows the traction force based intestinal navigation. Functionally, basic navigation is sufficient if the target environment is filled with water and if not, the electromagnetic coil can be used for navigation.

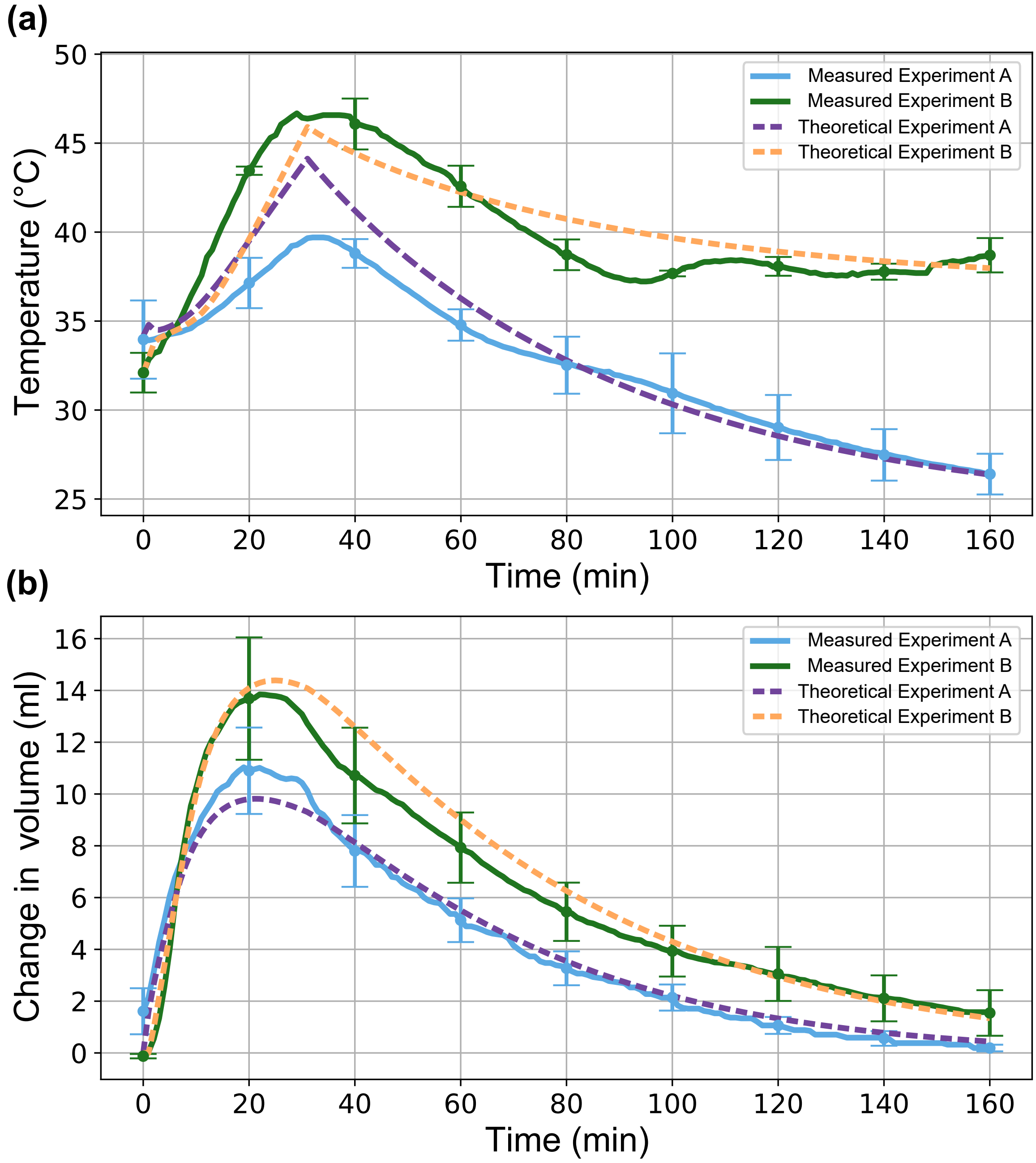

Fig. 3.8 Two sets of measured trials showing (a) the temperature outside the capsule and (b) inflation and deflation of the capsule. The capsule was heated for the first 30 minutes. The plots show the mean measurements for trials with two sets of conditions. The measured results are compared with the theoretical curve of the simulation when it is run with the same conditions.

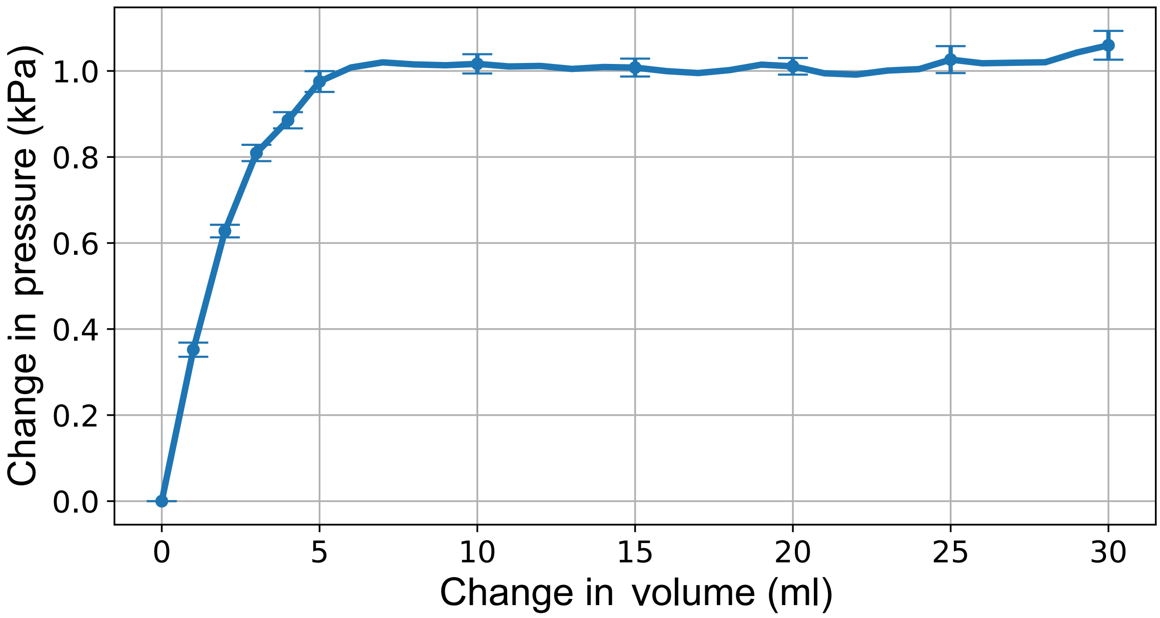

Fig. 3.9 The pressure and volume relationship of the capsule actuation while unconstrained.

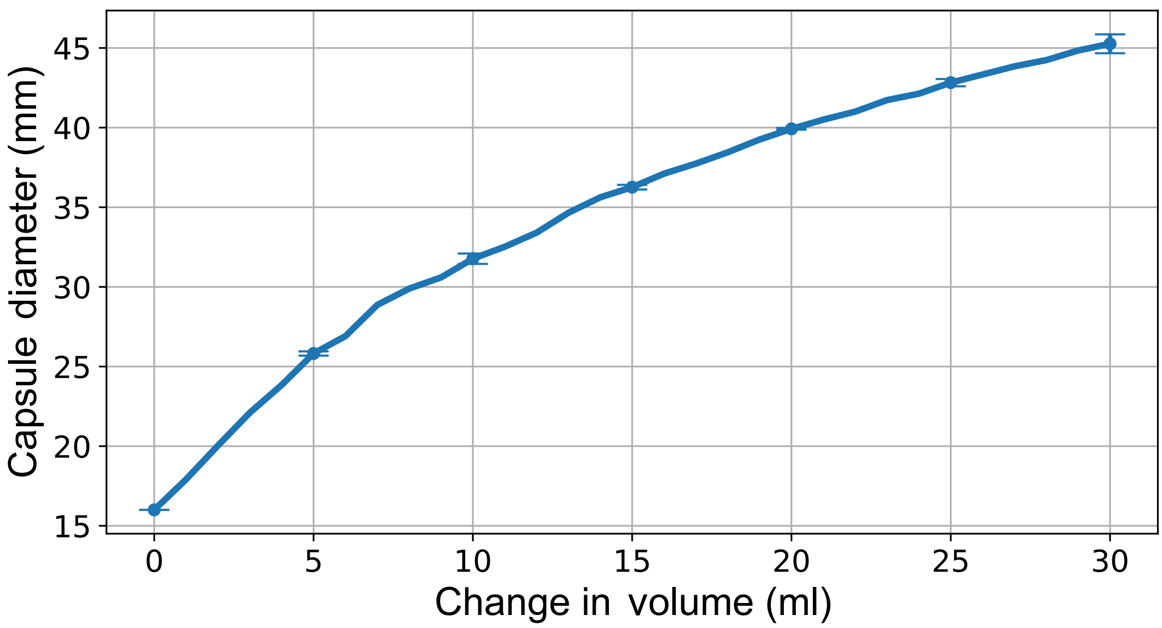

Fig. 3.10 The diameter and volume relationship of the actuator.

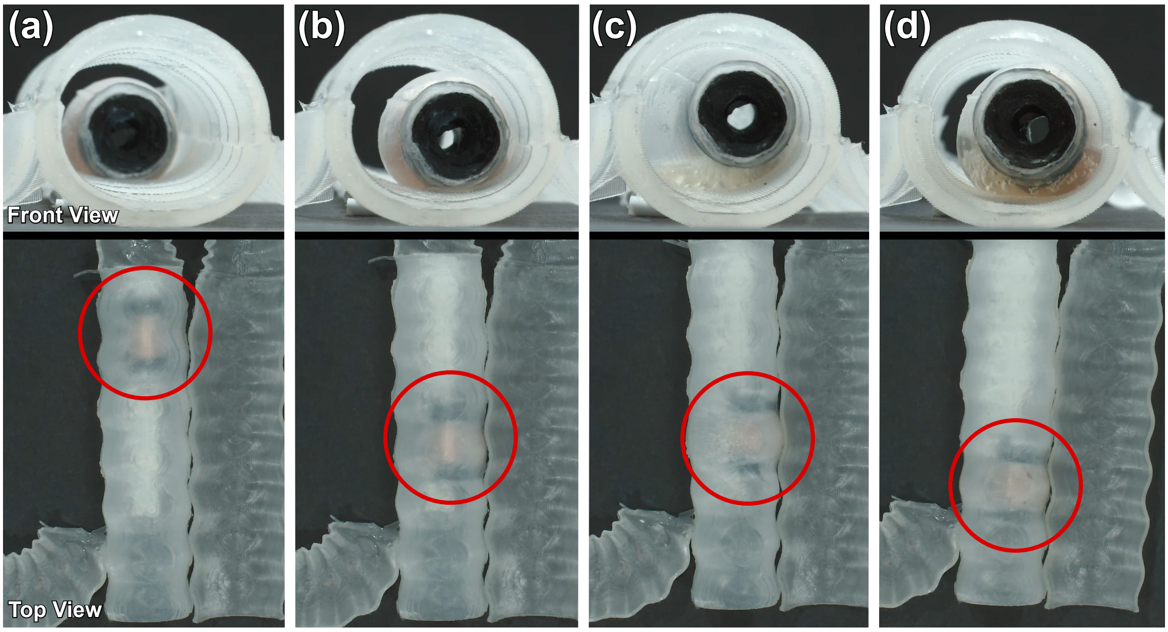

Fig. 3.11 Demonstration of the capsule navigation and anchoring in an intestine phantom from front view (top images) and top view (bottom images). (a-b) shows the navigation of the capsule down the phantom. The red circles indicate the location of the capsule. (c) The capsule is stationary. Induction heating is applied for 30 minutes to inflate and anchor the capsule. (d) After deflation, the capsule is navigated out.

Anchoring on biological tissue

The anchoring capability of the capsule is demonstrated in Fig. 3.13. The capsule is wirelessly inflated in a section of pig small intestine, whose average diameter is 20 mm [161]. This diameter is smaller compared to human small intestine but should provide closer results to using real human intestine as opposed to using the phantom due to the small friction coefficient intestinal fluids provide and elastic properties of the tissues of human and pig intestine being closer to each other than Ecoflex-30 is. The axial diameter of the capsule increased from 18 mm to 24 mm, which is a smaller increase compared to the previous unconstrained experiments. Since the capsule is in a section of pig intestine, the walls of the intestine apply a reactive force to the capsule. Once the intestine diameter is reached, the constraining force of the intestine will end up increasing the pressure inside the capsule as well rather than mostly increasing its volume. While constrained, the added pressure increases the anchoring force which means volume increase beyond the diameter of the intestine can be interpreted as where the capsule starts anchoring. It is unlikely that the capsule will be able to build up pressure levels that could cause a burst due to the large elongation ratio of Ecoflex-30, which can stretch up to 900% before breaking, as well as the

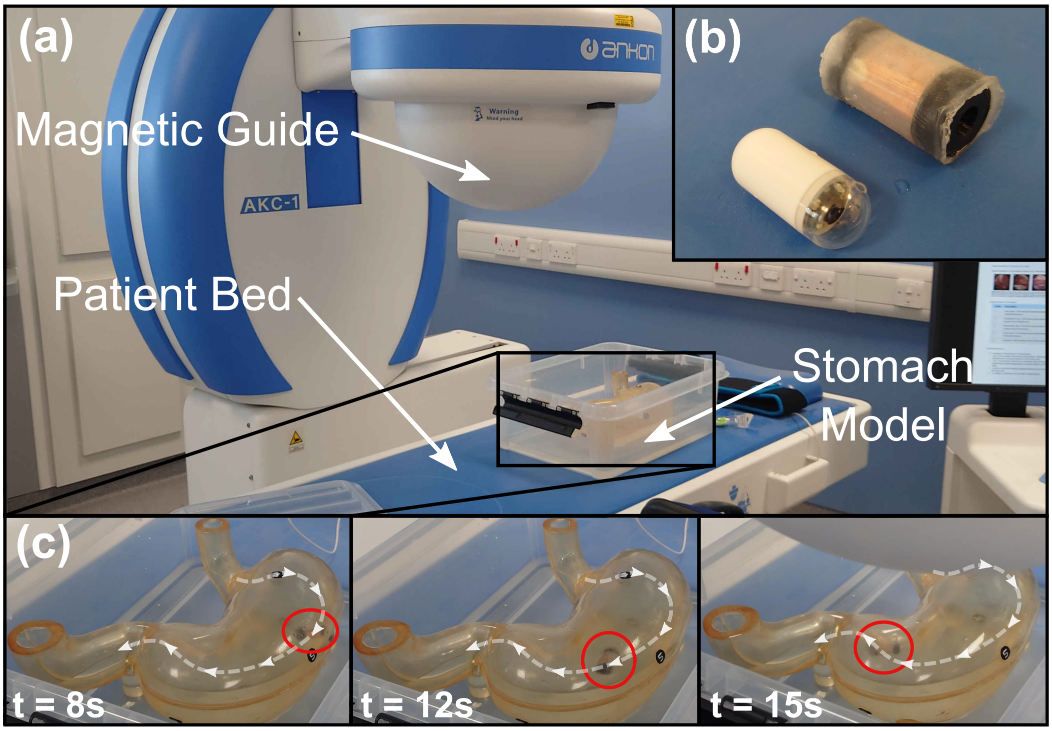

Fig. 3.12 (a) The capsule navigation was tested with an Ankon AKC-1. (b) Ankon's imaging capsule (left) next to the capsule robot presented in this work (right). (c) Close-up of the capsule being navigated through a stomach model used for training (sequence from left to right).

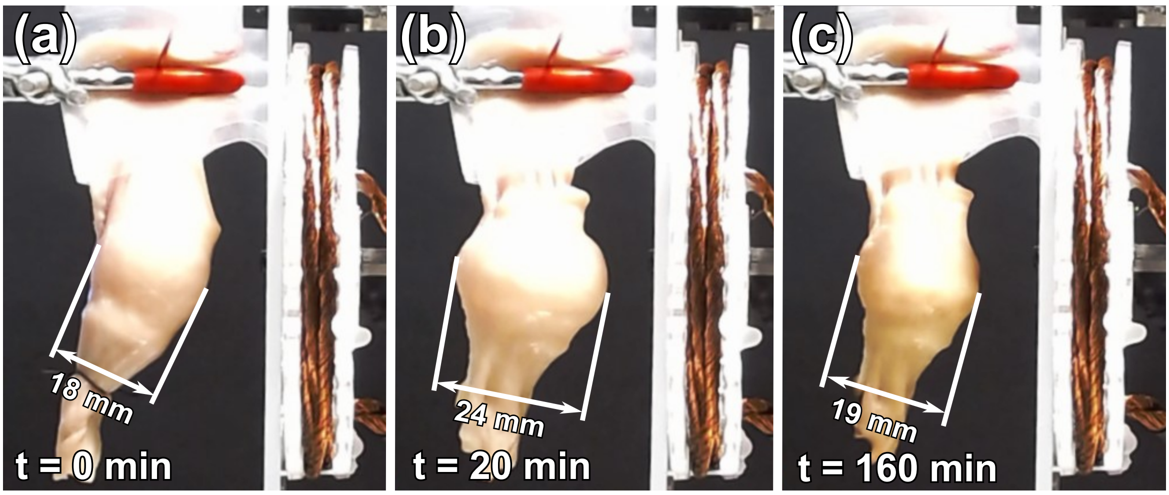

Fig. 3.13 Shows an ex vivo trial carried out using a section of pig intestine. (a) The capsule was placed inside the intestine with a knot at the bottom to prevent slipping. (b) After 20 minutes of wireless heating, the capsule reaches maximum expansion. Weights were hung on the capsule to test anchoring force. Then the capsule was heated for 10 more minutes and (c) left to deflate.

increased pressure also increasing the rate at which CO_2 is absorbed into the liquid. There is also a limited supply of reactants. The results of this trial has shown that the capsule was able to inflate enough for dilating the tissue and the anchoring force was measured to be around 0.27 N. This result is in line with a tethered capsule with a similar design, tested with an ex vivo pig intestine where a smooth balloon was quoted to provide around 0.2 N of anchoring force, which can be increased up to 2.1 N with a textured balloon [30].

3.6 Conclusions

In this paper, an untethered inflatable robotic capsule was presented for tissue dilation. The magnetic induction driven chemical reaction used for the inflation mechanism provides a novel method for controlling inflatable robots. The designed capsule provides volumetric expansion that can be sustained for 44 minutes above 30 mm axial diameter and can operate at temperatures below 45 °C. The study of the mechanism provides different control parameters, which can be used for simulating the actuation behavior and design capsules of varying sizes for different applications. The model developed for the capsule's volume change showed accuracy and can be used to refine the capsule's control. With the parameters chosen for this study, the volumetric expansion of the capsule can be sustained for 44 minutes greater than the axial diameter of an intestine. The chemical actuation of the fabricated capsule as a result of this study achieved an expansion from 16 mm to 35 mm with 0.27 N of anchoring force. Capsule navigation was tested with an electromagnetic coil system and achieved a crawling speed of $2.67\,\mathrm{mm\,s^{-1}}$ in an intestine phantom. The ex vivo trial carried out shows that the force generated by the capsule is sufficient to dilate a section of pig intestine in order aid surgical operations, and anchor the capsule body. The design and control of the capsule can be deemed safe for in vivo applications, given that the method used for inflation carries a low risk of harming the patient, the chemicals the inflation is based on are safe for ingestion in the case of a burst, and the capsule has shown a relatively small error of 15.2% for Experiment A and 17.1% for Experiment B. This error is mostly due to fabrication error of gelatin rings as small changes in the reactant amounts can cause a large change in volume behavior of the capsule.

When designing for different applications, the maximum expanded volume, the rate of volume increase and the time the capsule stays above a certain volume threshold can be adjusted. For example, for stent deployment or mild stricture treatment, the thermal energy input can be increased to decrease the inflation time and increase the pressure output when the capsule is constrained by the stent. The pressure output can be predicted using Eq. 3.12 and Eq. 3.20 if the target diameter is known.

The chemical reaction based inflation provides the advantage of untethered devices which open the potential of minimally traumatic surgical treatments. The inflation can be controlled on site by a priori design of the capsule, e.g., amount of reactants, volume of water, and thermal input via induction heating. A limitation of the current actuation approach is that the current chemical reaction is not reversible, thus the inflation cannot be repeated. If multiple inflation-deflation cycles are needed, then a reversible chemical reaction, or alternative methods should be sought [36, 5]. If the distance of the induction coil from the capsule needs to be increased depending on clinical needs, the current provided to the induction coil can be increased such that the amplitude of the magnetic field received by the capsule stays constant. To improve biocompatibility, the rigid body and rigid cap can be replaced with any biocompatible rigid material and cyanoacrylate can be replaced with a medical grade one. The capsule should be miniaturised by reducing the diameter by 31.3% to fit a standard capsule size “000”. The first few steps in reducing the size could be removing the hollow section of the capsule and increasing the amplitude and/or frequency of the applied magnetic field to account for the reduced copper sheet diameter. Future work will look at adjustment of the design to fit clinical requirements and its evaluation in animal trials.

Acknowledgment

We thank Joanna Jones for her help with the intestine tissue experiment, Marco Pontin for his help with the simulation, Quentin Lahondes for making the human intestine phantom, and the members of Sheffield Biomedical Robotics Lab and Sheffield Microrobotics Lab for their assistance with the project.

Chapter 4

Addressable Parallel Wireless Power Transfer for Capsule Robots

4.1 Abstract

Capsule robots provide untethered access to the gastrointestinal system with minimal invasiveness. There are many examples of therapeutic capsules, but a gap exists in their capability in carrying out complex functions such as manipulation. The major limiting factor is the size requirements for on-board computation and communication, along with capabilities of efficient small scale actuators. This work presents a new amplifier design capable of delivering power to capsule robots and control 6 addressable components with parallel wireless power transfer, which was confirmed by wirelessly lighting up LEDs, independently and concurrently. Additionally, a range of receivers were tested for heating that can be used for thermoresponsive actuators or cell necrosis, and controlling 2 DC motors bidirectionally at the same time for 2-DOF manipulation. Using these mechanisms, a capsule robot design capable of anchoring, manipulation and cauterisation was presented. The wireless powering method presented should benefit developments in electrothermal actuators for further miniaturisation of therapeutic capsule robots.

4.2 Introduction

Medical procedures in the gastrointestinal tract may require a laparoscopy, which is minimally invasive but still requires an incision, or an endoscopy, which is without an incision but may have difficulty reaching some parts of the small intestine. A double balloon endoscopy can be used to access the remaining parts, but will require multiple procedures to do so and require general anaesthetics. Wireless capsule robots can provide access to the entire gastrointestinal system via oral delivery. Some potential benefits wireless capsule robots may provide are reduced invasiveness, increased patient comfort, reduced procedure time and ability to be used under conditions where general anaesthetics is not preferred or considered dangerous due to the possibility of complications [48]. There are many examples of wireless capsules for inspection of the gastrointestinal system [10, 12–15], active drug delivery [10, 16–22], sampling [1, 2, 23–26], anchoring [27–29]. However, there are not many therapeutic capsule robots that are capable of complex tasks as manipulation which is important for surgical functions. There are many examples of therapeutic capsule robots, as shown in Table 2.1, some provide visual feedback, some provide a single therapeutic function, but the ones that try to include both do not fit into the largest allowed capsule size 000.

Miniaturisation of therapeutic capsules could be achieved using many scalable methods of control that can be used for actuation [10]. One example is manipulation of magnets using external magnetic force. Using magnetic force with a permanent magnet equipped robotic arm [15] or an electromagnetic coil system [75–77] can achieve complex motions with a single object. The robot can be localised with hall effect sensors [81] and form a closed-loop navigation system [82]. Additionally, magnetic systems are scalable, giving them high potential of reducing the overall size of the robot [1]. The main drawback is that magnetic force is a global stimulus, which makes the complexity of the design requirement for implementing multiple mechanisms increase exponentially, either due to the interaction between multiple embedded magnets based mechanisms, or due to the fact that the magnetic field will affect both mechanisms at the same time [10]. Some multipurpose functionality can be achieved by using magnetic force for navigation and magnetic gradient for the surgical mechanism [2], but multiple actuation under a global magnetic field remains a challenge.

Another potential approach is using electrical power to carry out surgical tasks using electromechanical, electrothermal or electrochemical actuators [10]. The electricity from battery power may take up too much space and run out of power eventually [10, 35]. Wireless Power Transfer (WPT) solves this issue by powering the robot from outside the body, but comes with the requirement of the power receiver being in good alignment with the transmitter [141] and optimised [140]. Overall size is the general drawback of this approach [40, 39, 38] due to requiring a microcontroller for on-board computation and a Bluetooth or a communications IC and antenna for two-way communication. These components along with a battery or wireless receiver take up enough space for an inspection capsule to be barely around the size of a 000 capsule without any moving mechanical parts or therapeutic function.

There are many examples of actuators that do not require on-board computation such as electromechanical actuators like dielectric [83, 85, 86] and piezoelectric [37, 8, 87, 37, 8] materials, thermoresponsive actuators that use the Coefficient of Thermal Expansion (CTE) [37, 86, 7, 8], Shape Memory Polymers (SMP) [88, 89, 91], Shape Memory Alloys (SMA) [90, 89, 58], hydrogels like PNIPAM [93, 95, 96, 98, 99] and electrochemical actuators that uses on-board pneumatic generation [37, 36, 31, 4], electrolysis [36, 37, 103] and liquid-to-gas transition [104, 6, 105, 5, 6]. One promising approach is using WPT with Resonant Inductive Coupling (RIC) using an Inductor-Capacitor (LC) combination with a specific resonant frequency that is only powered when the correct frequency is being transmitted to actuate the smart material without on-board computation [9, 120, 121].

In the literature, addressability through RIC was shown for up to 3 addressable components. This has been achieved with a transmission system using Frequency Modulation (FM) where the frequency of a pure sine wave is modulated to choose where to send the power. This means that the power being transferred is not concurrent and instead is sequential. For the majority of WPT applications, Class-E amplifiers are used for their high amplifier efficiencies. To achieve high Power Transfer Efficiencies (PTE) the link between the Transmission (Tx) coil and Receiver (Rx) coil needs to be optimised [140], the amplifier itself needs optimisation [147] and need an active way of changing the inductance or capacitance of the resonant tank as the frequency changes [146]. Relying on resonant matching has its own drawback such as sensitivity to capacitive elements of the patient's body [58, 136], and inductive elements like large metal objects around the surgical area or coil deformations all affect the PTE [143]. With FM, given that as the number of addressable components increase, the amount of time that can be dedicated to transfer power to one location decreases, meaning less power can be transferred overall. It also means that the load cannot be something that requires direct powering at the same time. Superposition instead of FM could be an alternative to improve the drawbacks of this approach, but it is difficult to produce mixed frequency signals from an amplifier, especially because amplifiers are most efficient in zero voltage switching (ZVS) conditions where the conduction angles between the threshold and maximum gate-source input are used at their maximum potential [146, 147]. To address some drawbacks of RIC with FM, this paper presents:

1. A new modular amplifier circuit called the Poly-Sinusoidal Resonance Generator (PSRG) that can generate multiple sinusoidal magnetic fields at different frequencies and superpose them at the Tx coil, achieving Parallel Wireless Power Transfer (P-WPT). 6 addressable components has been shown, but further tests may increase this value. Unlike with FM, the 6 addressable components are controlled independently and concurrently using the PSRG system.

2. Tx and Rx side analysis of WPT using the PSRG, a range of Tx coils and a range of Rx circuits for various powering applications such as heating up a Surface-Mount Device

(SMD) Resistor, lighting up an LED, powering a motor with bidirectional control without using a microcontroller or traditional communication methods.

3. A capsule robot design within endoscopic size requirements (11 mm diameter) that shows how an ingestible surgical robot can use the 6 frequencies for a robot to navigate to the site of surgery, anchor to the tissue, and use its manipulator and heater for a cauterisation application in the gastrointestinal system.

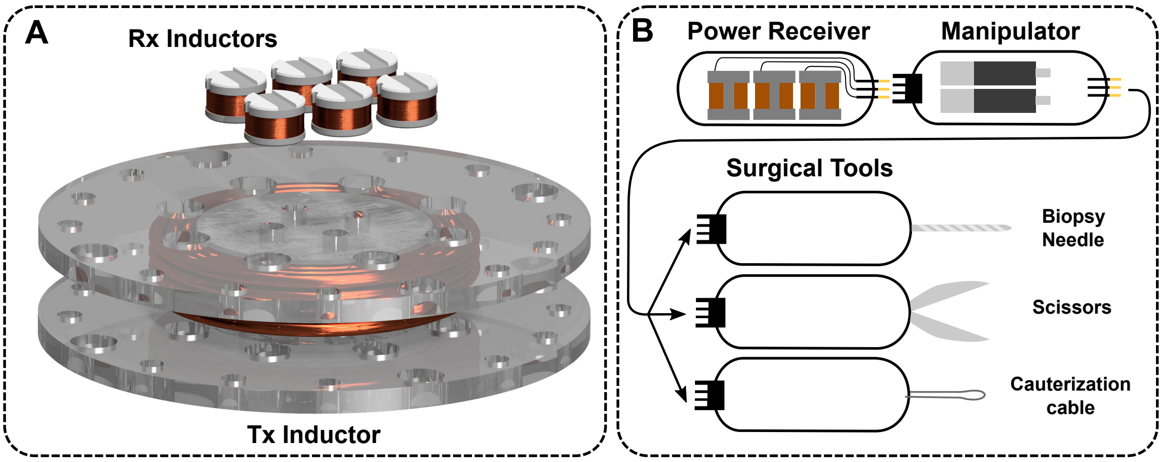

Fig. 4.1 Concept of modular wireless capsules. (A) Shows a CAD render of the Transmission and Receiver coils that the capsule robot could use. (B) Shows the concept of capsule train with a power receiver capsule, a manipulator capsule and interchangeable tools.

4.3 Methods

4.3.1 PSRG Working Principle

An amplifier takes a smaller input signal and amplifies it to a larger signal, which can be voltage and/or current. Amplifiers made up of current controlled transistors amplify and recreate a current signal while voltage controlled transistors amplify and recreate a voltage signal. Both have a threshold input signal before allowing current to pass through and a maximum input signal before the devices break. A sinusoidal wave can be recreated at the maximum power when the peak amplitude of the input signal is equal to the maximum as shown in Fig. 4.2 A (i). When multiple sinusoidal waves superpose, some parts of the waveform add up to peak values that go beyond the maximum, like in Fig. 4.2 A (ii), which will break the MOSFET. If the input voltage is clamped to the maximum, the waveform will be distorted, which will reduce the power delivered across the receivers that are meant to

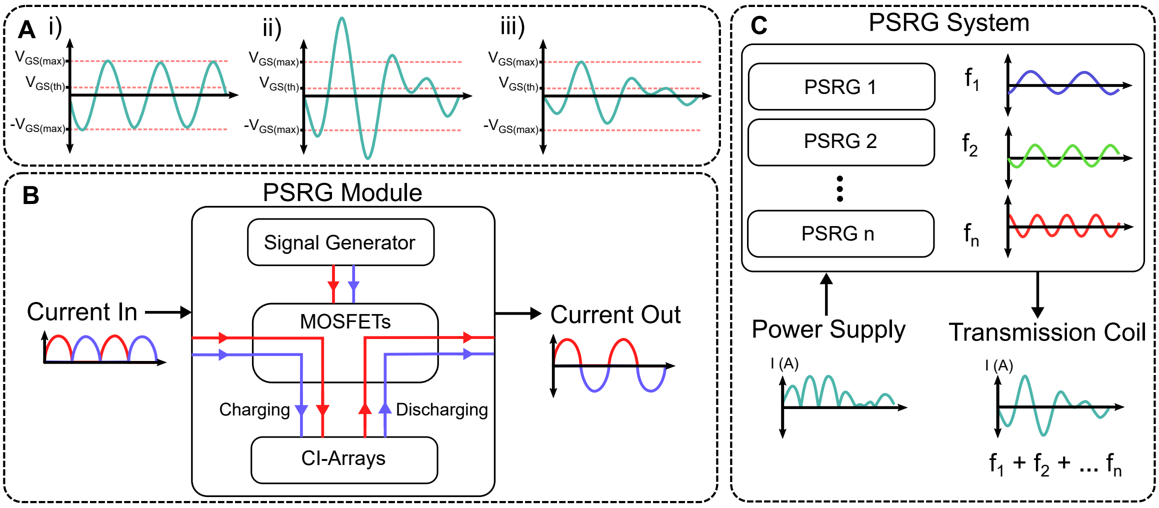

Fig. 4.2 PSRG system block diagram. (A) Limitations of superposition at input signal for traditional amplifiers. (i) A sinusoidal wave can be recreated at the maximum gate-source voltage. (ii) Superposing multiple sinusoidal waves end up with peaks beyond the maximum gate-source voltage. (iii) If the waveform is shrunk to fit the maximum, the power output will be reduced and the waveform below the gate-source threshold voltage will not be recreated. (B) A single PSRG module is used to generate one sinusoidal frequency. (C) Multiple PSRG modules can be connected in parallel. Each PSRG module generates its own frequency. Superposition only happens at the Tx coil current, which avoids high gate-source voltages at the MOSFETs.

receive power and increase power delivered to the ones that are not. If the waveform is shrunk to fit the maximum like in Fig. 4.2 A (iii), the power output overall is reduced. Additionally, a larger portion of the waveform remains below the threshold gate-source voltage which will not be recreated. Instead of trying to optimise the input to output signal performance, another approach was taken with the PSRG system to skip the issues at the input stage entirely by superposing at the output stage. This means that any configuration that allows for a higher voltage supply to be used or improvements to transistor technologies at a material level for higher current output will still benefit the design without suffering from the problems at the input stage.

The modular design starts at a single PSRG module, shown in Fig. 4.2 B, which used to generate one sinusoidal frequency. There are 3 main components that make up a module. The CI-Arrays are capacitor-inductor arrays connected in series that act as an energy reserve where potential energy is built up in the form of reactive power. The signal generator regulates the MOSFETs to switch the CI-Arrays between the power-in line and power-out line. One CI-Array charges while the other discharges and vice versa. The CI-Arrays are connected to the power out in reverse forming both sides of the sine wave. Multiple PSRG modules can be connected in parallel where each PSRG module generates its own frequency as shown in Fig. 4.2 C. The current supplied by each PSRG module only superpose at the Tx coil, which avoids high gate-source voltages at the MOSFETs. The charging and discharging of the CI-Array provides a stable source of current for each frequency and regulates the sinusoidal waveform, which is important because the amplitude of the magnetic flux density depends on current. Using a traditional MOSFET based amplifier with the same MOSFETs with the same physical properties that determine the amount of amplification such as transconductance and channel-length modulation, and the same input voltage used for the PSRG system, the current delivered to the Tx coil will be larger when superposing mixed frequencies.

4.3.2 Transmission Circuit Design

MOSFET Routing Circuit

The main section that brings a PSRG module together is the MOSFET routing. The schematics are shown in Fig. 4.5 A, the PCB trace and the image are shown in Fig. 4.6 A. All schematics and PCBs were designed in KiCad EDA. Each PSRG module has a total of 8 MOSFETs (IRFB4410ZPbF, Infineon), divided into two pairs for controlling each CI-Array. Each pair has two MOSFETs that connects the power to the CI-Array to charge, and the two that connects CI-Arrays to the Tx coil. While one CI-Array is being charged, the other is discharged into the Tx coil. The CI-Arrays are connected in the same polarity to the power supply, but in reverse polarity to the Tx coil, which provides both polarities of the sinusoidal current output to produce the alternating magnetic field.

Signal Generator Circuit

A signal generator is needed to turn on and off the gates of the MOSFET routing circuit with correct timing of the frequency that needs to be sent. A dedicated signal generator design was needed to be developed for two reasons. The PSRG module needs a large potential difference with opposite polarities to be provided to the MOSFET routing circuit, but the signal produced for the two polarities should never overlap in a way that would keep both sides of the MOSFET routing circuit open. The overlap would cause the circuit to be shorted and break the MOSFET due to large peaks of currents.

The schematics of the signal generator are shown in Fig. 4.5 B, the PCB trace and the image are shown in Fig. 4.6 B. The summary of the signal generator steps for one polarity are shown as a block diagram in Fig. 4.3 A. The signal generation starts at a small signal generator (AD9833, Analog Devices) generating a 1 V sinusoidal signal at the selected frequency, shown as a green trace in Fig 4.3 B. The DC offset of the signal is removed with

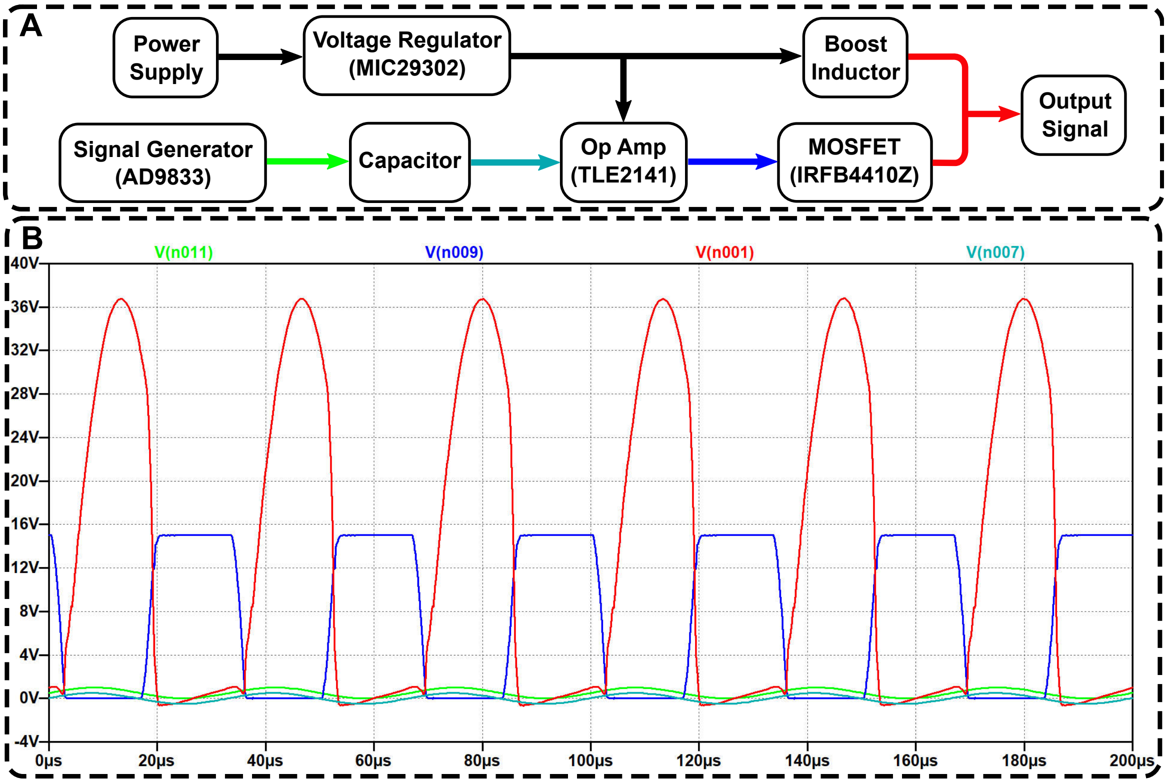

Fig. 4.3 Signal generator steps for one polarity of one PSRG module.(A) Shows a block diagram of the signal generator steps from each component. (B) Shows the traces of the signals from LTspice with colours matching the block diagram.

a capacitor, shown as the cyan trace. A voltage regulator (MIC29302WU, Microchip) is used to supply voltage to the signal generator components, and cut the power off when not in use. Two power OP Amps (TLE2141IP, Texas Instruments) are used to boost the signal up to the voltage of the voltage regulator with opposite polarities and a MOSFET is used to boost the current of the signal. Two MOSFETs for each polarity is used with an XOR configuration that sinks the current if both the polarities are conducting at the same time. An Arduino MEGA is used to control the signal generators (AD9833) as well as the Enable pin on the voltage regulator (MIC29302WU, Microchip), thus controlling which frequency is being sent by the PSRG system. Up to this point, the signal at each polarity is a half-rectified square wave, given that the OP Amp boosts the signal past the peak voltage provided by voltage regulator, which distorts the sinusoidal wave into a square wave. The signal output from the OP Amp for one polarity is shown in Fig. 4.3 B as the blue trace.

Two inductors between the two polarities of the signal, connected to the voltage regulator, boosts the voltage of the signal while also re-constructing the sinusoidal shape of the waveform. The boosted signal output for one polarity is shown in Fig. 4.3 B as the red trace.

Table 4.1 Boost Inductor Inductance for Frequency of Transmission

f (kHz)	10	15	18	20	30	40	50	60	70	80	90	100
L_B (μH)	6300	3000	2100	1700	750	430	280	200	148	114	90	73

The inductance values chosen for the boost inductors need to be adjusted for the frequency of the signal generated from the circuit, which was tested in an LTspice (Analog Devices) simulation where one PSRG module was simulated. The simulation was carried out for a range of frequencies, where a range of self-inductance of the boosting inductors were tested for each frequency. An example of the simulation results at one polarity of the signal generator output is shown in Fig. 4.4 A, its resulting effects on the Tx coil current is shown in Fig. 4.4 B and the current passing through the boost inductor is shown in Fig. 4.4 C. For the optimisation process, a range of inductance is chosen for the boost inductor. For 30 kHz, this was a range of 1500 μH to 100 μH. The simulation was run with 50 μH increments, but this was reduced to 100 for the plots for better visibility.

MOSFETs usually have a gate-source threshold voltage of 20 V. A half-rectified sinusoidal signal has a Root Mean Square (RMS) of 0.5 times the original amplitude. Given that 15 V supply voltage is boosted to half-rectified sinusoidal signal of around 40-45 V, the DC equivalent voltage at the gate is around 20 V, which does not break the MOSFET. The first step is to check that the peak voltage in Fig. 4.4 A is below 40-45 V. Then the peak currents in Fig. 4.4 B and Fig. 4.4 C are inspected. The peak current generated at the Tx coil is 5.63 A when the boost inductor is 550 μH, but the current is very close for the next few increments. For example, at 750 μH the current across the Tx coil is 5.57 A. Inspecting the peak currents for the boost inductor, the minimum currents are -0.27 mA and -0.18 mA and the maximum currents are 0.23 mA and 0.14 mA for 550 μH and 750 μH respectively. For a small trade off of the Tx coil current, the current drawn at the boost inductor is reduced, helping with the stability of the signal generator. The simulation was repeated for each frequency while adjusting the range and increment of the boost inductor's inductance, the results of which are shown in Table 4.1, where f is the frequency being tested and L_B is the self-inductance of the boost inductor.

CI-A Circuit

The CI-Array consists of two sets of capacitor and inductor in series matched to the intended frequency. The schematics are shown in Fig. 4.5 C, the PCB trace and the image are shown in Fig. 4.6 C. The CI-Array could be made with single components for the capacitor and inductor, but were chosen to be in an array for practical reasons. As an array, the current and therefore the heat is distributed amongst the individual components for better heat

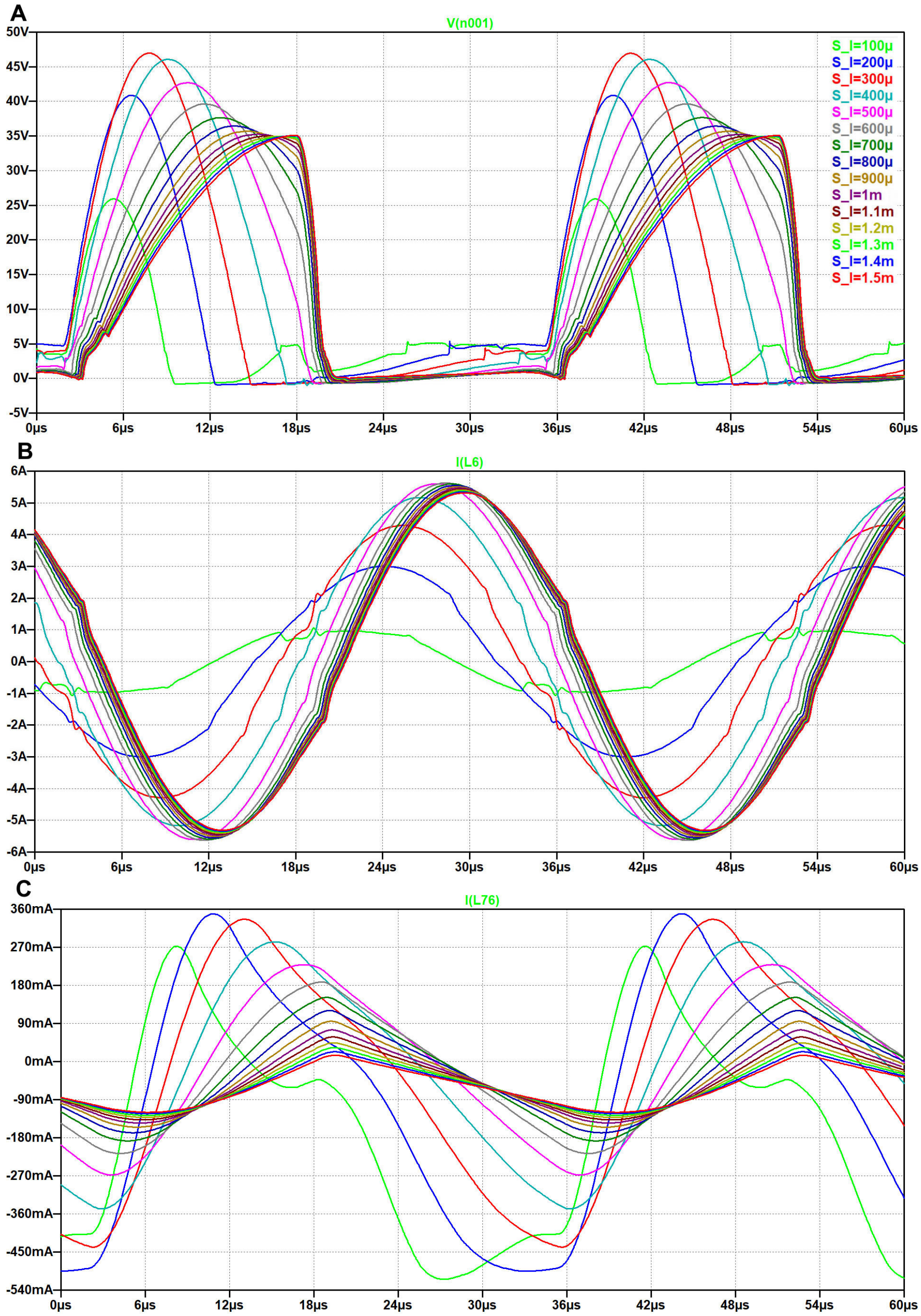

Fig. 4.4 An example of traces from LTspice simulations used for choosing the boost inductor's self-inductance for 30 kHz Tx frequency. (A) shows the voltage output of the signal generator after the boost. The legend in the corner marked "S_l" shows the self-inductance. The first light green for 100 μH is the smallest signal with a peak around 25 V. (B) Shows the resulting current across the Tx inductor. (C) Shows the current draw in the boost inductor.

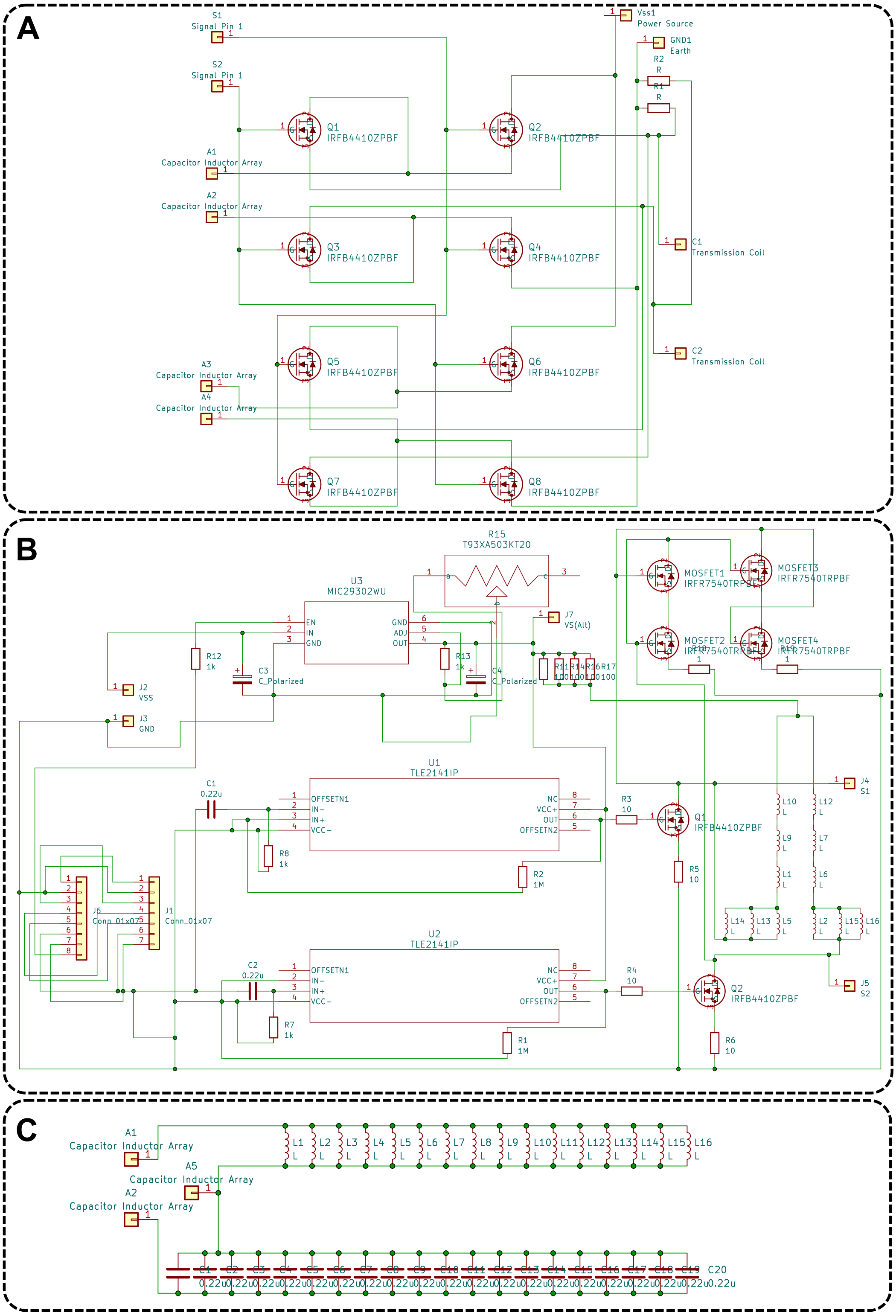

Fig. 4.5 PSRG schematics for a single module. (A) MOSFET routing circuit. (B) Signal Generator. (C) CI-Array. There are two CI-Arrays for each PSRG module.

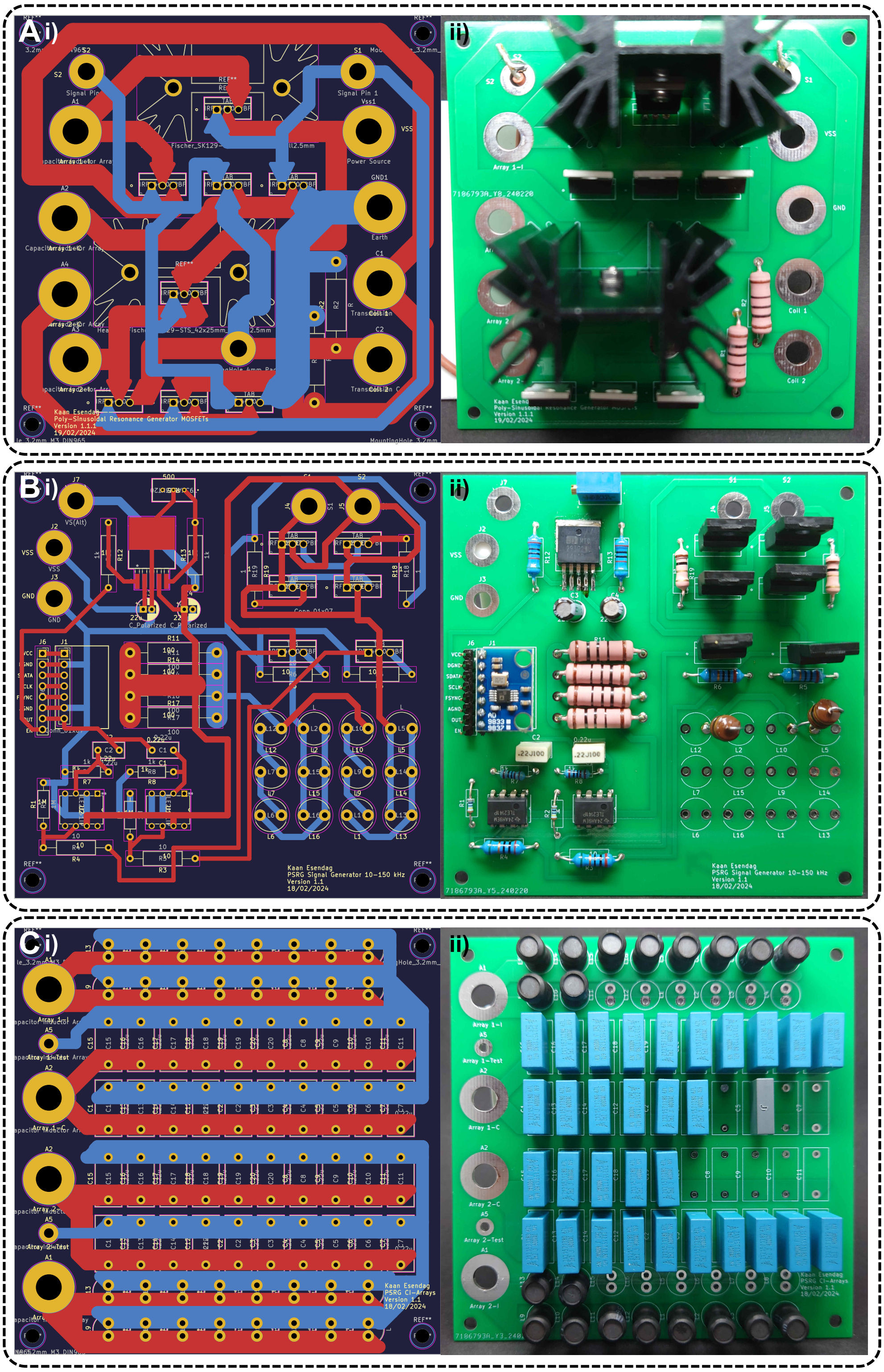

Fig. 4.6 PSRG PCB trace and image of assembled product to make up one module. (A) MOSFET routing circuit. (B) Signal Generator. (C) CI-Array.

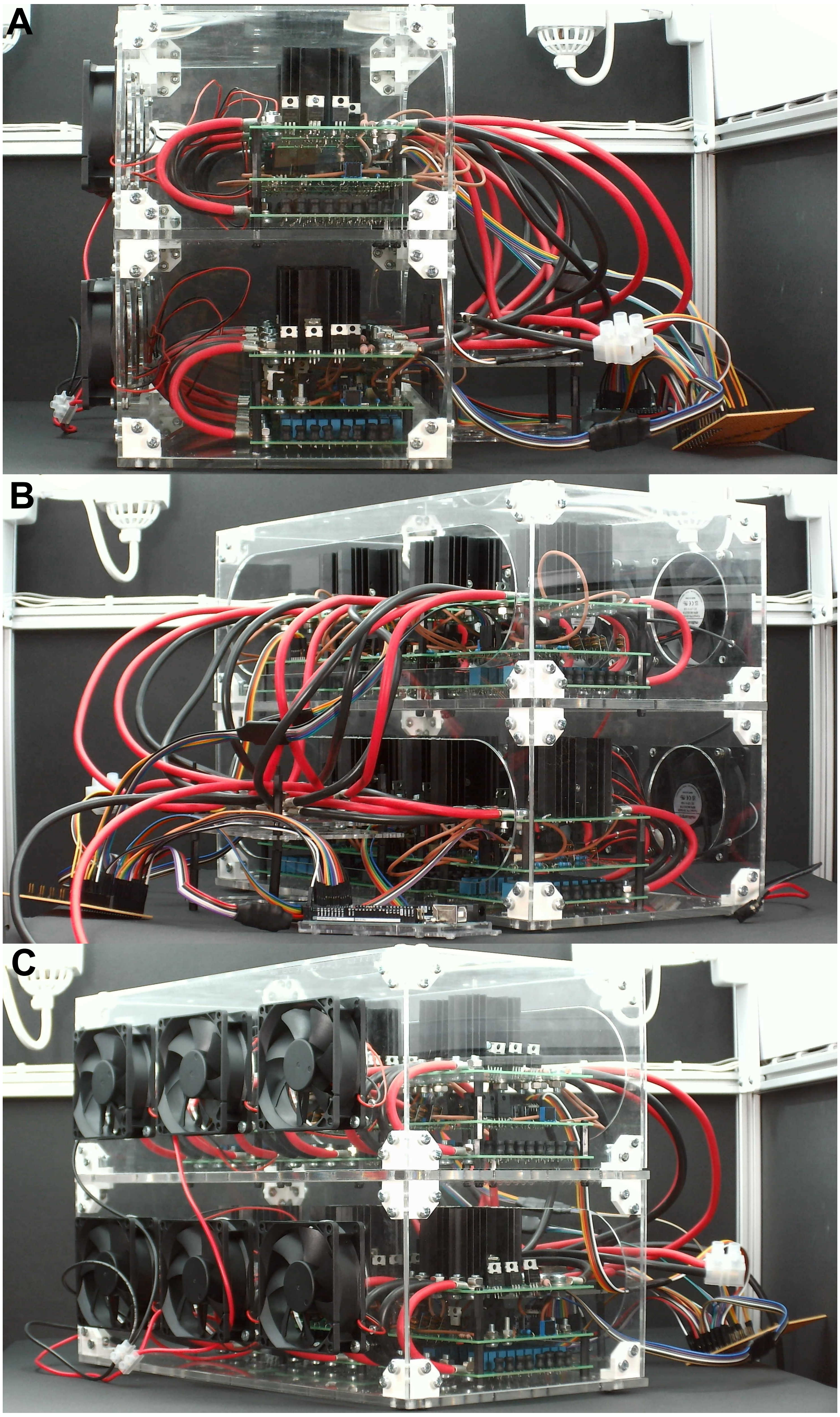

Fig. 4.7 Final assembly of 6 PSRG modules. (A) Side view. (B) Front isometric view. (C) Back isometric view.

management. It is also easier to match the frequency due to component tolerances. The inductors used for this assembly have a DC resistance of 5 Ω, which is divided into 10 as they are connected in parallel. The DC resistance in the CI-Array is a limiting factor of the current that can be built-up by the PSRG system, which means that it should be kept to a minimum. An important extra detail is that the frequency of one side of the array needs to match the other for best WPT. To keep consistent thermals throughout the experiments, each PSRG module had its own cooling fan which can be seen in the fully assembled images of the PSRG system in Fig. 4.7.

4.3.3 Receiver Circuit Design

For microcontroller-less operation, passive components including inductor, capacitors, resistors and diodes can be used to control a variety of different loads using the PSRG system. The receiver design choice will depend on whether the load needs AC, DC, direction control and whether the load is voltage driven or current driven. For heat generation, a resistor can be used as an AC load in series with the LC like the circuit in Fig. 4.8 A, given that no power is lost to the diodes converting the AC power to DC. To wirelessly turn on an LED, an LED in parallel to the LC circuit with a resistor can be chosen, shown in Fig. 4.8 B, as the LED will limit the current if it is connected in series to the LC. This circuit can also be used for any other load that requires DC power, but has a high internal resistance that would limit the power that could be built up by the LC tank. For such loads, a larger voltage is needed than current, so a resistor is needed to improve selectivity between different resonant frequencies of receivers. A DC motor can be driven by a series LC circuit, shown in Fig. 4.8 C, with one diode in series with the motor and another diode in parallel with both the motor and its diode to allow the reverse direction current to bypass the motor. If both directions of current across the load is needed, the bidirectional control circuit in Fig. 4.8 D can be used. Each bidirectional circuit has two series LC circuits matched to different frequencies where each frequency is used for one direction of current. The diodes are connected similarly to the single direction circuit, but one of the LC is connected in opposite direction to the load. This circuit needs the smoothing capacitor to prevent the opposite diodes from bypassing the motor. The circuit also benefits with separating the frequencies matched on the same circuit further. The load on this circuit will be voltage limited to double of the breakdown voltage of diodes used because higher voltages will pass through the diodes back into the receiver inductor instead of the load. Also, the conduction time of the diode needs to be faster than the frequency of the transmission. The circuits from Fig. 4.8 A-C are basic LCR circuits and the circuit in Fig. 4.8 D was designed for this specific project. All the circuits were fabricated

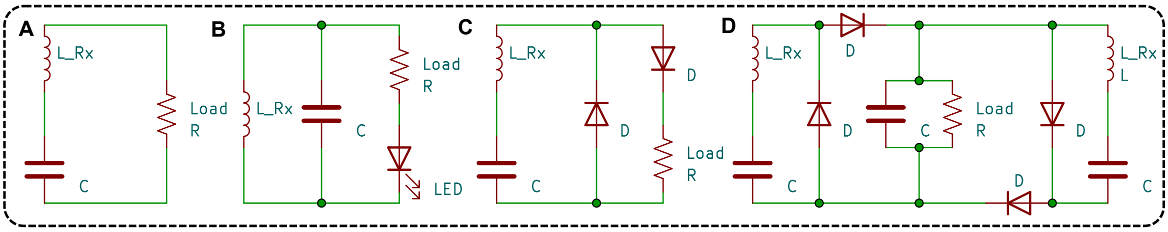

Fig. 4.8 Receiver circuits. (A) Series LCR with AC load. (B) Parallel LCR with DC Diode/LED Load. (C) Series LCR with DC Load. (D) Bidirectional control circuit with 2 Rx coils and 1 DC Load.

by directly soldering components magnet together with magnet wire instead of using a PCB to save space inside the capsules.

4.3.4 Tx/Rx Design

One of the advantages of the PSRG system is that it is suitable to be used with a single Tx coil for a range of frequencies. This means that there is no need to account for the mutual inductance between Tx coils for systems that utilize multiple Tx coils [150]. Multiple Tx coils would not be a simple offset solution, given that the magnetic field produced from each Tx coil mutually inducts with all the other Tx coils. The higher the current is, the higher the mutual inductance, making the problem a non-linear one. If the frequencies need to be independently controlled, there needs to be an offset for each combination of frequencies to account for. This makes the problem increase exponentially with number of addressable components. Having a single Tx coil solution gets rid of this problem entirely, but comes with the limitation of selecting a suitable frequency range.

For the purpose of these experiments a frequency range of 30 kHz to 90 kHz was chosen with 12 kHz increments. The range was started from the lowest frequency with the lowest energy transfer potential possible for powering the capsule and then finding the smallest gap that worked. These conditions should help to set the baseline as more frequencies and number of addressable components are added. It was determined that 18 kHz did not deliver enough power to turn on a motor compared to higher frequencies, so the starting frequency was chosen to be 30 kHz. When 6 kHz increments were tested with an LED application, the selectivity did not exhibit good results where minor positioning differences of Rx coils would affect results. 12 kHz increments were chosen instead of 10 kHz to avoid the effects of harmonic interference delivering power to the first harmonics of the fundamental frequency. From initial tests in simulation, using 30 kHz and 66 kHz has reduced this effect and second harmonics such as 30 kHz and 90 kHz does not exhibit as much interference in power delivery as first harmonics.

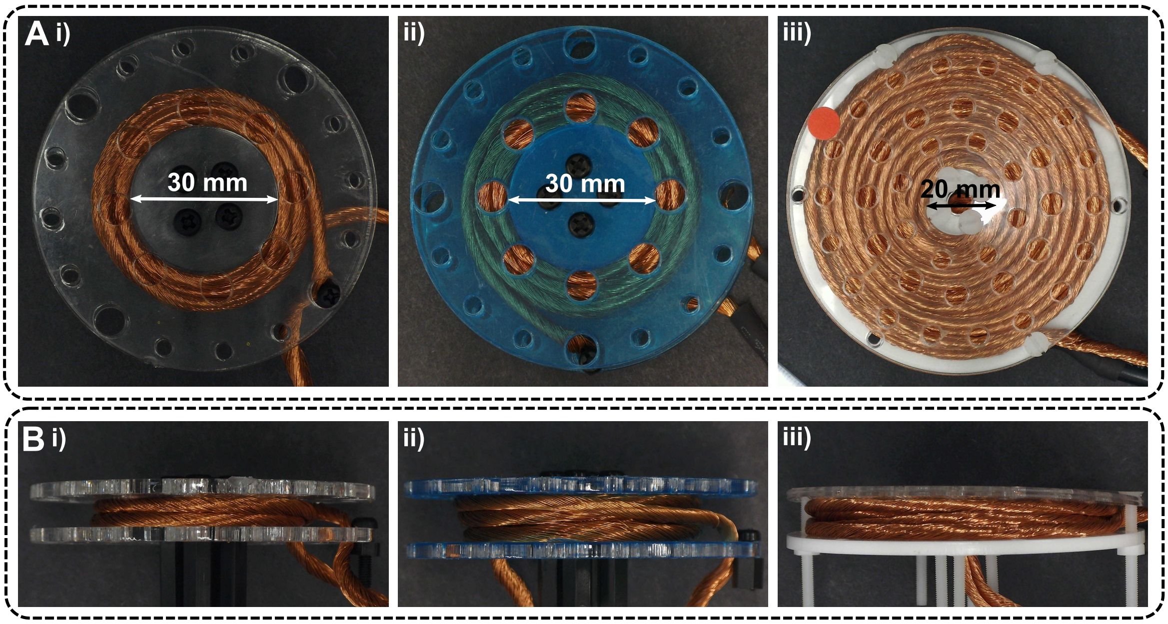

Fig. 4.9 Transmission coils used in the experiments. (A) Top View. (B) Side view. (i) L_1. (ii) L_2. (iii) L_3.

A range of Tx inductors were fabricated to test the performance of the PSRG system and find an optimum Tx inductor for the chosen range of frequency. Inductors L_1, L_2 and L_3 have an inductance of 2.85, 5.44 and 18.56 μH respectively, the images of which can be seen in Fig. 4.9 and further parameters are given in Table 4.2. They were all wound using a Litz wire made with the same parameters.

For the Rx Coil, L_{Rx}, an off the shelf 8 mm diameter, 5 mm height unshielded inductor with a ferrite core that has a self-inductance of 3700 μH was used (SDR0805, Bourns). To match the Rx coil with the target frequencies, f_t, a range of capacitors were chosen shown in

Table 4.2 Inductor Characteristics

Inductor	L_1	L_2	L_3	L_{Rx}
Inductance (μH)	2.85	5.44	18.56	3700
Number of Horizontal Turns	3	3	11	26
Number of Vertical Turns	2	3	2	16
Individual Wire Strand Thickness (mm)	0.2	0.2	0.2	0.1
Number of Strands	100	100	100	1
Total Diameter of Coil Wire (mm)	2	2	2	0.1
Inner Diameter of Coil (mm)	30	30	20	3.5
Outer Diameter of Coil (mm)	50	50	100	7
DC Resistance (Ω)	<0.1	<0.1	<0.1	15

Table 4.3. The resonant frequency, f_0 can be calculated by using the formula:

$$f_0 = \frac{1}{2\pi\sqrt{L_x C_x}} , \tag{4.1}$$

where C_x is the capacitance and L_x is the inductance.

The inductance of L_{Rx} and the capacitance of the capacitors were measured using an LCR meter (BM4070, PROSTER), but the Tx coils were too small to measure. Instead, they were measured using a signal generator (SFG-1013, GW Instek), an oscilloscope (GDS-840C, GW Instek), a known capacitor and a resistor. A series LCR is built with the inductor to be tested, and a frequency sweep was applied. The lowest voltage measured across the LC is the resonant frequency of the circuit, as the reactance of the LC will be the lowest. Using the known f_0, C_x and Eq. 4.1, the inductance was calculated. L_{Rx} has a DC resistance of 15 Ω but the resistance of L_1, L_2 and L_3 are too small to measure with an LCR meter and assumed to be lower than the lead resistance of 0.1 Ω.

Table 4.3 Resonant Frequency for Receiver Circuits

Frequency	$f_t(kHz)$	$C_x(nF)$	$f_0(kHz)$
f_1	30	7.6	30.01
f_2	42	3.88	42.01
f_3	54	2.34	54.09
f_4	66	1.57	66.12
f_5	78	1.12	78.11
f_6	90	0.842	90.17

4.3.5 Capsule Design

The capsule, shown in Fig. 4.10, has been designed within endoscopic dimension limits of 11 mm diameter to allow for oral delivery. The capsule could be delivered past the oesophagus in an endoscopic procedure and released after entering the duodenum. The capsule robot consists of 4 individual 000 capsule sized sections, within 28 mm length and 11 mm diameter. A soft membrane connects the 4 capsules to allow navigation in the crevices of the small intestine. A 3x3 mm neodymium magnet has been included at the tip of the robot to allow the navigation towards a target location with the help of a magnetic or electromagnetic system.

The first two capsules contain 6 Rx coils to allow WPT. After the Rx coils are electrically insulated, capsule 1 can be filled with an aqueous solution of chemical reactant A and capsule 2 can be filled with chemical reactant B. The two capsules are connected with a soft Ecoflex membrane and the two reactants are separated by 3 gelatin layers acting as the dissolution

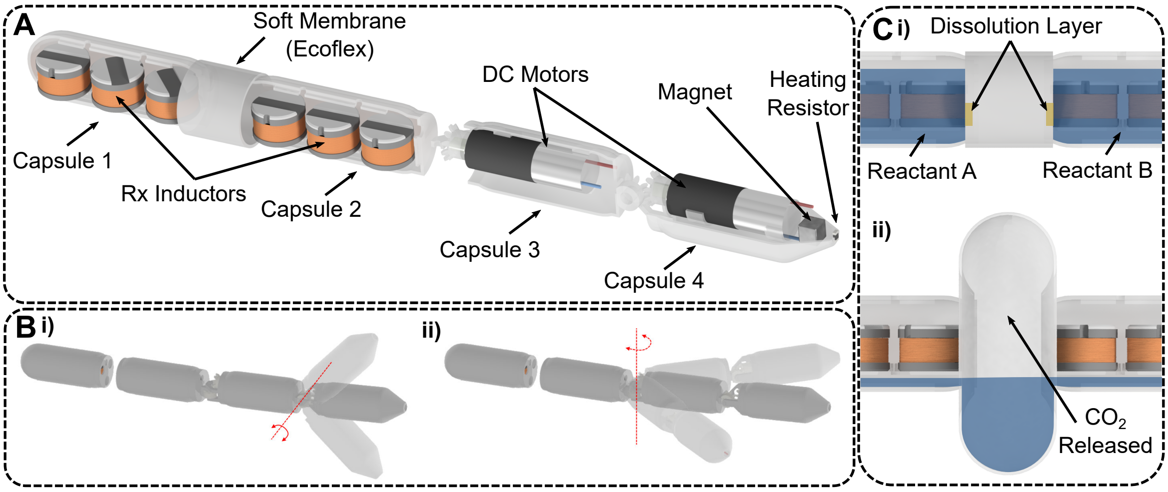

Fig. 4.10 Capsule robot design proposed. (A) The capsule robot consists of 6 inductors for 6 addressable frequencies, an inflating soft membrane for anchoring, 2 motors for 2-DOF manipulation, a heating resistor and a 3x3 neodymium magnet. (B) The mechanical design allows the motors to control 2-DOF joints in (i) vertical and (ii) horizontal rotations.(C) The anchoring mechanism of the capsule. (i) Capsule 1 and 2 are filled with reactants and the dissolution layer is melted with an internal heating resistor. (ii) The chemical reaction releases CO_2 to inflate the soft membrane for anchoring.

medium. Upon application of heat to the gelatin layers using an internal SMD heating resistor, the chemical reactants mix to produce a gas as a result of the reaction, which is used to inflate the soft membrane of the capsule and anchor to the walls of the intestine. A more detailed version of this mechanism has been studied in Chapter 3.

The last two capsules both contain a small DC motor and a mechanical design that allows 2-DOF rotation to navigate the capsule tip to a target location. After anchoring, the magnet at the tip of the robot can be used for movement parallel to the walls of the intestine, adding an extra DOF. Some space has been reserved for the bidirectional control circuit for the motors. There is an external SMD heating resistor at the tip of the capsule which can be used to apply heat to a target location to kill pathogens or cells by heating it beyond the limits of cell necrosis (45 °C). It could potentially be used for cauterisation or patching up wounds. With 6 Rx receivers, 1 frequency is used for triggering the chemical reaction for anchoring, 1 is used for heating the target location, and 4 are used for bidirectionally controlling 2 motors.

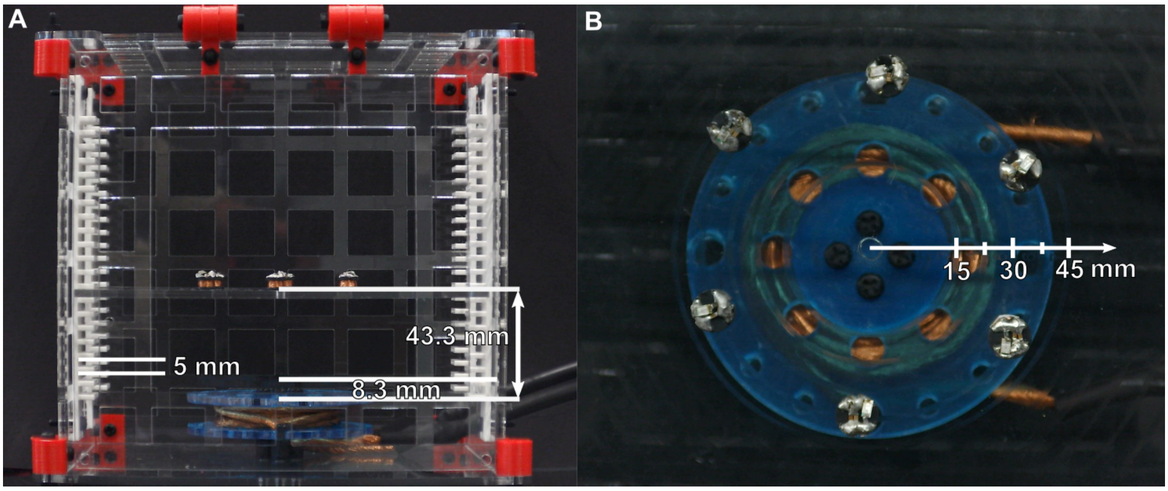

Fig. 4.11 Experimental setup platform. (A) The experimental setup that was used to test Tx/Rx performance at fixed vertical distances away from the Tx coil. (B) The top-down view of the platform showing the radial distance away from the Tx coil.

4.4 Experimental Setup

4.4.1 Testing Platform

The testing platform shown in Fig. 4.11, was fabricated to fix the distances throughout the experiments. On the Tx side, each Tx coil's top acrylic layer starts on the same distance regardless of the number of vertical turns they have. This is to capture a realistic scenario for when the Tx coil needs to be placed as close as possible to the target, rather than fixing the distance to the middle of the Tx coil. The 0 mm position starts from the first layer of the Tx coil winding, the top acrylic sheet of the Tx coil has a thickness of 3 mm, the plastic screws holding the coil together has a head height of 2.3 mm and the acrylic sheet holding the Rx coils also has a thickness of 3 mm, making the shortest distance the Rx coils can be placed away from the Tx coil 8.3 mm. For the Rx coil position, an acrylic sheet is used slid into rows of 5 mm increments. The acrylic sheet the Rx coils are placed on also had markings on it indicating the radial distance away from the Tx coil to be able to evenly spread the coils along a radial distance.

4.4.2 Tx Coil Current Measurement

Since the magnetic flux density produced by an inductor depends on the current, the current has to be measured first. To measure the current across the inductor, 0.1 Ω thick film resistor (PWR220T-35-R100F, Bourns) was connected in series with the inductor to act as a shunt resistor and the voltage drop across the resistor was measured with a PicoScope (2204A, Pico Technology). According to Ohm's Law, to get the peak current passing through the resistor, and therefore the inductor, the peak voltage drop across the resistor is multiplied by 10. The samples were taken at 50 $\mu s/div$ (micro seconds per division) at a sample rate of 12.5 MS/s (Mega samples per second).

A 0.1 Ω resistor was used as it is small enough to ignore the effect of the added series resistance reducing the current, but large enough to cause a voltage drop that is readable by an oscilloscope and distinguishable from noise. Most resistors are physically manufactured using a coiled wire and will have a small amount of self-inductance. Also, oscilloscope probes exhibit a small amount of capacitance between the leads (roughly 140 pF in 1x mode, 40 pF in 10x mode). This makes alternating current measurements difficult due to added noise and unwanted oscillations. A thick film resistor was used to reduce this effect as the resistance comes from thick films of resistive layers rather than coil windings (the model used in this experiment guarantees maximum of 0.1 μH self-inductance). In the PicoScope 7 software used for the measurements, a software 500 kHz Low-Pass filter was applied to remove the remaining noise without affecting the rest of the waveform when measuring the RMS and peak values to only measure the energy of the fundamental frequency.

A Fast Fourier Transform (FFT) analysis of the waveforms in the frequency domain was carried out in the PicoScope software as well. The low pass filter was not used for this section of measurements. The decibel values of the voltage across the shunt resistor for the 6 frequencies were recorded for all 63 Tx states possible with the 3 Tx coils. The fundamental Total Harmonic Distortion (THD) (% and dBu), as well as THD with noise (dBu) were recorded for single frequency waveforms for 8 harmonics. These values should show how deformed the waveform is from a pure sine wave and how much of it is due to noise, which could be caused by the system or the measurement tools used.

4.4.3 Magnetic Flux Density Estimate

To get an estimate of the magnetic flux density produced by each Tx coil, the magnetic flux density produced by each into individual loops of wire within the Tx coil was calculated separately and then added up together. The magnetic flux density, B (T), produced by a single loop of wire can be calculated using Biot-Savart Law:

$$B = \frac{\mu_0 I R^2}{2(x^2 + R^2)^{3/2}} \ , \tag{4.2}$$

where μ_0 is the magnetic permeability of free space ($\mathrm{H\,m^{-1}}$), I is the current passing through the loop of wire (A), R is the radius of the loop of wire (m), x is the vertical distance of the target from the centre of the loop of wire (m).

A python script was written that uses the coil geometry parameters (vertical and horizontal number of turns, the wire cross-sectional diameter, the radius of the first inner loop of wire), the measured peak current passing through the inductor and the vertical distance of the target away from the coil, to calculate the field produced by each loop of wire, which is added up to get the magnetic flux density estimate at target position. Since the majority of the measurements were made with the Rx coil 18.3 mm away from the coil, the magnetic flux density estimate was calculated for this distance.

4.4.4 Tx Error in Superposition

A new parameter was defined to get an estimate of how well the frequencies are being superposed with different Tx coils. When different frequencies of sinusoidal waves mix, they create a unique repeating patterns of peaks and trough. As the rate of change of current increases, the reactance of the inductor increases. Due to the faster rate of change of current resulting from the superposition, the increased reactance of the inductor will limit the current passing through. If you measure the waveforms for single frequencies and manually superpose them, you will get an ideal superposed waveform, which can be compared with the measured waveform superposed at the Tx coil. The single frequency waveforms were sampled from the PSRG output instead of defining a perfect sinusoidal wave because it is a very analogue system where the output has some imperfections due to component tolerances. Using the sampled waveform to construct the ideal superposed waveforms ends up with a more fair comparison which ignores device fabrication errors. The RMS of a wave is often used to convert an alternating or irregular wave into a statistical average value. Calculating the RMS of the ideal, $I_{T_x(Id)}$ (A), and the measured, $I_{T_x(M)}$ (A), waveforms can give us an estimate of the error in superposition, E_{Tx} (%), using the following formula:

$$E_{Tx} = \frac{100(I_{T_x(Id)} - I_{T_x(M)})}{I_{T_x(Id)}} \quad . \tag{4.3}$$

The PSRG system is controlled using an Arduino (Mega, Arduino). A code was written to assume the 6 frequencies as bits, starting with 30 kHz as bit 1 and 90 kHz as bit 6, cycling through all the possible combination of 63 Tx states (equivalent to the decimal value) which are covered through binary counting for a duration of 1 second for each Tx state. The waveforms are recorded using a PicoScope with the same settings as the single frequency Tx current measurements, but instead of just reading the peak values, the entire waveforms are saved instead. These waveforms are extracted manually for each Tx state. An inspection of the mixed waveforms has shown that the longest repeating pattern is 167 us. This value was chosen as the waveform sample length to make sure that the RMS measurement covers at minimum, 1 full repeating pattern. A python script automatically sorts the Tx states, samples the single frequency waveforms to construct the ideal waveforms for each combination of frequencies, then uses Eq. 4.3 to calculate the error in superposition for each Tx state. The data was further processed by breaking down the Tx states into the number of frequencies being mixed and an average is taken. This way, the effects of how the number of frequencies being mixed affect all 3 Tx coils can be interpreted clearly.

4.4.5 LTspice Simulation

An LTspice model was built to test the Tx/Rx circuit in simulation. The simulation uses a single PSRG module for transmission and an LCR circuit with a 1 Ω resistor as the load. The frequency is cycled through from 12 kHz to 202 kHz with 12 kHz increments while the capacitors on both Tx and Rx side are automatically adjusted to match the resonant frequency. Each step is run for 3 ms and characteristic measurements are extracted.

For mutual inductance, the Tx/Rx link can be assumed as a transformer where a coupling factor, k_M, needs to be defined in addition to the self-inductance of both Tx and Rx coils. Apart from the purely electrical properties like self-inductance, the coupling coefficient depends on both the Tx and Rx coil geometries. The space both inductors cover in respect to each other's magnetic flux densities is the main factor of flux linkage. The more lines of flux produced by the Tx coil cuts through the Rx coil, the more potential difference can be generated in the Rx coil according to Faraday's Law.

Instead of theoretically acquiring the k_M values, a small set of experiments were carried out to measure it instead. The Rx coil was matched to 30 kHz with a capacitor and a 1 Ω resistor (PWR220T-35-1R00F, Bourns) is used as the load. The Rx coil was placed in the centre 18.3 mm away from the Tx coil and the voltage across the Rx coil and resistor was measured 3 times for each Tx coil. Then, the same LTspice simulation is used at a fixed frequency, while k_M is cycled through instead. The k_M values with matching simulation results are listed in Table 4.4. These results may have some inaccuracy due to the simulation ignoring the inductors having an iron core. The material properties were not available in the data sheet of the Rx coils which makes it hard to include necessary details in the simulation.

Table 4.4 Coupling Coefficient Table

L_1	L_2	L_3
0.0095	0.012	0.019

The results are curve fitted for a Tx inductance for a range of $2.85 < L_{Tx} < 18.56\,\mu$H to derive the formula:

$$k_M = 6.322981 \times 10^{-3} + 1.193062 \times 10^{-3} L_{Tx} - (2.748023 \times 10^{-5} L_{Tx})^2 \quad . \tag{4.4}$$

Then Eq. 4.4 was used in the simulation that cycles through the frequencies and the simulations were run to collect data for all 3 Tx coils.

4.4.6 Rx Coil Analysis Measurements

To characterize the power transfer of the Tx coils to the Rx coil, a set of experiments were carried out using 2 different resistive loads. Both of the loads used are thick film resistors, one $1\,\Omega$ and the other $20\,\Omega$ (PWR220T-35-20R0F, Bourns). $1\,\Omega$ load was chosen as a representation of the power transfer without a high resistance affecting the results and $20\,\Omega$ load was chosen as a closer comparison to the $22\,\Omega$ resistor that was used for the heating experiments and $30\,\Omega$ of the motor. L_{Rx} was placed in the middle of the testing platform 18.3 mm away from the top of the Tx coil. To make a fair comparison, one Rx receiver was used while switching the C_x for each of the 6 resonant frequencies, given that multiple Rx receivers cannot occupy the exact same space. The circuit used makes up a basic series LCR circuit. On the Tx side, the same Arduino code was used to cycle through the 63 Tx states with 1 second intervals.

A PicoScope was used to record the results for the voltage across L_{Rx} and across the resistive load using 5 us/div at a sample rate of $100\,MS/s$. The peak to peak (pk-pk) and RMS measurements were recorded in logging mode. A python script was written to automatically sort the collected data using the pk-pk L_{Rx} voltage with a threshold to define an ON Rx state (when the Rx is expected to receive power because Tx is sending the f_0 of the Rx circuit) and OFF Rx state (when the Tx is sending frequencies that does not match the f_0 of the Rx circuit). The "ON" and "OFF" here refers to the Tx side, whether the specific frequency in question is being transmitted or not. The terminology was chosen to be able to interpret the analogue nature of power transfer values with an arbitrary digital threshold. There is no digital or active component in the Rx circuit being switched, the state is "ON" when the intended frequency is being sent and "OFF" when not. Then, the script takes an average of the data collected for each Tx state. The measurements for L_3 had an additional half a second pause between each transmission as the script was not able to tell apart ON and OFF Rx States with a threshold for some combination of frequencies, which meant that the Tx state changes had to be defined manually to sort the data.

This experiment was repeated for all 6 Rx f_0, using all 3 Tx coils and 2 resistive loads, 5 trials each, for a total of 180 trials. An average of all 5 trials were taken for each condition. Using the RMS values measured, each Tx state is separated by number of frequencies being sent by the Tx coil and also by Rx state ON or OFF. From this point, the data can be inspected in two ways. First is by taking an average of all Rx circuits with different f_0 for ON and OFF Rx state. This highlights how much the current or power is reduced across all Rx circuits as the number of frequencies being sent increases. The second way is to take each number of frequencies and take an average of each ON and OFF Rx state. Fixing the number of Tx frequencies being sent and inspecting the Rx resonant frequencies highlights how the current or power is distributed across the Rx circuits for ON and OFF Rx states.

The same concept of error in superposition was applied to the Rx side with different definitions for ON and OFF Rx states. Error in superposition for ON Rx state, $E_{R_x(ON)}$ (%), can be defined using the following formula:

$$E_{R_x(ON)} = \frac{100(Rx_{On(n_1)} - Rx_{On(n_x)})}{Rx_{On(n_1)}} \quad , \tag{4.5}$$

where $Rx_{On(n_1)}$ is the average RMS value of ON Rx state when 1 frequency is being sent at a time, $Rx_{On(n_x)}$ is the average RMS value of ON Rx state when x number of frequencies are being sent. The values can either be current or power. The ratio of the difference between a single frequency and multiple frequencies is used get a percentage of how much current or power is reduced as number of frequencies increase.

Error in superposition for ON Rx state, $E_{R_x(OFF)}$ (%), can be defined using the following formula:

$$E_{R_x(OFF)} = \frac{100(Rx_{Off(n_x)})}{Rx_{On(n_6)}} \quad , \tag{4.6}$$

where $Rx_{Off(n_x)}$ is the average RMS value of OFF Rx state when x number of frequencies are being sent and $Rx_{On(n_6)}$ is the average RMS value of ON Rx state when all 6 frequencies are being sent at the same time. The ratio of the OFF Rx state and the lowest point of the ON Rx state is used to get a percentage of how close the OFF state is to what could be considered as the ON state.

4.4.7 Bidirectional Motor Control

To test the bidirectional control circuit, 2 motors were used as DC load and L_2 was used as the Tx coil. The motors (ZWPD006006-136, JMI-Motion) have a 3-stage planetary gear, a length of 18.7 mm, diameter 6 mm and resistance of 30 Ω. The motor is rated 40 mA at 3 V, but can be turned on at voltages as low as 1 V at the cost of lower torque. For the Tx coil, L_2 was used. To achieve bidirection, 2 frequencies are needed, so a total of 4 Rx coils were used for this experiment. The Rx coils were placed at a vertical distance of 13.3 mm and evenly distributed radial distance of 15 mm away from the Tx coil. To complete the rest of the two circuits, Schottky diodes (SB150-E3/54, Vishay), capacitors for f_1, f_2, f_4 and f_5 from Table 4.3, and 1 uF smoothing capacitors across the two motors were used. The capacitors were used to match the f_0 of Rx coils such that 42 and 78 kHz was used for the motor on the left and 30 and 66 kHz was used for the motor on the right. The Arduino was used to binary count using the 4 frequencies, starting with 30 kHz and ending with 78 kHz, to transmit power using the PSRG and test all possible combinations.

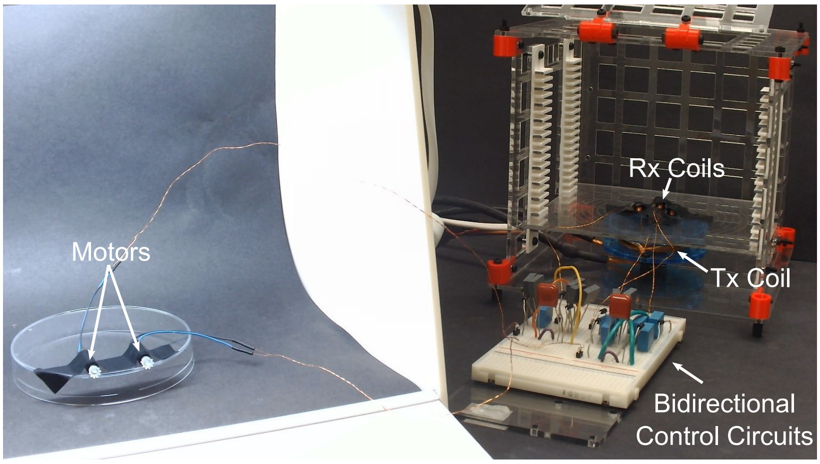

Fig. 4.12 Experimental setup used to test the bidirection motor control with 4 frequencies.

4.4.8 Heating Test

Heat can be achieved using a resistor as the load of the circuit as when current passes through a resistor, resistance to the motion of electronics generates thermal energy. To test the performance of how much heat can be produced using this system, an SMD 0603 22 Ω resistor was used as the AC load of a series LCR circuit and two set of experiments were carried out. L_2 was used as the Tx coil. The first one was carried out for all 6 frequencies, one at a time, for a fixed distance of 8.3 mm away from the Tx coil. The second experiment was carried out for a fixed frequency of 54 kHz but 3 different distances, 8.3, 13,3 and 18.3 mm away from the Tx coil were used. To measure the temperature of the resistor, a thermal camera (C3-X, FLIR) was used. Heat was applied for 30 seconds and the resistor was left to cool for 1 minute. Each trial was repeated 3 times for both experiments. The experiments were carried out at room temperature.

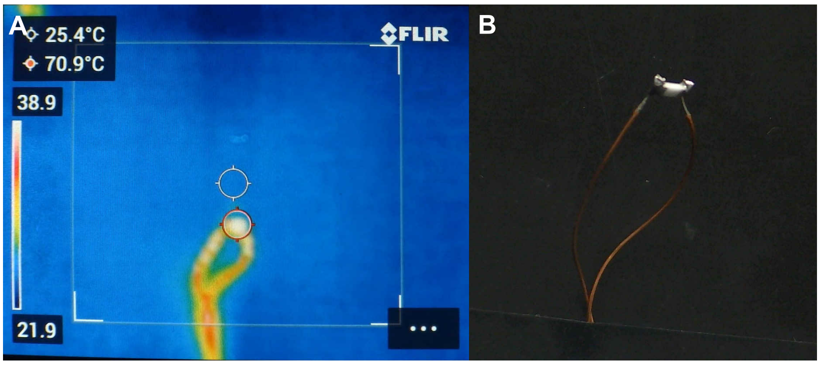

Fig. 4.13 Experimental setup used to test the SMD resistor temperature. (A) Image from the thermal camera (C3-X, FLIR) display. (B) Image of the target SMD resistor that is being heated.

4.4.9 LED Test

The parallel LCR circuit with DC load was tested using LEDs as diodes. L_2 was used as the Tx coil. To make up the circuit, 1206 Red, Green and Blue LEDs were used as the diode, SMD capacitors were used to match the resonant frequency and 1 kΩ resistors were used. The LEDs require less power to turn on than motors or generating heat, so a relatively large resistor can be used. Since this circuit is a parallel one, increasing the resistance increases the quality factor, which improves selectivity. The Rx coils were placed at a vertical distance of 43.3 mm and evenly distributed radial distance of 37.5 mm away from the Tx coil. The bottom 3 LEDs represent the bits 1-3, from right to left, where Red, Green and Blue LEDs were used for bit 1, 2 and 3 respectively. The top 3 LEDs uses the same configuration for the last 3 bits.

4.5 Results and Discussion

4.5.1 Transmission Analysis

The Tx coil current data in Fig. 4.14 A (i) shows that the largest inductor, L_3 draws the least amount of current as expected. There is a sharp fall of current past 54 kHz which could be due to the cut-off frequency of the inductor. The cut-off frequency of an inductor depends on the inductive and resistive elements of the components forming a low-pass filter. Past this value, the current that can be pushed decreases as the frequency increases. The current for L_1 and L_2 also reduces with increasing frequency, but the decrease is significantly less. Within the frequency range used, the peak current ranges from 1.5 to 4.4 A for L_3 and from 3.7 to 5 A for L_1 and L_2.

The same pattern from the current data can be seen in Fig. 4.14 A (ii) for the peak magnetic flux density. L_3 produces the largest amount of magnetic flux density, but it falls sharply with increasing frequency, whereas the magnetic flux produced by L_1 and L_2 are more consistent across the frequencies. Even though L_1 and L_2 draw very similar amounts of current, L_2 still produces a larger magnetic flux due to the inductance being larger but not large enough to go past its cut-off frequency.

The error in superposition shown in Fig. 4.14 A (iii) indicates that L_3 had maximum error of 51% when sending all 6 frequencies. A 50% error in superposition means that half as much of power can be delivered to the Rx compared to when sending 1 frequency. This effect does not only reduce the power delivered to the correct set of frequencies but also increases the power delivered to the unwanted frequencies. The overall selectivity of the system is reduced rather than just a net power loss to the target. 0% percent error in superposition means that the waveform was recreated perfectly. The effects of the larger inductance of L_2 is a little more visible in the error values as even though both L_1 and L_2 produce consistent magnetic flux densities across the frequencies, L_2 consistently has more error in superposition than L_1.

Superposition creates peaks and trough that require fast changes in current and larger peak amplitudes. An increase in inductance limits the ability of the inductor being able to pass the larger rate of change of currents due to the increased reactance, thus has an increased error in superposition. This indicates a delicate balance is needed in choosing the right inductor size for the frequency range that is to be transmitted. The inductor should not transmit a frequency past its cut-off frequency that would limit the current through the inductor, but also aim to use the largest possible inductance to produce the largest magnetic field.

4.5.2 LT Spice Simulation

Fig. 4.14 B shows the results of the LTspice simulation for the Tx/Rx relationship using the Tx coils L_1, L_2 and L_3 transmitting to the Rx coil L_{Rx}. The simulation inspects the single frequency transmission using measured values of the mutual inductance coefficient and provides extrapolated frequencies up to 200 kHz not used in the rest of the experiments. All the values for the simulation are for peak values rather than RMS values used in the measured

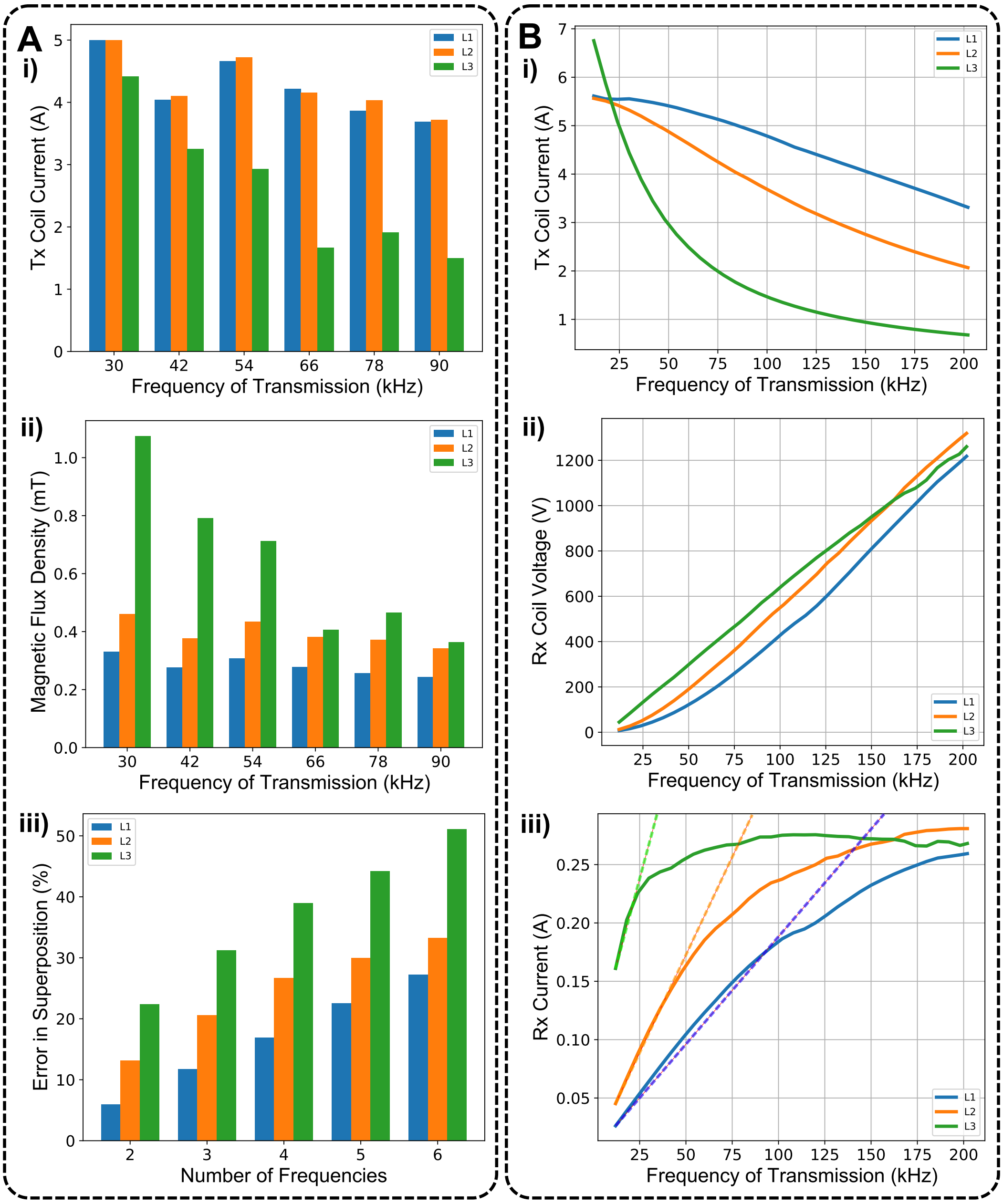

Fig. 4.14 Transmission characteristics of the PSRG system. The inductance of the Tx coil determines the suitable range of frequencies to be used. (A) (i) Shows measured data of the peak transmission coil current, (ii) The peak calculated magnetic flux density at 18.3 mm away from the top of the coil and (iii) shows the relative error in superposition with increasing number of frequencies, based on the measured RMS currents from the output of the PSRG system. (B) Shows data gathered from LTspice simulations for the PSRG system with 1 Ohm load on a series LCR receiver. The simulation uses measured mutual inductance coefficient values. (i) Shows the Tx coil current, (ii) shows the voltage across the Rx coil and (iii) shows the current in the receiver, which is also equal to the voltage across the load.

results. Fig. 4.14 B (i) shows very similar trend for L_3 with the measured results but expected a larger current difference between L_1 and L_2. This could be due to the internal resistance of the CI-Array inductors limiting the flow of current, regardless of the inductance size. Potentially, using lower resistance larger inductors for the CI-Array could show different measured results.

Fig. 4.14 B (ii) shows that the voltage across the inductor of the receiver increases linearly with frequency. This is due to the voltage being dependent on the flux linkage between the two coils and the frequency. Since the flux linkage stays constant, the only changing factor is the frequency of transmission.

Fig. 4.14 B (iii) shows the current induced in the Rx circuit, which is also equal to the voltage across the 1 Ω load. The effects of the reduced current in the Tx coil is also seen in the current induced in the Rx coil. Overall, for a single frequency, L_3 results in the largest current in the Rx, but the increase in current levels off around 50 kHz. The linear region of the increase in current indicates the range of frequencies unaffected by the cut-off frequency of the Tx coil. This region is the part where the error in superposition can be kept to a minimum. The results of the simulation indicate that the linear region ends at around 25 kHz for L_3, 50 kHz for L_2 and 100 kHz for L_1. The region where the error in superposition would be large enough for ON Rx state to be indistinguishable from OFF Rx state is the part where the current through the Rx coil levels off. As frequency increases, the voltage that needs to be applied to the Tx coil to keep supplying the same current increases. The superposition of frequencies create peaks that require fast changes in current. Since the voltage supply is constant, going beyond the cut-off frequencies of the Tx coils makes it increasingly difficult to re-create the superposed signals. For L_3, this happens around 50 kHz, for L_2 around 200 kHz and for L_1, the level off is not visible within the bounds of the simulation.

4.5.3 Frequency Domain Analysis

The waveforms used for the current measurements have also been used for an FFT analysis (without the low-pass filter) to analyse the frequency domain components of the transmission. An example of the waveforms are shown in Fig. 4.15. The waveforms chosen highlights 30 kHz and 42 kHz separately and then mixed, as well as the waveform of when all 6 frequencies are being transmitted. An inspection of the waveforms in Fig. 4.15 A and B shows that the single frequency waveforms for 30 kHz and 42 kHz for L_1 and L_2 resemble a triangular waveform rather than a sinusoidal one. Results of L_3 shows that the triangular waveforms are also being deformed additionally due to the reactive component of the inductor, causing slow fall times. This suggests that the triangular waveforms are not caused by the self-inductance of the Tx coil.

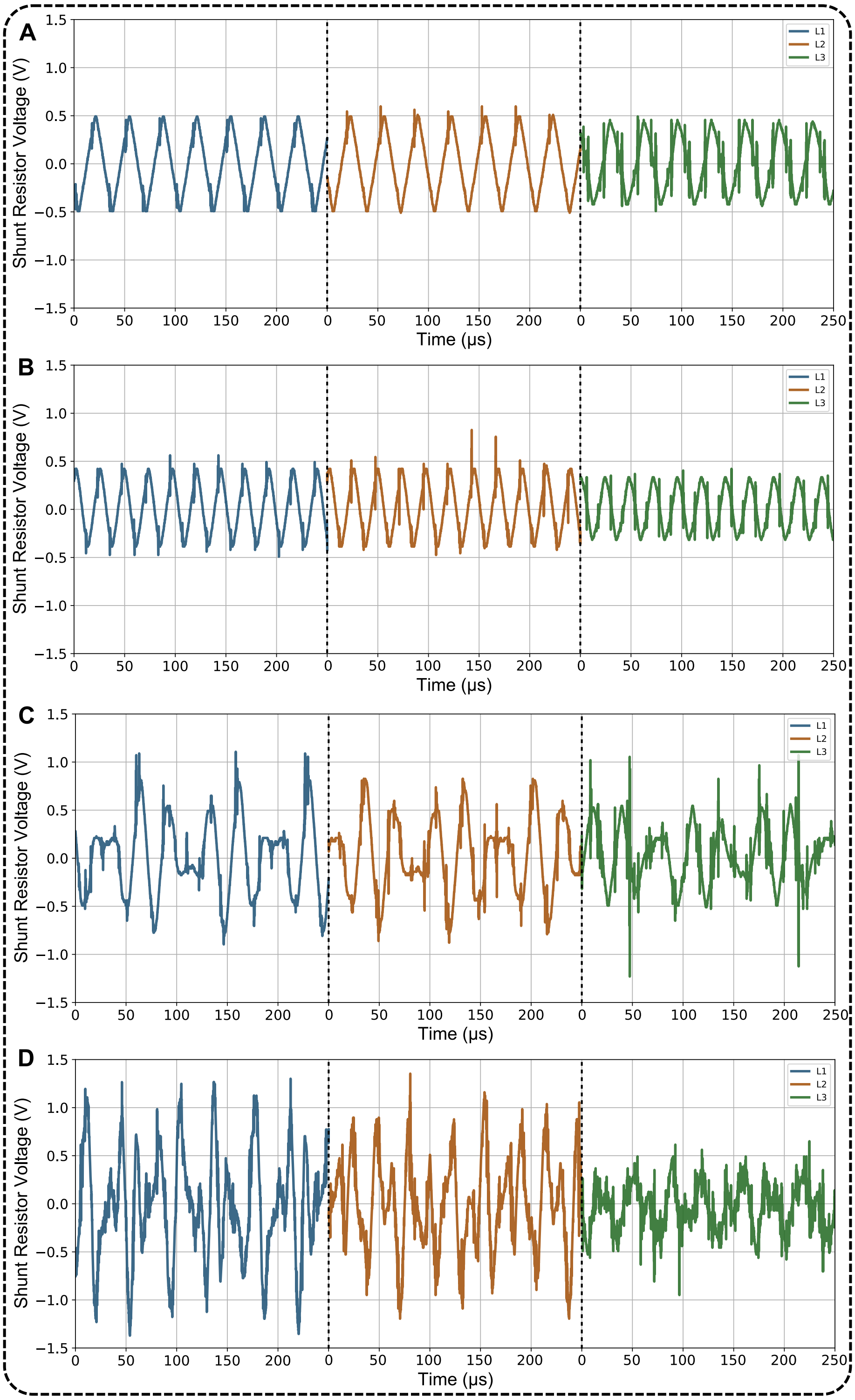

Fig. 4.15 Collected waveforms across the shunt resistor for voltage reading versus time. The waveforms have been spliced together with 250 μs intervals for better readability. (A) Represents when 30 kHz is being transmitted, (B) 42 kHz, (C) 30 kHz and 42 kHz and (D) all 6 frequencies.

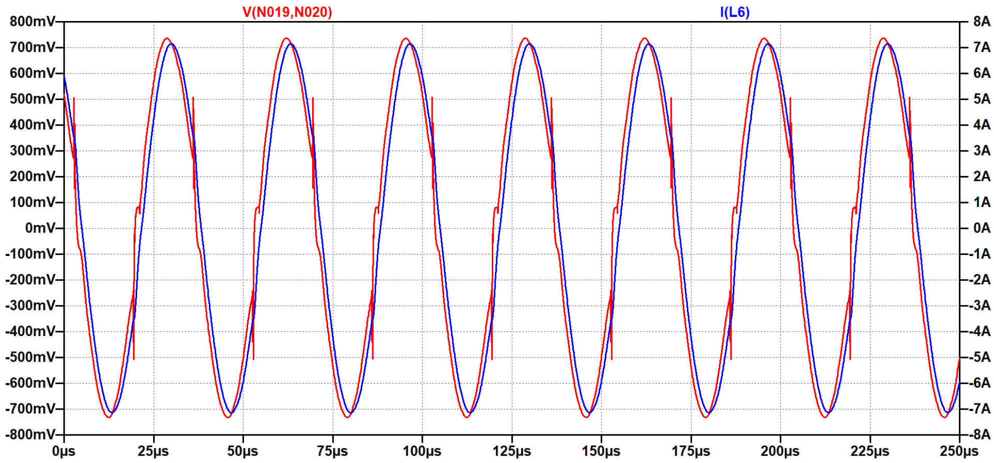

Fig. 4.16 Waveforms from LTspice simulation for the PSRG system with the Tx coil L2 transmitting 30 kHz. The red trace labelled "V(N019,N020)" shows the voltage across the shunt resistor with the y-axis on the left and the blue trace labelled "I(L6)" shows the current across the Tx coil with the y-axis on the right.

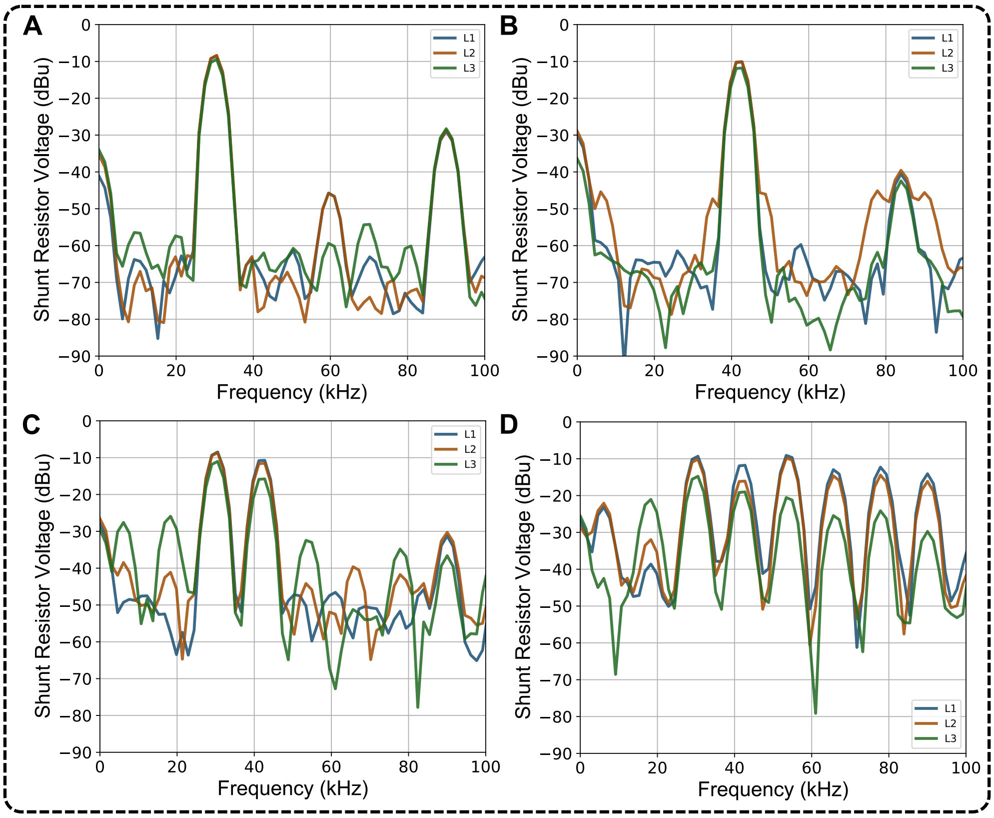

Fig. 4.17 Frequency domain representation of the measured waveforms across the shunt resistor for the relevant frequencies up to 100 kHz. (A) Represents when 30 kHz is being transmitted, (B) 42 kHz, (C) 30 kHz and 42 kHz and (D) all 6 frequencies.

Fig. 4.16 shows LTspice simulated waveform for when only 30 kHz is being transmitted. The simulation uses perfectly matched CI-Arrays for the PSRG modules and a simulation of the shunt resistor with 0.1 Ω DC resistance and 0.1 μH inductance in series and a 140 pF capacitor in parallel for scope capacitance. The simulation shows a much more uniform sinusoidal waveform compared to the measured results, which indicates that there may be error in the resonant frequency of the CI-Arrays. The shunt resistor measurement is also sinusoidal which can rule out the measurement method causing the triangular waveforms. The two important reasons that the resonant frequency of the CI-Arrays being mismatched is that when building the modules, the inductance and capacitance values were read with the LCR meter only rather than using a frequency sweep method. Another potential cause is that the inductors used for the CI-Array have iron cores. The self-inductance of an inductor with an iron core decreases with increasing current and/or frequency, the ratio of which depends on a number of variables such as permeability of the iron core and the physical properties of the coil winding such as number of turns and coil wire thickness. This could be an issue as the LCR meter measurements does not take into account the difference high current makes in the self-inductance. The system performance should improve with a more accurately built CI-Array.

Comparing the shunt resistor voltage of the measured results in Fig. 4.15 A for L_2 with the simulated results in Fig. 4.16, the high frequency noise appears regularly in both but not in the simulated current across the Tx coil, which indicates that some or most of the high frequency noise is caused by the measurement method. The peak values are also different as well, where measured results show 0.5 V whereas simulated ones show 0.7 V, which again could be due to mismatched CI-Array resonant frequency or resistance unaccounted in the simulation such as PCB trace or wire resistances including resistance caused by heat.

Fig. 4.17 shows the frequency domain trace of the same waveforms from Fig. 4.15 for a range of 0 to 100 kHz. The trace in Fig. 4.17 A and B show that all Tx coils have a peak of around -10 dBu for 30 kHz and 42 kHz. The trace also shows that when 30 kHz is being transmitted, there is a -30 dBu harmonic component at 90 kHz for all Tx coils. When both 30 and 42 kHz are being transmitted in Fig. 4.17 C, a reduction can be seen in the peaks in the results of L_3, especially for 42 kHz. The same trend for L_3 continues in Fig. 4.17 D when all 6 frequencies are being transmitted. The values for 30 kHz and 42 kHz are further reduced, and all other transmitted frequencies have smaller peaks with increasing frequency. An important note is that the peak of 90 kHz when all 6 frequencies are being transmitted is smaller than the peak seen in the 90 kHz harmonic component of when 30 kHz is being transmitted. Some decrease in peak values for L_1 and L_2 can also be seen, but the difference is much smaller.

The decrease at 42 kHz seems unusual compared to the expected trend, but result is still above -20 dBu, which distinguishes it from when 42 kHz is not being transmitted.

Using the same method to inspect the frequency domain components of the waveforms, the values of all 6 frequencies for all 63 Tx coil states were recorded to plot the results in Fig. 4.18. The distribution in this plot represents the data collected across the 6 frequencies and not error. The data is grouped together when the frequencies are being transmitted as "On" and when not being transmitted as "Off". Then the data is broken down into number of frequencies being transmitted at the same time. Taking the 30 kHz data from Fig. 4.17 A as an example, the "On" frequency at 30 kHz has a peak of around -10 dBu, but all other 5 frequencies, grouped as "Off", has a range of results, which is represented by the distribution here.

The data in Fig. 4.18 reveals that there is no overlap for "On" and "Off" values for L_1 and L_2, but there is a significant overlap between the minimum "On" values and maximum "Off" values for L_3 when more than 3 frequencies are being transmitted. The values are also very close when 3 frequencies are being transmitted. The overlap is a problem if all devices need the same energy to be powered. There needs to be a clear distinction between "On" or "Off" energy levels transferred to the device. Also, the range of "On" values for L_3 is larger compared to the other two coils as it is harder for the larger self-inductance coil to produce higher frequency transmission, which creates a larger difference between the 6 frequencies being transmitted. All "On" Tx coil values decrease as number of frequencies increases, but decrease is more significant for L_3. As the number of frequencies increase, it becomes harder for the larger Tx inductor to re-create the peaks of superposition, thus reducing the overall accuracy of the waveform. All outlier values at around -30 dBu for 1 frequency "Off" values are caused by the 90 kHz harmonic component of 30 kHz. The "Off" values for all Tx coils shows a level off around -30 to -40 dBu as the number of frequencies increases. Around -30 dBu seems to be where the peak levels off for "Off" values when the "On" values are around -10 to -15 dBu. The "Off" values increasing is caused by harmonic distortion and added noise as number of frequencies being transmitted increases, but the reason for the value of this ceiling or why it levels off may need further investigation to explain. The main conclusion that can be drawn is that the results show that for a range of 30 kHz to 90 kHz and 6 addressable components, L_1 and L_2 are suitable, but not L_3. Further tests may be carried out to find the limits of L2 by increasing the range and number of frequencies using the same methodology.

A closer inspection of when 5 frequencies are being transmitted shown in Fig. 4.19, highlights the problem with L_3 using this range of frequencies. There is a clear distinction between "On" and "Off" values of L_1 and L_2, but L_3 shows that there is an overlap of the

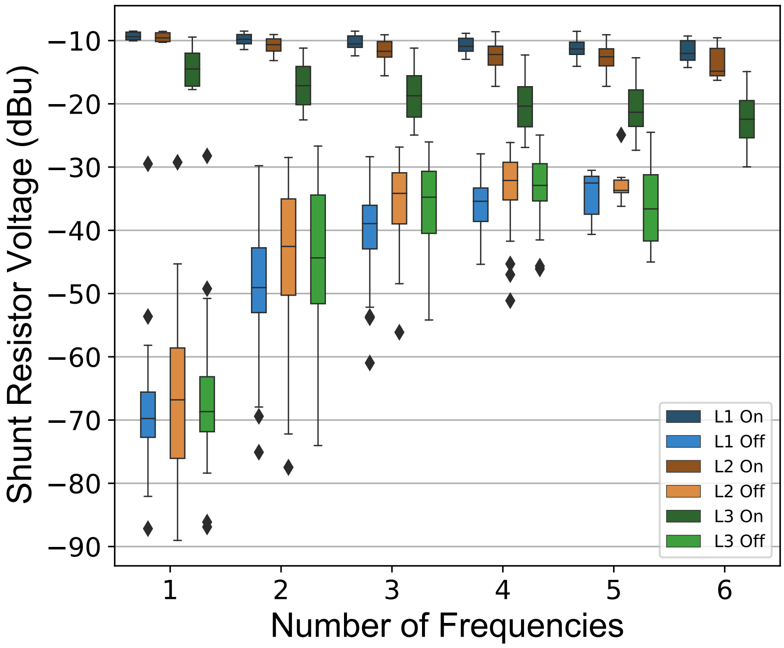

Fig. 4.18 Frequency domain analysis of the Tx characteristics. The box plots shows how the voltage read across the 0.1 Ω shunt resistor changes with increasing number of frequencies. The distribution represents data across frequencies from 30 kHz to 90 kHz, rather than the distribution of error in same conditions.

"Off" value of L_3 at around -25 dBu with the "On" values of 66 kHz, 78 kHz and 90 kHz. The combination of lower overall current being transmitted for all frequencies and the current decreasing as frequency increasing makes L_3 unsuitable for this range and number of frequencies. Since both L_1 and L_1 show significant distinguish between On and Off values, but L_2 produce a larger magnetic field overall shown in Fig. 4.14 A (ii), L_2 is likely to be the best choice.

THD levels can be a good indicator of waveform quality, as it is compared to a pure sinusoidal wave. Fig. 4.14 A shows that, L_1 has a maximum THD of around 11% at 78 kHz and 90 kHz, L_2 around 12.5% at 90 kHz and L_3 around 13.5% at 66 kHz. The THD for L_3 seems to decrease as frequency increases, which can be explained by the current also decreasing as frequency increases, further deforming the triangular waves into more sinusoidal ones. Fig. 4.14 B shows that there is also a significantly higher difference between THD and THD with noise for L_3,which suggests the noise increases with increasing self-inductance of Tx coil. However, whether this noise is only due to the measurement method or because additional problems exist in system such as current reflections or interference between wires and PCB traces is unknown and may require further testing to confirm.

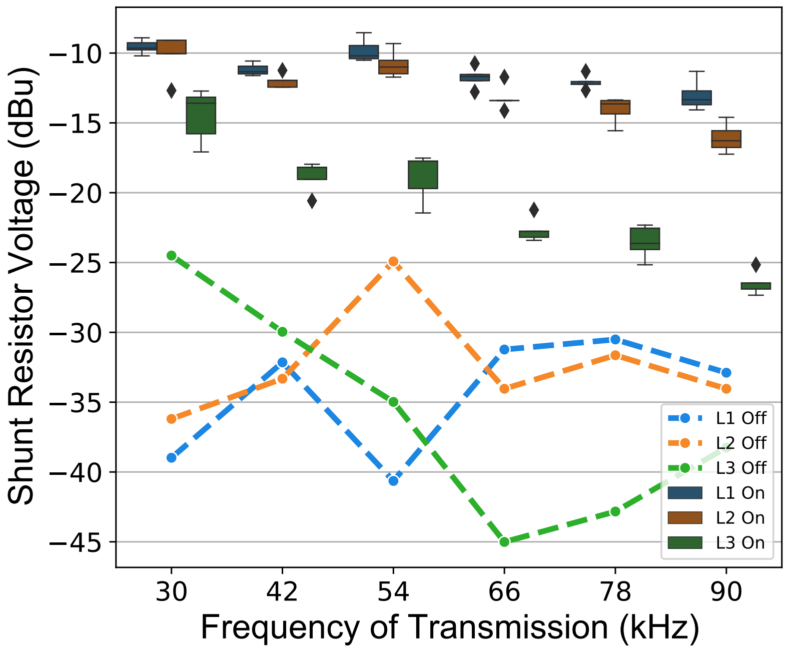

Fig. 4.19 Frequency domain analysis of the Tx characteristics using the voltage readings across the 0.1 Ω shunt resistor when 5 frequencies are being transmitted. When 5 frequencies are being sent, there are multiple instances for each frequency being transmitted, the distribution of which is represented by a box plot, but only one combination when it is not being transmitted, represented as a line.

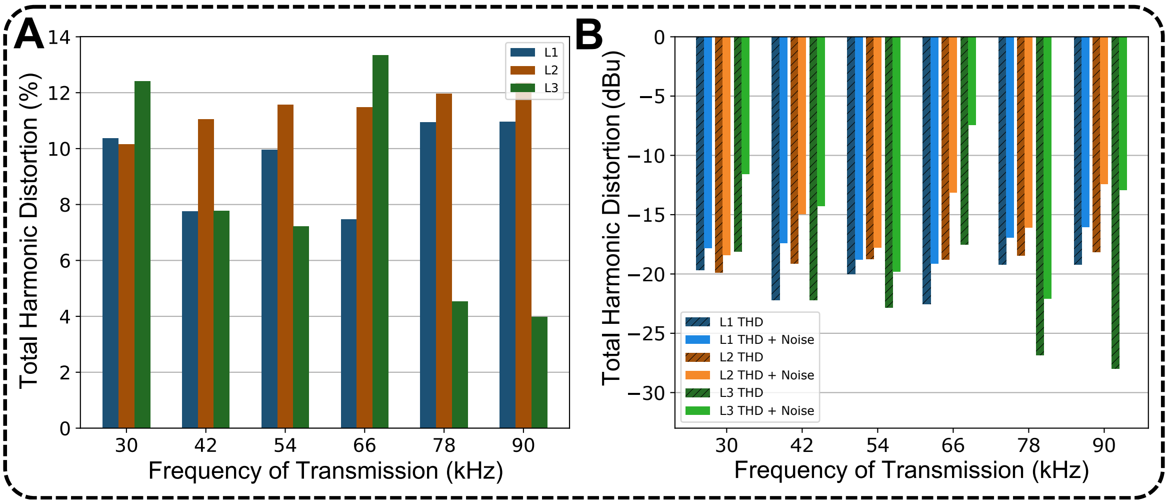

Fig. 4.20 Frequency domain analysis of the Tx characteristics showing for the THD of single frequency transmission. (A) Shows the THD (%) of the waveforms read across the shunt resistor for each frequency. (B) Shows the THD and THD + Noise (dBu).

4.5.4 Receiver Analysis

The Rx side has been measured for two different loads, one for a 1 Ω load shown in Fig. 4.21 and for 20 Ω load shown in Fig. 4.22. All the results are for a fixed distance of 18.3 mm away from the Tx coil.

Both Fig. 4.21 A (i) and Fig. 4.22 A (i) show that the current in the ON Rx state when L_3 is used reduces as the number of frequencies increase, whereas the change is less noticeable for L_2 and there is almost no change for L_1. The range for 1 Ω is from 44.7 to 89.8 mA for L_3, from 39.6 to 54.4 mA for L_2 and from 28.7 to 33.8 mA for L_1. The range for 20 Ω is from 30.5 to 63.6 mA for L_3, from 28.6 to 40.9 mA for L_2 and from 19.5 to 23.3 mA for L_1. The reduced current for 20 Ω is expected due to the higher resistance, but the trend remains the same. The power delivered to the 20 Ω load in Fig. 4.22 B (i) however is almost 10 times to the power delivered to the 1 Ω load in Fig. 4.21 B (i). The power delivered is increased because more power is dissipated across the resistor at the cost of reduced current, but the increase in power will fall if the resistance of the load is large enough that the loss in current becomes a limiting factor compared to the 15 Ω DC resistance of the L_{Rx}.

The error in superposition for Rx ON state current shown in both Fig. 4.21 A (ii) and Fig. 4.22 A (ii) follows the same trend as the Tx current error in superposition in Fig. 4.14 A (iii) for L_3 and L_2. However, L_1 on the Rx side exhibits around 15% error in superposition for 6 frequencies, which is almost half as much as error compared to the Tx side. A 50% Rx ON state error in superposition means that the Rx circuit received half as much as power compared to when a single frequency was being sent. A larger percentage indicates a larger reduction in current or power for the Rx ON state.

Fig. 4.21 B (ii) shows a reduction of power by 44.30% and Fig. 4.22 B (ii) by 50.08% when number of frequencies are increased from 1 frequency to 6. If FM was used for this application instead of superposition, only 1 frequency can be sent at a time for the same duration, which means that one receiver can only receive power for only $1/6^{th}$ of the time. If there were 2 addressable components, for the same time span, frequency and magnetic flux density, power transmitted to the receivers would be reduced by 50% since only one frequency can be transmitted at the same time and there are two frequencies. Extending this logic to 6 addressable components equate to a reduction of power by around 84%.

As explained in the Tx side analysis, the error in superposition also affects the Rx OFF state whereas the number of frequencies increase, the current and power in the Rx OFF state also increase. A 50% OFF Error in superposition means that the Rx OFF state has received half much as current or power when compared to the lowest Rx ON state current or power when all 6 frequencies are being transmitted. A larger percentage indicates a worse distinction of Rx OFF state from Rx ON state. Since voltage dropped across the load is

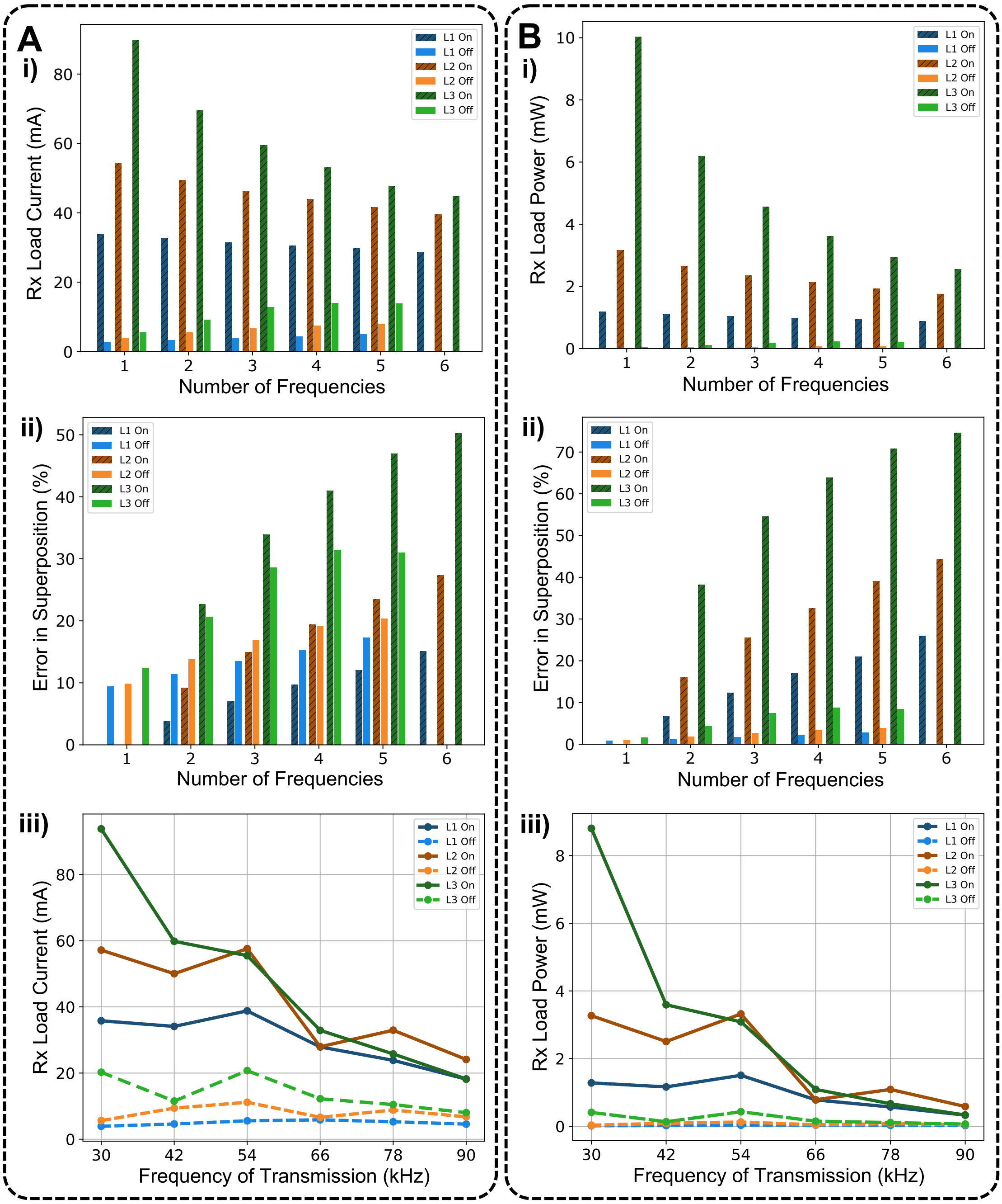

Fig. 4.21 Receiver characteristics of PSRG with a 1 Ω load in a series LCR circuit. Data was collected for the 63 combination of 6 frequencies, for 6 Rx circuits at distance of 18.3 mm away from the Tx coil. On and Off refers to Rx ON state and Rx OFF state. (A) (i) Shows the data for the measured voltage/current across the load. (ii) Shows the relative error in superposition. (iii) Shows the Rx load current across the 6 frequencies when a combination of 5 frequencies are being transmitted at a time. (B) Shows the same information for power delivered to the load, calculated from the load voltage.

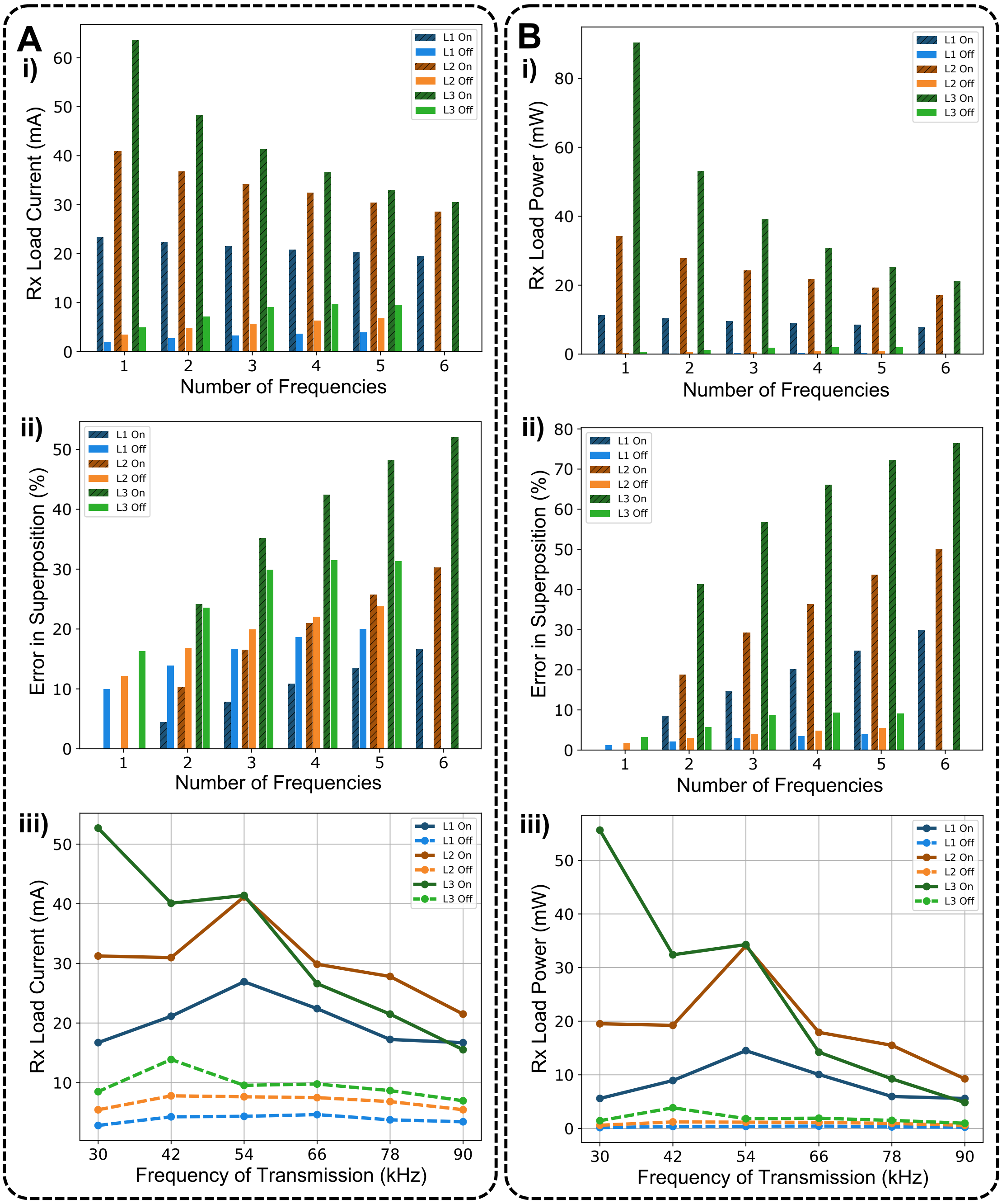

Fig. 4.22 Receiver characteristics of PSRG with a 20 Ω load in a series LCR circuit. Data was collected for the 63 combination of 6 frequencies, for 6 Rx circuits at distance of 18.3 mm away from the Tx coil. On and Off refers to Rx ON state and Rx OFF state. (A) (i) Shows the data for the measured voltage/current across the load. (ii) Shows the relative error in superposition. (iii) Shows the Rx load current across the 6 frequencies when a combination of 5 frequencies are being transmitted at a time. (B) Shows the same information for power delivered to the load, calculated from the load voltage.

linear to the current and power is a function of both, the effects of error in superposition is amplified when power values are used. Fig. 4.21 B (ii) and Fig. 4.22 B (ii) show that error in superposition for Rx ON state is higher than when current values are used, but the Rx OFF state error is lower as well since Rx OFF state is relative to the smallest ON value, therefore ability to distinguish between ON and OFF state remains the same. Whether to use power values or current values to set the boundaries depends on the load.

Fig. 4.21 A (iii) and Fig. 4.22 A (iii) shows how the current is distributed across the frequencies when 5 frequencies are being sent at a time. The data for 5 frequencies were chosen as it is harder to superpose larger number of frequencies due to larger peak amplitudes, but also for 6 frequencies, 5 frequencies is the largest number of frequencies where there are measurements for OFF Rx State for comparison of the performance. For L_3, the current for ON Rx State sharply falls after 30 kHz, but still distinguishable from OFF Rx State up to 54 kHz. Past 54 kHz, the difference between ON and OFF becomes very close. For L_2, including 66 and beyond, current for ON Rx State falls, but it is still distinguishable from OFF Rx State. L_1 has the lowest current for both ON and OFF Rx State, but throughout all frequencies there is no sharp fall. The results from Fig. 4.22 A (iii) are consistent with the linear region and level-off boundaries from Fig. 4.14 B (iii) on the receiver side as the current and power falls sharply after 30 kHz for L_3, after 54 kHz for L_2 and not distinctly visible for L_1. One difference is, comparing the simulated results to the measured results for the frequency between 30 kHz to 90 kHz, all Tx inductors shows that in simulation, the current in Rx slows down and levels-off, whereas in the measured results, the current decrease with increasing frequency. This might be due to the simulation ignoring that the receiver inductor has a ferrite core. A higher frequency might be reducing the inductance of the receiver, which makes its resonant frequency deviate.

Table 4.5 shows the percentage difference between the minimum Rx ON state and maximum Rx OFF state for the data in Fig. 4.21 A (iii) and Fig. 4.22 A (iii). The higher percentage is, the better. 0% and below means that Rx ON state cannot be distinguished from Rx OFF state and 100% means that the Rx ON state is double the current or power of Rx OFF state. This comparison is relevant if the same load is used for all frequencies, as all the loads will have the same boundary for the minimum current or power necessary to turn the load on. As the distance away from the Tx coil increases, all Rx ON state current and power will decrease. This means that a higher percentage results in a larger usable range of distance away from the Tx coil.

Table 4.5 Percentage Difference Between Minimum ON and Maximum OFF Rx State

Condition	L_1 (%)	L_2 (%)	L_3 (%)
1 Ω Load Current	67.71	53.66	-13.80
1 Ω Load Power	89.59	78.59	-29.23
20 Ω Load Current	72.20	63.75	10.59
20 Ω Load Power	92.28	86.88	20.17

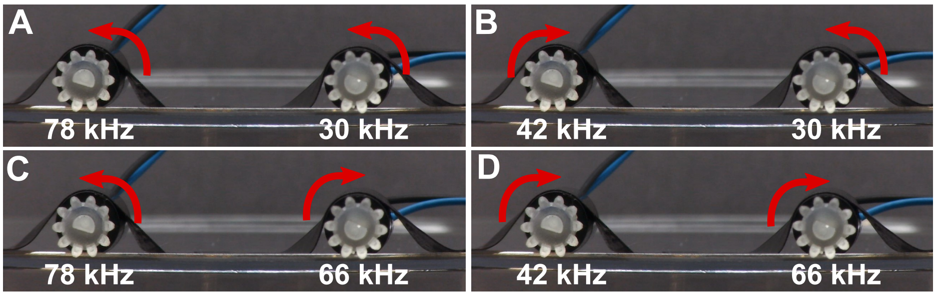

Fig. 4.23 Experimental results for the bidirectional motor control. In this experiment, 42 and 78 kHz was used for the motor on the left and 30 and 66 kHz was used for the motor. The 4 Rx coils were placed at a vertical distance of 13.3 mm and evenly distributed radial distance of 15 mm away from the Tx coil. (A-D) Shows all 4 possible combinations of frequencies and the resulting direction of the motor rotation is marked with a red arrow.

4.5.5 Bidirectional Motor

The results of the motor test shown in Fig. 4.23, confirms that it is suitable to control 2 motors bidirectionally, without using any active electronic components, but instead using the bidirectional control circuit from Fig. 4.8 D. Two frequencies are needed per direction and a total of 4 frequencies and 4 L_{Rx} were used for this experiment. All 15 combinations of 4 frequencies were tested. The motors spin to the direction the frequency is designated for, independent of each other, when the correct frequency is sent. When the frequencies designated to the same motor is sent at the same time, for example, 30 kHz and 66 kHz to the motor on the right, the motor stays stationary. The results were correct up to 13.3 mm vertical distance and 15 mm radial distance away from the Tx coil, but had inconsistent results at 18.3 mm vertical distance away. This means that improvements needs to be done on the transmission side or on the energy requirements of the actuator for the system to be clinically viable, given that a distance larger than 30.9 mm would be needed to provide access from outside the body [54]. Individually, the motors can be turned on from up to 28.3 mm for single frequency without a radial offset from the centre of the Tx coil. For this experiment, results from the radially distributed Rx coils were chosen to be presented because it is a more realistic use case scenario that the Rx coils are present on the test platform at the same time.

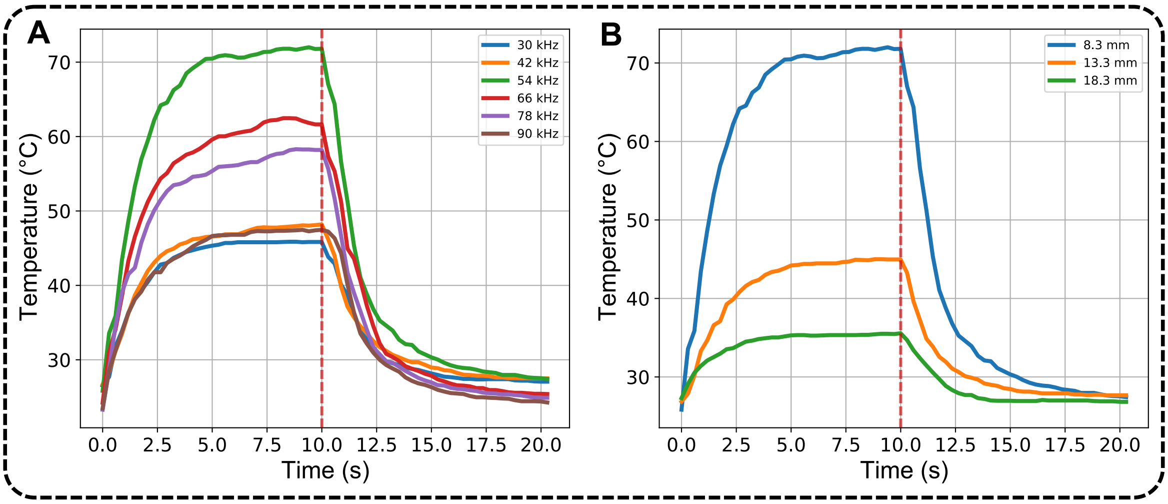

Fig. 4.24 Experimental results for the SMD resistor heating. (A) Shows the data for heating across all 6 frequencies over time for a fixed distance of 8.3 mm away from the Tx coil. (B) Shows the data for heating at a fixed frequency of 54 kHz over time for 3 different distances. The dotted red line shows the point where the heating data was cut and spliced together with the cooling data as the temperature stayed relatively constant in between.

4.5.6 Heating

The results of the SMD resistor heating experiment is shown in Fig. 4.24. Even though the heating was applied for 30 seconds and the resistor was left to cool for 1 minute, the data is presented to show the first 10 seconds of heating and first 10 seconds of cooling. This is because the peak temperature was reached within 5 seconds and returned to room temperature within 10 seconds for all frequencies and all distances and stayed relatively constant for the rest. The distribution of peak temperatures across the frequencies in Fig. 4.24 A matches the 20 ohm power distribution in Fig. 4.22 B (iii) for 54 kHz, where 54 kHz receives the most power. However, 66 and 78 kHz received a larger temperature increase than 30 and 42 kHz, and 90 kHz was expected to be smaller than 30 and 42 kHz, but had a similar temperature increase instead. Fig. 4.24 B shows that the distance, and therefore the power delivered, affects temperature increase significantly. For Fig. 4.24 A, 8.3 mm results were chosen to be presented because the difference in increase in temperature is better highlighted compared to the distribution of higher distances where the difference in temperature across all frequencies is smaller. For cell necrosis, a distance of 13.3 mm is suitable from the results. It should also be considered that these experiments were carried out in room temperature in a well ventilated environment. The temperature loss coefficient is likely to be a lot smaller inside the body with an environmental temperature of 37 °C and less movement of the surrounding fluid.

4.5.7 LED

The LED test results in Fig. 4.25 highlights the distinctive capabilities of the PSRG system in delivering power to 6 addressable components in parallel, concurrently and independently, in a visual manner. With FM, addressability of SMAs were seemingly possible because of the delayed response the heating and cooling cycles they exhibit [58]. If the frequencies were transmitted sequentially with FM, the power delivered to the LEDs would have increasingly lengthy interruptions as the number of frequencies to be sent increases. The luminosity of an LED when 1 frequency is being sent would differ from the results of luminosity of 6 frequencies and would likely to flicker because of the interruptions. The results from Fig. 4.21 and Fig. 4.22 show that the average power reduces as the number of frequencies increase, but this power is delivered at the same time without interruptions. Even though the overall power delivered does decrease, this decrease is small enough that the decrease in luminosity of the LEDs is minimal without flickering, regardless the number of frequencies being sent within this example. Fig. 4.26 shows a comparison of all 6 frequencies being transmitted one by one and all transmitted at the same time to visually inspect the small amount of decrease in luminosity. The purpose of this experiment was to visually demonstrate the independent and concurrent control of 6 addressable components. Further testing may be carried out with luminosity sensors on the LEDs for more quantitative results. The results also show that, as the power necessary to operate the load decreases, the distance which this system can be used also increases, meaning that developments in lower power actuation methods could lead to more practical applications. By confirming the possibility of P-WPT for 6 addressable components, the PSRG system may be suitable to be used with faster response actuators.

4.5.8 Capsule Concept

For the motor test in Fig. 4.12, throug-hole capacitors were used to build the circuit in Fig. 4.8 D, but for the capsule, SMD versions needs to be used. The capsule design was 3D printed using an SLA printer (Form 3+, Formlabs) and the mechanism for the motor and gear set was assembled, tested and found to be working. The SMD version of the components were tested and confirmed that they do fit into the capsule. One difficulty to be noted comes from matching ceramic SMD capacitors to the resonant frequency as ceramic capacitors increase in capacitance of around 5% and slowly degrade over time. The capacitors that are used to match the resonant frequency also need a high voltage capacity as the potential difference needed to sustain the reactive energy of large self-inductance of L_{Rx}. The SMD capacitors that were used for this experiment had a voltage limit of 50 V, which was not enough for frequencies above 54 kHz, resulting in the capacitors to break down and malfunction. This means that the

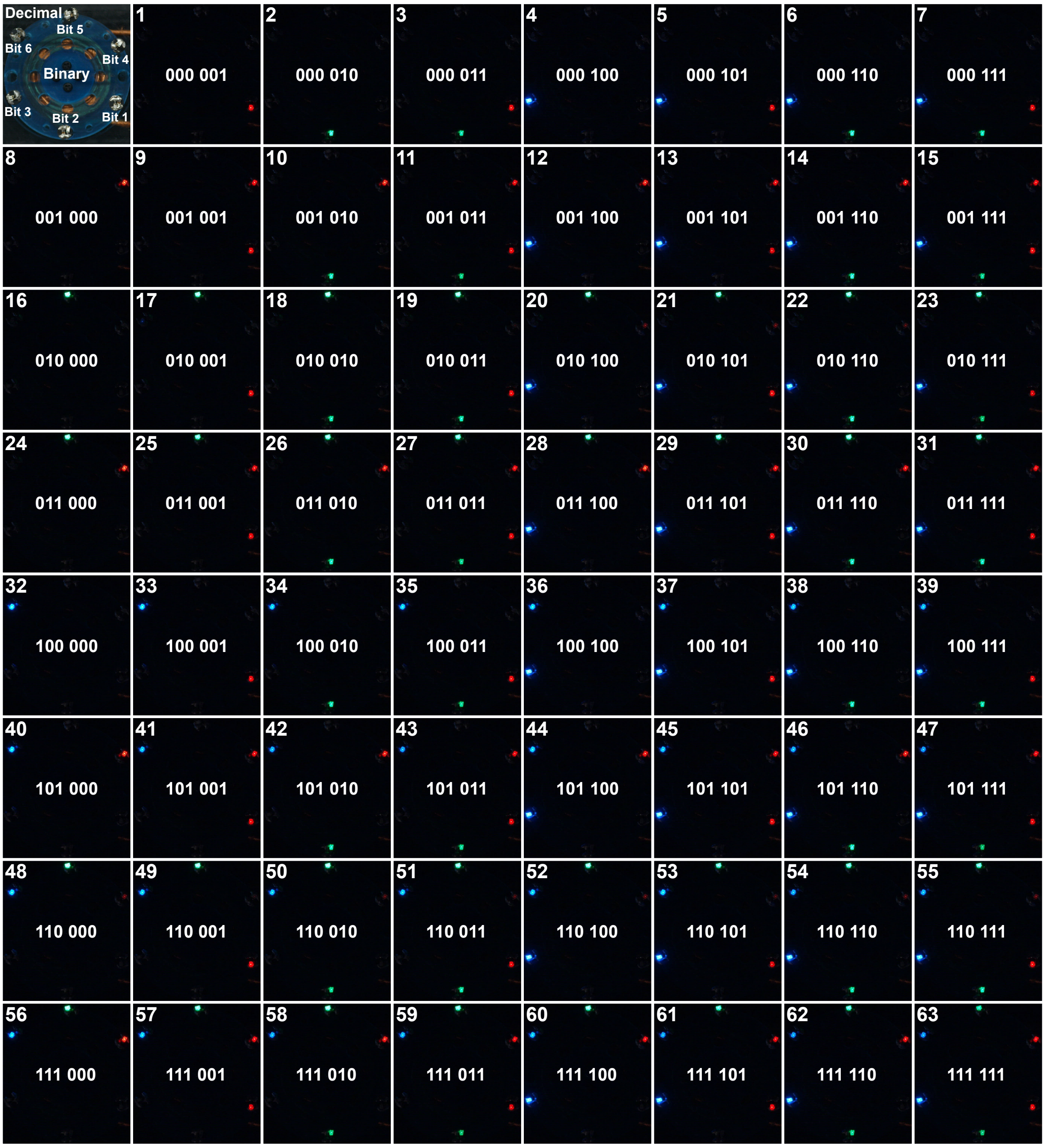

Fig. 4.25 LED mixing sequence results. LED modules are matched to the 6 frequencies. The frequencies are sent by binary counting, starting with 30 kHz as bit 1 and 90 kHz as bit 6, cycling through 63 combinations.

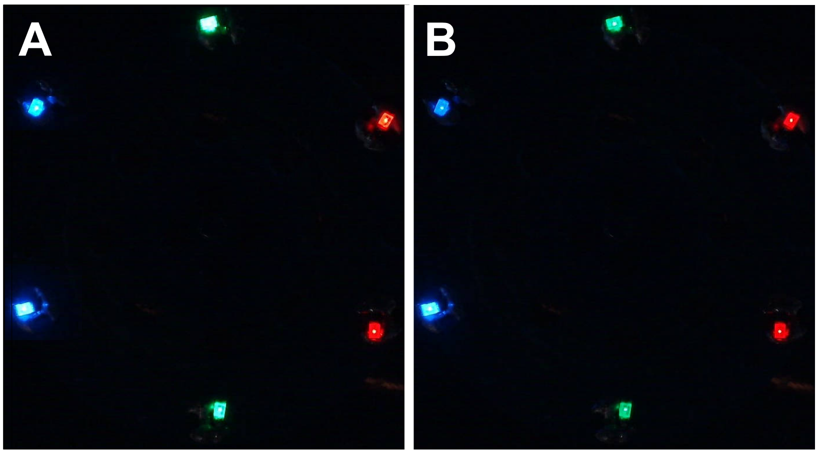

Fig. 4.26 Comparison based on the LED Results. (A) Shows a reconstructed image from every LED when only 1 frequency is being transmitted. (B) Shows the image of the LEDs when all 6 frequencies are being transmitted.

self-inductance of L_{Rx} needs to be reduced for the higher frequencies to reduce the potential difference requirements. This could be done by optimising the Rx coil geometry with one made specifically for this application that fits the endoscopic size requirements but has a better WPT efficiency while having a smaller self-inductance. Additionally, using motors that require less energy to operate or another method of actuation could improve the use case scenario and capabilities of the capsule design such as the operation distance away from the Tx coil. The design presented is similar to the self-assembling 2-DOF manipulator [3] which may be transferable to future self-assembling versions.

4.6 Conclusion

As a result of the study, a new amplifier design called the PSRG was developed, capable of superposing multiple sinusoidal magnetic fields at the Tx coil, bypassing the maximum and threshold gate-source limitations of traditional amplifiers that superpose at the input signal stage. A range of Tx coils were tested with the same Rx circuit to find out the limitations of the approach and find an optimal Tx self-inductance to be used for the range of frequencies. The Tx/Rx analysis has shown that the PSRG system is suitable to be used for 6 frequencies, which is not only double of what was achieved in literature [9, 120, 121], but also the power transfer happens independently and concurrently to each Rx Receiver. The transmission is carried out for a range of frequencies spanning from 30 to 90 kHz with 12 kHz increments, using a Tx coil of 5.44 μH. For the chosen Tx/Rx design, there is around 30% reduction in current and around 50% reduction in power received by the Rx load when 6 frequencies

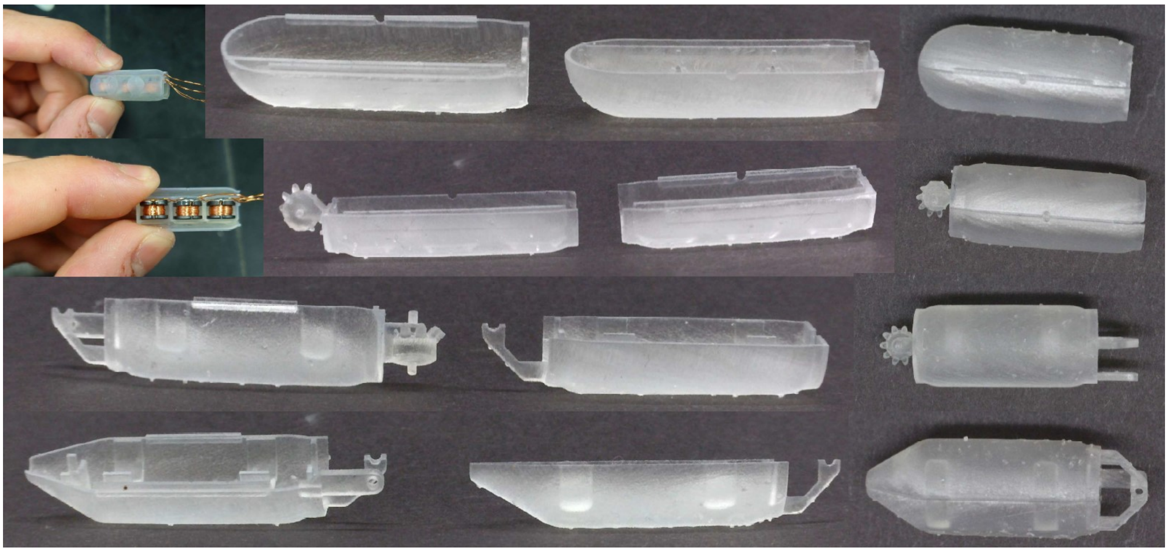

Fig. 4.27 Images of the capsule parts printed with Formlabs 3+ SLA printer.

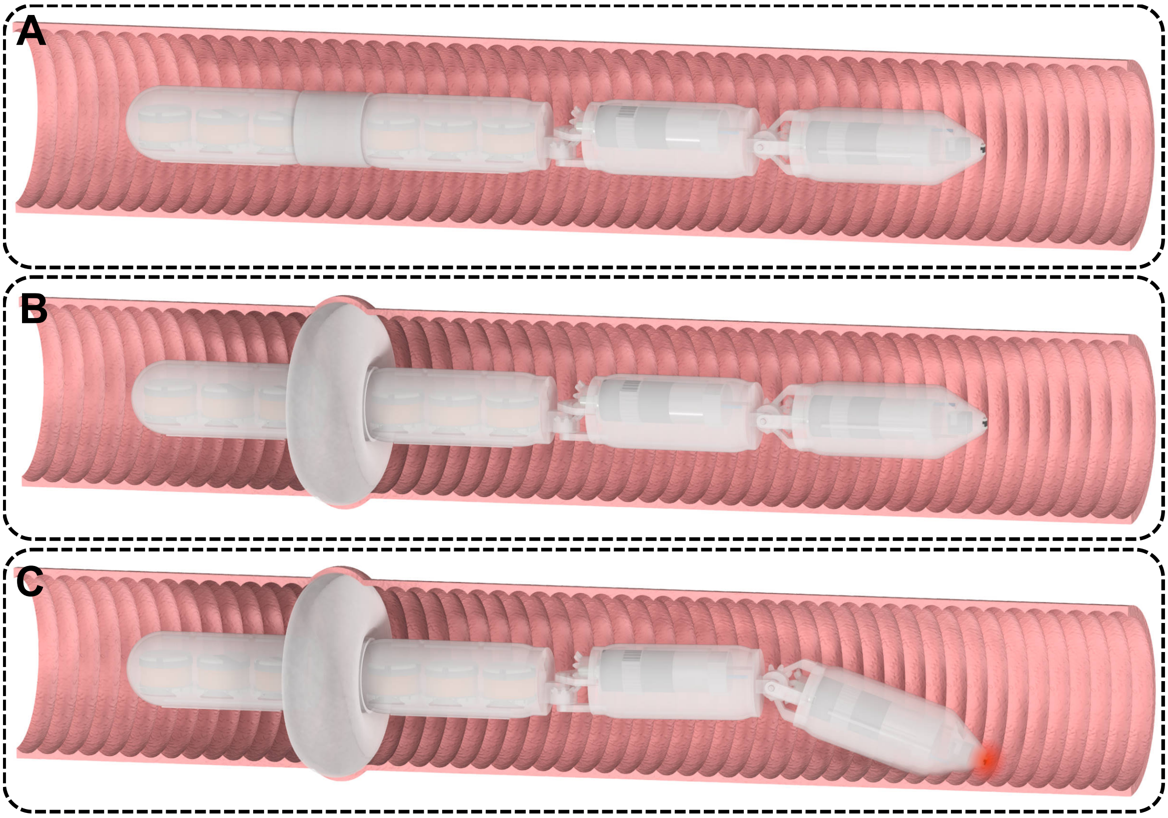

Fig. 4.28 Example use of the capsule robot using 6 frequencies. (A) Robot reaches the site of surgery. (B) Chemical reaction is triggered to anchor the capsule to the intestinal tissue. (C) The capsule tip is navigated to a target area for the heat to be applied with the SMD resistor. The heat can be used for cauterisation, patching wounds or destroying pathogens.

are being sent compared to the current and power of 1 frequency, which is a lower value of what could be achieved with FM. For the PSRG system, the net reduction in power delivery is lower, but comes at the cost of careful selection of Tx coil self-inductance and range of frequencies to be transmitted. The system can deliver an average of 28.5 mA and 17 mW to 6 frequencies at the same time, for a Tx/Rx separation distance of 18.3 mm with an input voltage of 15 V to the PSRG. The Tx and Rx side analysis carried out the methodology for choosing the right variables and expand the work in the future, adding more addressable components.

A range of applications such as heating an SMD resistor, lighting up LEDs and controlling 2 motors bidirectionally were tested with various simple Rx circuits comprised of passive components only. The bidirectional motor test has shown that using the PSRG system, 4 frequencies, 2 passive circuits and 4 Rx coils, 2 small DC motors can be controlled independent of each other. The heating test has shown that it is possible to reach temperatures of cell necrosis or cauterisation, but the PTE needs to be improved to increase the operation distance that would allow operation in the gastrointestinal tract. The LED test has confirmed that 6 frequencies can be transmitted, independently and concurrently, without significant power losses compared to sending 1 frequency that would affect the luminosity of the LEDs. The performance shown with the LEDs highlights the future potential of the system as the energy requirements of actuator are reduced through improvements by material or manufacturing means. If actuators with power requirements similar to an LED are developed, powering the capsule at a distance of 43.3 mm could make it clinically viable. Compared to the literature, the number of addressable components has been doubled and the ability of P-WPT has been introduced. A prototype capsule design has been presented that could anchor to the intestinal tissue, based on previous research, contain 6 Rx inductors, SMD components for passive Rx circuits, 2 DC motors and a mechanical design that allows 2-DOF manipulation, and a heater for cauterisation or cell necrosis. Before practical applications can be tested, the overall WPT needs to be improved.

The PSRG system can be improved by using lower resistance inductors for the CI-Array or modifications to the MOSFET routing circuit to allow a higher gate-source voltages, for example, by using multiple MOSFETs in series. Both modifications would end up with a larger current build-up and therefore, larger magnetic flux density to be produced at the Tx coil. This would also likely require a better thermal design for the MOSFET routing circuit and the CI-Array. An optimal Tx geometry was picked for the range of frequencies, but no optimisation has been carried out for the Tx/Rx relationship. Improvements to the Tx/Rx geometry relationships could improve the PTE and therefore the operating distance. Lower power requirements for the load could improve the operating distance. Only a basic circuit with SMD resistors as the source of heat was tested. The next steps could look into other options for heating, or thermoresponsive materials as the source of actuation like SMP, SMA or PNIPAM. Further developments in actuator technologies or motors with lower power requirement could help improve the practical use case scenarios of the presented capsule design and the PSRG system. The issue with high voltage requirements and the SMD capacitors breaking down could potentially be turned into an advantage by using dielectric actuators as capacitors, given that dielectric actuators' main disadvantage is high operation voltages [83–85]. The frequency range could be increased to further increase the voltage built-up at the Rx coil. It may be possible to reduce the overall capsule size by replacing the DC motors with thermoresponsive materials [89, 37, 95]. Instead of using 4 frequencies for 2 DC motors for 2-DOF, it could be used to replace wired elements of a CTE based precision instrument [8] to make a wireless guided endoscope. There also a potential to implement a closed-loop control system with RIC wireless sensors [137] to improve the surgical capabilities of the capsule robot. Despite the need for improving the PTE, the research carried out provides a new platform and methodology for P-WPT, and the Rx side analysis highlights the details necessary to be considered for the robot design. The work opens up the possibility of wirelessly controlling a single small scale robot for complex tasks or multiple smaller scale robots for simpler tasks, with minimal electronics on board.

Chapter 5

Conclusion

5.1 Discussion

From the literature review, two gaps have been identified to allow further miniaturisation of more complex therapeutic functions for capsule robots. The first one was a thermal-based method of wireless control of pneumatics using chemical reactions. The second one is an improvement to wireless technologies that can control electrical or thermal actuators without the need of a microcontroller or wireless communication, which is a major bottleneck of scalability for capsule robots.

The study introduces an untethered inflatable robotic capsule for tissue dilation, powered by a magnetic induction-driven chemical reaction for inflation, offering a novel approach to wirelessly controlling soft actuators. The model developed allows for predicting the actuation behaviour and help with designing capsules of various sizes for different applications. As a result of this study, a capsule capable of intestinal tissue dilation that can be sustained for 44 minutes was achieved. The capsule expanded from 16 mm to 35 mm, exerting 0.27 N of anchoring force in a pig intestine and crawling at $2.67\,\mathrm{mm\,s^{-1}}$ in an intestine phantom. The design can be considered safe for in vivo use, as the inflation method poses minimal patient risk, the chemicals used are safe for ingestion, the capsule uses no electronics on-board and the capsule exhibits a small error margin of 15.2-17.1%. As an outcome, the introduction of a dissolution medium to control the release of chemicals provides a new way to control chemical reactions for the pneumatic actuation of soft robots. This work provides a scalable and soft robot compliant alternative to electromechanical systems that end up with a large overall size [4] or systems using the liquid-to-gas boiling point transition as a source of pneumatic pressure [104, 105, 5, 6], which is hard to control the volume of gas with. The main drawback of this approach is that the chemical reaction used is non-reversible, only used for one inflation and deflation cycle.

The second part of the study introduces a new amplifier design, the PSRG, capable of superposing multiple sinusoidal magnetic fields. Unlike traditional designs, it bypasses the maximum and threshold gate-source voltage limitations at the input stage by superposing at the Tx coil instead, achieved with a modular design that works in parallel and has potential for expansion. The full amplifier design, along with its P-WPT performance and potential limitations for future designs, was presented. Tx/Rx analysis shows that the PSRG system can transmit six frequencies simultaneously within a 30-90 kHz range using a 5.44 μH Tx coil. When transmitting six frequencies, there is only a 30% reduction in current and 50% reduction in power received by the Rx load, compared to sending a single frequency, which is lower than what could be achieved with FM. The system delivers an average of 28.5 mA or 17 mW to six frequencies simultaneously with a Tx/Rx separation of 18.3 mm and an input voltage of 15 V.

There is a varying range of power requirements from the literature such as a current supply of 115 mA [39], more than 100 mW [135], to as low as 20 mW for capsule inspection only [58]. In most of the cases, the wireless power transfer is usually operated at much higher frequencies. One example uses a transmission frequency of 1 MHz to achieve 150 mW power transfer at 10 mm separation distance with a Tx coil current of 11 A [143] and another uses a frequency of 6.78 MHz to achieve 162 mW at 200 mm with a Tx coil current of 3.8 A [162]. A major difference from these examples is that majority of the cases are for wireless power transfer of a single frequency, which is much easier to amplify and transmit. This work still achieves its major goal of improving the wireless capabilities of multi-frequency wireless power transfer that aims to reduce electronic circuitry inside the capsule to reduce the overall size of the robot. One key takeaway from the literature is to alter the design for higher frequencies to improve the power transfer, given that higher frequencies at the same amplitude carry a higher amount of energy. Higher frequencies are harder to produce as the amplifier design becomes more susceptible to noise and current reflections and electromagnetic safety of the system should be taken into account.

The study explores several applications, including heating, lighting LEDs, and bidirectional motor control. The bidirectional motor test demonstrated that 4 frequencies, 2 passive circuits, and 4 Rx coils could independently control two small DC motors using the PSRG system. The heating test showed that temperatures sufficient for cell necrosis or cauterization could be reached, though the PTE needs improvement to extend the operational distance for GI tract applications that require a minimum of 30.9 mm [54]. The LED test confirmed that 6 frequencies can be transmitted at the same time without significant power loss, unlike FM, which would reduce LED luminosity or show visible flickering. Compared to existing literature, the system doubles the number of addressable components and introduces P-WPT capabilities [9, 120, 121]. A prototype capsule design was presented, capable of anchoring to intestinal tissue, controlling two DC motors for 2-DOF manipulation, and using a heater for cauterization or cell destruction. While the PTE needs improvement, this research provides a new platform and methodology for P-WPT, with Rx side analysis offering insight for the robot design.

5.2 Future Directions

Even though the general approach of on-board pneumatics and soft robotic actuators is a scalable solution, the chemical reaction used in this study is not reversible, which means for more complex actuation behaviour, a reversible chemical reaction or alternative methods should be sought out. As an immediate improvement, the deflation can be achieved quicker by other methods of CO_2 absorption such as actively cooling down the capsule or via a mechanical deflation mechanism. The chemical capsule may be reduced in size to fit a standard capsule size 000 by removing the hollow section or potentially if a reversible reaction is being used, the reversibility could be used to control the exact amount of gas in the capsule instead of using the gelatin. Additionally, using a theoretical simulation based on the physical properties of the final capsule and the methodology provided in Chapter 3, transmission of simple diagnostic data of the internals of the capsule, such as temperature, pressure or force on the outside of the capsule can be a good way of achieving closed-loop control.

The PSRG system compliments the wireless scalable soft actuator control by providing a method of controlling electrical and thermal power wirelessly without on-board computation or requirement for data transfer. Before practical applications can be tested however, the overall PTE of the P-WPT needs to be improved. The PSRG system can be improved by using lower resistance inductors for the CI-Array, modifications to the MOSFET routing circuit to allow a higher gate-source voltages, an optimisation of Tx/Rx relationship of the system, using higher range of frequencies for smaller Rx receivers, considerations and testing of other electrothermal actuators and potentially using magnetic resonance instead of inductive coupling could help improve the operation distance [136, 138]. Apart from operation distance, capsule size is still a big limitation, which may be alleviated with replacing DC motor with thermoresponsive actuators [89, 37, 95]. The surgical functionality may be improved with converting a CTE based precision instrument [8] to be powered wirelessly and implementing a closed-loop control system with a wireless sensor [137]. Inspection capsules that are already commercially available have dimensions that are already around the largest allowed capsule size [10]. Before the technology further develops in miniaturisation of inspection capsules and in efficient small scale actuators that may be suitable to be used as manipulators, self-assembly of multiple capsules in the stomach may be sought out to allow the inclusion of inspection capsules to the surgical ones. The capsule design provided can still form a 2-DOF manipulator with a maximum diameter of 11 mm, and since 2-DOF self assembling capsules have already been developed, it may be possible to convert the capsule design proposed into a self-assembling version. There are further challenges however, such as how to allow magnetic self-assembly to take place in the stomach while also allowing electrical connection between moving parts of the assembled pieces while insulating the electrical components to the outside of the capsule assembly, or re-designing the system to a higher frequency version to improve power transfer capabilities. Regardless of the future challenges, the work opens up the possibility of wirelessly controlling small scale capsule robots that may be able to carry out more complex therapeutic functions such as manipulation and cauterisation with minimal electronics on board.

References

[1] M. Simi, G. Gerboni, A. Menciassi, and P. Valdastri, “Magnetic torsion spring mechanism for a wireless biopsy capsule,” *Journal of Medical Devices*, vol. 7, no. 4, p. 041009, 09 2013. [Online]. Available: https://doi.org/10.1115/1.4025185

[2] D. Ye, J. Xue, S. Yuan, F. Zhang, S. Song, J. Wang, and M. Q.-H. Meng, “Design and control of a magnetically-actuated capsule robot with biopsy function,” *IEEE Transactions on Biomedical Engineering*, vol. 69, no. 9, pp. 2905–2915, 2022.

[3] Z. Nagy, R. Oung, J. J. Abbott, and B. J. Nelson, “Experimental investigation of magnetic self-assembly for swallowable modular robots,” in *2008 IEEE/RSJ International Conference on Intelligent Robots and Systems*, 2008, pp. 1915–1920.

[4] L. Yan, T. Wang, D. Liu, J. Peng, Z. Jiao, and C.-Y. Chen, “Capsule robot for obesity treatment with wireless powering and communication,” *IEEE Transactions on Industrial Electronics*, vol. 62, no. 2, pp. 1125–1133, 2015.

[5] Y. Tang, M. Li, T. Wang, X. Dong, W. Hu, and M. Sitti, “Wireless miniature magnetic phase-change soft actuators,” *Advanced Materials*, 2022.

[6] M. Boyvat, D. M. Vogt, and R. J. Wood, “Ultrastrong and high-stroke wireless soft actuators through liquid-gas phase change,” *Advanced Materials Technologies*, vol. 4, no. 2, p. 1800381, 2019. [Online]. Available: https://onlinelibrary.wiley.com/doi/abs/10.1002/admt.201800381

[7] S. Wu, Y. Hong, Y. Zhao, J. Yin, and Y. Zhu, “Caterpillar-inspired soft crawling robot with distributed programmable thermal actuation,” *Science Advances*, vol. 9, no. 12, p. eadf8014, 2023. [Online]. Available: https://www.science.org/doi/abs/10.1126/sciadv.adf8014

[8] M. E. M. K. Abdelaziz, J. Zhao, B. G. Rosa, H.-T. Lee, D. Simon, K. Vyas, B. Li, H. Koguna, Y. Li, A. A. Demircali, H. Uvet, G. Gencoglan, A. Akcay, M. Elriedy, J. Kinross, R. Dasgupta, Z. Takats, E. Yeatman, G.-Z. Yang, and B. Temelkuran, “Fiberbots: Robotic fibers for high-precision minimally invasive surgery,” *Science Advances*, vol. 10, no. 3, p. eadj1984, 2024. [Online]. Available: https://www.science.org/doi/abs/10.1126/sciadv.adj1984

[9] M. S. M. Ali and K. Takahata, “Wireless microfluidic control with integrated shape-memory-alloy actuators operated by field frequency modulation,” *Journal of Micromechanics and Microengineering*, vol. 21, no. 7, p. 075005, jun 2011. [Online]. Available: https://dx.doi.org/10.1088/0960-1317/21/7/075005

[10] W. Chen, J. Sui, and C. Wang, “Magnetically actuated capsule robots: A review,” *IEEE Access*, vol. 10, pp. 88 398–88 420, 2022.

[11] R. L. Siegel, K. D. Miller, N. S. Wagle, and A. Jemal, “Cancer statistics, 2023,” *CA: A Cancer Journal for Clinicians*, vol. 73, no. 1, pp. 17–48, 2023. [Online]. Available: https://acsjournals.onlinelibrary.wiley.com/doi/abs/10.3322/caac.21763

[12] M. F. Hale, R. Sidhu, and M. E. McAlindon, “Capsule endoscopy: current practice and future directions,” *World journal of gastroenterology*, vol. 20, no. 24, pp. 7752–7759, Jun 2014.

[13] S. N. Adler and Y. C. Metzger, “PillCam COLON capsule endoscopy: recent advances and new insights,” *Therapeutic Advances in Gastroenterology*, vol. 4, no. 4, pp. 265–268, Jul. 2011.

[14] N. K. Mandsberg, J. F. Christfort, K. Kamguyan, A. Boisen, and S. K. Srivastava, “Orally ingestible medical devices for gut engineering,” *Advanced Drug Delivery Reviews*, vol. 165-166, pp. 142–154, 2020.

[15] H.-L. Ching, M. F. Hale, and M. E. McAlindon, “Current and future role of magnetically assisted gastric capsule endoscopy in the upper gastrointestinal tract,” *Therapeutic Advances in Gastroenterology*, vol. 9, no. 3, pp. 313–321, 2016, pMID: 27134661. [Online]. Available: https://doi.org/10.1177/1756283X16633052

[16] S. Yim and M. Sitti, “Shape-programmable soft capsule robots for semi-implantable drug delivery,” *IEEE Transactions on Robotics*, vol. 28, no. 5, pp. 1198–1202, 2012.

[17] W. Yu, R. Rahimi, M. Ochoa, R. Pinal, and B. Ziaie, “A smart capsule with gi-tract-location-specific payload release,” *IEEE Transactions on Biomedical Engineering*, vol. 62, no. 9, pp. 2289–2295, 2015.

[18] O. Erin, M. Boyvat, J. Lazovic, M. E. Tiryaki, and M. Sitti, “Wireless mri-powered reversible orientation-locking capsule robot,” *Advanced Science*, vol. 8, no. 13, p. 2100463, 2021. [Online]. Available: https://onlinelibrary.wiley.com/doi/abs/10.1002/advs.202100463

[19] V. H. Le, H. L. Rodriguez, C. Lee, G. Go, J. Zhen, V. D. Nguyen, H. Choi, S. Y. Ko, J.-O. Park, and S. Park, “A soft-magnet-based drug-delivery module for active locomotive intestinal capsule endoscopy using an electromagnetic actuation system,” *Sensors and Actuators A: Physical*, vol. 243, pp. 81–89, 2016. [Online]. Available: https://www.sciencedirect.com/science/article/pii/S0924424716301194

[20] M. Beccani, G. Aiello, N. Gkotsis, H. Tunc, A. Taddese, E. Susilo, P. Völgyesi, Ákos Lédeczi, E. D. Momi, and P. Valdastri, “Component based design of a drug delivery capsule robot,” *Sensors and Actuators A: Physical*, vol. 245, pp. 180–188, 2016. [Online]. Available: https://www.sciencedirect.com/science/article/pii/S0924424716301807

[21] M. Rehan, I. Al-Bahadly, D. G. Thomas, W. Young, L. K. Cheng, and E. Avci, “Smart capsules for sensing and sampling the gut: status, challenges and prospects,” *Gut*, vol. 73, no. 1, pp. 186–202, 2024. [Online]. Available: https://gut.bmj.com/content/73/1/186

[22] Y. L. Kong, X. Zou, C. A. McCandler, A. R. Kirtane, S. Ning, J. Zhou, A. Abid, M. Jafari, J. Rogner, D. Minahan, J. E. Collins, S. McDonnell, C. Cleveland, T. Bensel, S. Tamang, G. Arrick, A. Gimbel, T. Hua, U. Ghosh, V. Soares, N. Wang, A. Wahane, A. Hayward, S. Zhang, B. R. Smith, R. Langer, and G. Traverso, "3d-printed gastric resident electronics," *Advanced Materials Technologies*, vol. 4, no. 3, p. 1800490, 2019.

[23] V. H. Le, V. D. Nguyen, C. Lee, G. Go, J.-O. Park, and S. Park, "Miniaturized biopsy module using gripper tool for active locomotive capsule endoscope," *Mechatronics*, vol. 44, pp. 52–59, 2017. [Online]. Available: https://www.sciencedirect.com/science/article/pii/S0957415817300582

[24] D. Ye, F. Zhang, S. Yuan, S. Song, and M. Q.-H. Meng, "Magnetically driven wireless capsule robot with targeting biopsy function," in *2019 IEEE International Conference on Robotics and Biomimetics (ROBIO)*, 2019, pp. 1222–1227.

[25] M. Rehan, I. Al-Bahadly, D. G. Thomas, and E. Avci, "Development of a robotic capsule for in vivo sampling of gut microbiota," *IEEE Robotics and Automation Letters*, vol. 7, no. 4, pp. 9517–9524, 2022.

[26] H. Rezaei Nejad, B. C. M. Oliveira, A. Sadeqi, A. Dehkharghani, I. Kondova, J. A. M. Langermans, J. S. Guasto, S. Tzipori, G. Widmer, and S. R. Sonkusale, "Ingestible osmotic pill for in vivo sampling of gut microbiomes," *Advanced Intelligent Systems*, vol. 1, no. 5, p. 1900053, 2019. [Online]. Available: https://onlinelibrary.wiley.com/doi/abs/10.1002/aisy.201900053

[27] F. Munoz, G. Alici, and W. Li, "A review of drug delivery systems for capsule endoscopy," *Advanced Drug Delivery Reviews*, vol. 71, pp. 77–85, 2014.

[28] S. Song, S. Yuan, F. Zhang, J. Su, D. Ye, J. Wang, and M. Q.-H. Meng, "Integrated design and decoupled control of anchoring and drug release for wireless capsule robots," *IEEE/ASME Transactions on Mechatronics*, vol. 27, no. 5, pp. 2897–2907, 2022.

[29] J. Gao and G. Yan, "Design and implementation of a clamper-based and motor-driven capsule robot powered by wireless power transmission," *IEEE Access*, vol. 7, pp. 138 151–138 161, 2019.

[30] W. Chen, Q. Ke, S. He, W. Luo, X. C. Ji, and G. Yan, "Experimental research on anchoring force in intestine for the motion of capsule robot," *Journal of Medical Engineering and Technology*, vol. 37, no. 5, pp. 334–341, 2013.

[31] B. H. K. Leung, C. C. Y. Poon, R. Zhang, Y. Zheng, C. K. W. Chan, P. W. Y. Chiu, J. Y. W. Lau, and J. J. Y. Sung, "A therapeutic wireless capsule for treatment of gastrointestinal haemorrhage by balloon tamponade effect," *IEEE Transactions on Biomedical Engineering*, vol. 64, no. 5, pp. 1106–1114, 2017.

[32] J. A. Vale, P. D. Miller, and R. S. Kirby, "Balloon dilatation of the prostate–should it have a place in the urologist's armamentarium?" *J R Soc Med*, vol. 86, no. 2, pp. 83–86, Feb. 1993.

[33] K. Sunada, H. Yamamoto, H. Kita, T. Yano, H. Sato, Y. Hayashi, T. Miyata, Y. Sekine, A. Kuno, M. Iwamoto, H. Ohnishi, K. Ido, and K. Sugano, "Clinical outcomes of enteroscopy using the double-balloon method for strictures of the small intestine," *World J Gastroenterol*, vol. 11, no. 7, pp. 1087–1089, Feb. 2005.

[34] Pasricha, T. Smith, B. F. ; Mitchell, V. R. ; Fang, B. Brooks, E. R. ; Gerding, J. S. ; Washington, M. K. Valdastri, P. Obstein, and K. L., "Controlled colonic insufflation by a remotely triggered capsule for improved mucosal visualization," *Endoscopy*, vol. 46, no. 07, pp. 614–618, Jun. 2014.

[35] P. Valdastri, M. Simi, and R. J. Webster, 3rd, "Advanced technologies for gastrointestinal endoscopy," *The Annual Reviews of Biomedical Engineering*, vol. 14, pp. 397–429, May 2012.

[36] M. Adami and A. Seibel, "On-board pneumatic pressure generation methods for soft robotics applications," *Actuators*, vol. 8, no. 1, 2019.

[37] A. L. Evenchik, A. Q. Kane, E. Oh, and R. L. Truby, "Electrically controllable materials for soft, bioinspired machines," *Annual Review of Materials Research*, vol. 53, no. Volume 53, 2023, pp. 225–251, 2023. [Online]. Available: https://www.annualreviews.org/content/journals/10.1146/annurev-matsci-080921-102916

[38] J. Jung, S. Shin, M. Li, and Y. T. Kim, "Telemetry transmission to support bidirectional communication for capsule endoscope using human body communication," *IEEE Microwave and Wireless Components Letters*, vol. 31, no. 7, pp. 905–908, 2021.

[39] R. Fontana, F. Mulana, C. Cavallotti, G. Tortora, M. Vigliar, M. Vatteroni, and A. Menciassi, "An innovative wireless endoscopic capsule with spherical shape," *IEEE Transactions on Biomedical Circuits and Systems*, vol. 11, no. 1, pp. 143–152, 2017.

[40] M. J. Christoe, J. Yuan, A. Michael, and K. Kalantar-Zadeh, "Bluetooth signal attenuation analysis in human body tissue analogues," *IEEE Access*, vol. 9, pp. 85 144–85 150, 2021.

[41] J. H. Palep, "Robotic assisted minimally invasive surgery," *Journal of Minimal Access Surgery*, vol. 5, no. 1, pp. 1–7, Jan. 2009.

[42] J. Huang, Z. Zhang, and S. Wang, "Efficacy of the da vinci surgical system in colorectal surgery comparing with traditional laparoscopic surgery or open surgery: A meta-analysis," *International Journal of Advanced Robotic Systems*, vol. 13, no. 5, p. 1729881416664849, 2016. [Online]. Available: https://doi.org/10.1177/1729881416664849

[43] T. Haidegger, S. Speidel, D. Stoyanov, and R. M. Satava, "Robot-assisted minimally invasive surgery—surgical robotics in the data age," *Proceedings of the IEEE*, vol. 110, no. 7, pp. 835–846, 2022.

[44] A. R. Lanfranco, A. E. Castellanos, J. P. Desai, and W. C. Meyers, "Robotic surgery: a current perspective," *Annals of Surgery*, vol. 239, no. 1, pp. 14–21, Jan. 2004.

[45] D. Jain, A. Goyal, and S. Zavala, "Predicting colonoscopy time: A quality improvement initiative," *Clinical Endoscopy*, vol. 49, no. 6, pp. 555–559, 2016.

[46] H. Kang and M. H. Thoufeeq, "Size of colorectal polyps determines time taken to remove them endoscopically," *Endoscopy International Open*, vol. 6, no. 5, pp. E610–E615, 2018.

[47] U. Akyuz and F. Akyuz, "Diagnostic and therapeutic capability of Double-Balloon enteroscopy in clinical practice," *Clin Endosc*, vol. 49, no. 2, pp. 157–160, Mar. 2016.

[48] S. R. Lieber, B. J. Heller, C. F. Martin, C. W. Howard, and S. Crockett, "Complications of anesthesia services in gastrointestinal endoscopic procedures," *Clinical Gastroenterology and Hepatology*, vol. 18, no. 9, pp. 2118–2127.e4, 2020. [Online]. Available: https://www.sciencedirect.com/science/article/pii/S1542356519311103

[49] R. M. Bonnor and K. A. Ludwig, "Laparoscopic colectomy for colon cancer: comparable to conventional oncologic surgery?" *Clin. Colon Rectal Surg.*, vol. 18, no. 3, pp. 174–181, aug 2005.

[50] K. Wang, J. Ma, F. Wang, Z. Wang, G. Yan, and Y. Zhou, "Full-driving soft robotic colonoscope in compliant colon tissue," *J. Med. Eng. Technol.*, vol. 41, no. 8, pp. 662–669, Nov. 2017.

[51] C. J. Fyock and P. V. Draganov, "Colonoscopic polypectomy and associated techniques," *World journal of gastroenterology*, vol. 16, no. 29, pp. 3630–3637, 2010.

[52] L. Liu, S. Towfighian, and A. Hila, "A review of locomotion systems for capsule endoscopy," *IEEE Reviews in Biomedical Engineering*, vol. 8, pp. 138–151, 2015.

[53] H. F. Helander and L. Fändriks, "Surface area of the digestive tract - revisited," *Scandinavian Journal of Gastroenterology*, vol. 49, no. 6, pp. 681–689, 2014.

[54] G. Kiran, I. Yilmaz, S. Aydin, F. Sanlikan, and E. Ozkaya, "The shortest distance between the skin and the peritoneal cavity is obtained with fascial elevation: a preliminary prospective laparoscopic entry study," *Facts Views Vis Obgyn*, vol. 14, no. 2, pp. 171–175, Jun. 2022.

[55] A. E. Deatsch and B. A. Evans, "Heating efficiency in magnetic nanoparticle hyperthermia," *Journal of Magnetism and Magnetic Materials*, vol. 354, pp. 163–172, 2014.

[56] A. Bhardwaj, K. Parekh, and N. Jain, "In vitro hyperthermic effect of magnetic fluid on cervical and breast cancer cells," *Scientific Reports*, vol. 10, no. 1, p. 15249, Sep 2020.

[57] P. R. Slawinski, K. L. Obstein, and P. Valdastri, "Capsule endoscopy of the future: What's on the horizon?" *World J Gastroenterol*, vol. 21, no. 37, pp. 10 528–10 541, Oct. 2015.

[58] Q. Cao, R. Deng, Y. Pan, R. Liu, Y. Chen, G. Gong, J. Zou, H. Yang, and D. Han, "Robotic wireless capsule endoscopy: recent advances and upcoming technologies," *Nature Communications*, vol. 15, no. 1, p. 4597, May 2024. [Online]. Available: https://doi.org/10.1038/s41467-024-49019-0

[59] A. Z. Taddese, P. R. Slawinski, K. L. Obstein, and P. Valdastri, “Closed loop control of a tethered magnetic capsule endoscope,” *Robot Sci Syst*, vol. 2016, Jun. 2016.

[60] S. Miyashita, S. Guitron, K. Yoshida, S. Li, D. D. Damian, and D. Rus, “Ingestible, controllable, and degradable origami robot for patching stomach wounds,” in *2016 IEEE International Conference on Robotics and Automation (ICRA)*, 2016, pp. 909–916.

[61] A. du Plessis d’Argentré, S. Perry, Y. Iwata, H. Iwasaki, E. Iwase, A. Fabozzo, I. Will, D. Rus, D. D. Damian, and S. Miyashita, “Programmable medicine: Autonomous, ingestible, deployable hydrogel patch and plug for stomach ulcer therapy,” in *2018 IEEE International Conference on Robotics and Automation (ICRA)*, 2018, pp. 1511–1518.

[62] Y. Shi, G. Yan, W. Chen, and B. Zhu, “Micro-intestinal robot with wireless power transmission: design, analysis and experiment,” *Computers in Biology and Medicine*, vol. 66, pp. 343–351, 2015. [Online]. Available: https://www.sciencedirect.com/science/article/pii/S0010482515002036

[63] K. Wang, G. Yan, G. Ma, and D. Ye, “An earthworm-like robotic endoscope system for human intestine: Design, analysis, and experiment,” *Annals of Biomedical Engineering*, vol. 37, no. 1, pp. 210–221, Jan 2009. [Online]. Available: https://doi.org/10.1007/s10439-008-9597-6

[64] R. A. Ganz, J. Viveiros, A. Ahmad, A. Ahmadi, A. Khalil, M. J. Tolkoff, N. S. Nishioka, and M. R. Hamblin, “Helicobacter pylori in patients can be killed by visible light,” *Lasers in Surgery and Medicine*, vol. 36, no. 4, pp. 260–265, 2005. [Online]. Available: https://onlinelibrary.wiley.com/doi/abs/10.1002/lsm.20161

[65] G. Tortora, B. Orsini, P. Pecile, A. Menciassi, F. Fusi, and G. Romano, “An ingestible capsule for the photodynamic therapy of helicobacter pylori infection,” *IEEE/ASME Transactions on Mechatronics*, vol. 21, no. 4, pp. 1935–1942, 2016.

[66] Q. Tang, G. Jin, G. Wang, T. Liu, X. Liu, B. Wang, and H. Cao, “Current sampling methods for gut microbiota: A call for more precise devices,” *Frontiers in Cellular and Infection Microbiology*, vol. 10, 2020. [Online]. Available: https://www.frontiersin.org/journals/cellular-and-infection-microbiology/articles/10.3389/fcimb.2020.00151

[67] J. Wang, M. Leach, E. G. Lim, Z. Wang, R. Pei, and Y. Huang, “An implantable and conformal antenna for wireless capsule endoscopy,” *IEEE Antennas and Wireless Propagation Letters*, vol. 17, no. 7, pp. 1153–1157, 2018.

[68] P. R. Slawinski, K. L. Obstein, and P. Valdastri, “Emerging issues and future developments in capsule endoscopy,” *Techniques in Gastrointestinal Endoscopy*, vol. 17, no. 1, pp. 40–46, 2015.

[69] B. Boyd, K. Esendag, S. Miyashita, and D. D. Damian, “Development of a near-field wireless power transfer system for controlling electronic motors within capsule endoscopes,” in *Hamlyn Symposium on Medical Robotics 2024*, vol. 16, June 2024, pp. 95–96.

[70] Z. Li, M. C. Hoang, C.-S. Kim, E. Choi, D. Bang, J.-O. Park, and B. Kang, “Modular capsules with assembly and separation mechanism: Proof of concept,” *Actuators*, vol. 10, no. 7, 2021. [Online]. Available: https://www.mdpi.com/2076-0825/10/7/159

[71] F. Peker and O. Ferhanoğlu, “Multi-capsule endoscopy: An initial study on modeling and phantom experimentation of a magnetic capsule train,” *Journal of Medical and Biological Engineering*, vol. 41, no. 3, pp. 315–321, Jun 2021. [Online]. Available: https://doi.org/10.1007/s40846-021-00610-6

[72] J. Guo, P. Liu, S. Guo, L. Wang, and G. Sun, “Development of a novel wireless spiral capsule robot with modular structure,” in *2017 IEEE International Conference on Mechatronics and Automation (ICMA)*, 2017, pp. 439–444.

[73] X. Ma, D. E. Vogtmann, and S. Bergbreiter, “Dynamics and scaling of magnetically folding multi-material structures,” *2016 IEEE International Conference on Robotics and Automation (ICRA)*, pp. 1899–1906, 2016. [Online]. Available: https://api.semanticscholar.org/CorpusID:17929579

[74] H. Suzuki and R. J. Wood, “Origami-inspired miniature manipulator for teleoperated microsurgery,” *Nature Machine Intelligence*, vol. 2, no. 8, pp. 437–446, 2020.

[75] J. Liu, X. Chen, Q. Lahondes, K. Esendag, D. Damian, and S. Miyashita, “Origami robot self-folding by magnetic induction,” in *2022 IEEE/RSJ International Conference on Intelligent Robots and Systems (IROS)*, 2022, pp. 2519–2525.

[76] J. Han, D. Rus, and S. Miyashita, “Roblets: Robotic tablets that self-assemble and self-fold into a robot,” in *2023 IEEE/RSJ International Conference on Intelligent Robots and Systems (IROS)*, 2023, pp. 4709–4714.

[77] M. P. Kummer, J. J. Abbott, B. E. Kratochvil, R. Borer, A. Sengul, and B. J. Nelson, “Octomag: An electromagnetic system for 5-dof wireless micromanipulation,” *IEEE Transactions on Robotics*, vol. 26, no. 6, pp. 1006–1017, 2010.

[78] K. Esendag, M. E. McAlindon, D. Rus, S. Miyashita, and D. D. Damian, “Development of an untethered inflatable capsule robot for stricture dilation - a preliminary study,” in *Hamlyn Symposium on Medical Robotics 2023*, vol. 15, June 2023, pp. 101–102.

[79] O. Onaizah and E. Diller, “Tetherless mobile micro-surgical scissors using magnetic actuation,” in *2019 International Conference on Robotics and Automation (ICRA)*, 2019, pp. 894–899.

[80] A. Lim, A. Schonewille, C. Forbrigger, T. Looi, J. Drake, and E. Diller, “Design and comparison of magnetically-actuated dexterous forceps instruments for neuroendoscopy,” *IEEE Transactions on Biomedical Engineering*, vol. 68, no. 3, pp. 846–856, 2021.

[81] S. Guitron, A. Guha, S. Li, and D. Rus, “Autonomous locomotion of a miniature, untethered origami robot using hall effect sensor-based magnetic localization,” in *2017 IEEE International Conference on Robotics and Automation (ICRA)*, 2017, pp. 4807–4813.

[82] J. Liu, H. Sugiyama, T. Nakayama, and S. Miyashita, “Magnetic sensor based topographic localization for automatic dislocation of ingested button battery,” in *2020 IEEE International Conference on Robotics and Automation (ICRA)*, 2020, pp. 5488–5494.

[83] D. Wang, B. Zhao, X. Li, L. Dong, M. Zhang, J. Zou, and G. Gu, “Dexterous electrical-driven soft robots with reconfigurable chiral-lattice foot design,” *Nature Communications*, vol. 14, no. 1, p. 5067, Aug 2023. [Online]. Available: https://doi.org/10.1038/s41467-023-40626-x

[84] A. Wiranata, M. Kanno, N. Chiya, H. Okabe, T. Horii, T. Fujie, N. Hosoya, and S. Maeda, “High-frequency oscillations of low-voltage dielectric elastomer actuators,” *Applied Physics Express*, vol. 15, 12 2021.

[85] S. Rahmanian, A. Alibakhshi, H. Mouharrar, J. M. Benitez, and F. J. Montáns, “Low-voltage dielectric elastomer actuators by electro-mechanical resonance syntonization,” *International Journal of Mechanical Sciences*, vol. 263, p. 108758, 2024. [Online]. Available: https://www.sciencedirect.com/science/article/pii/S0020740323006604

[86] S. Wu, G. L. Baker, J. Yin, and Y. Zhu, “Fast thermal actuators for soft robotics,” *Soft Robotics*, vol. 9, no. 6, pp. 1031–1039, 2022, pMID: 34874763. [Online]. Available: https://doi.org/10.1089/soro.2021.0080

[87] Y. Wu, J. K. Yim, J. Liang, Z. Shao, M. Qi, J. Zhong, Z. Luo, X. Yan, M. Zhang, X. Wang, R. S. Fearing, R. J. Full, and L. Lin, “Insect-scale fast moving and ultrarobust soft robot,” *Science Robotics*, vol. 4, no. 32, p. eaax1594, 2019. [Online]. Available: https://www.science.org/doi/abs/10.1126/scirobotics.aax1594

[88] S. M. Felton, K. P. Becker, D. M. Aukes, and R. J. Wood, “Self-folding with shape memory composites at the millimeter scale,” *Journal of Micromechanics and Microengineering*, vol. 25, no. 8, p. 085004, jul 2015. [Online]. Available: https://dx.doi.org/10.1088/0960-1317/25/8/085004

[89] N. Sabahi, W. Chen, C.-H. Wang, J. J. Kruzic, and X. Li, “A review on additive manufacturing of shape-memory materials for biomedical applications,” *JOM*, vol. 72, no. 3, pp. 1229–1253, Mar 2020. [Online]. Available: https://doi.org/10.1007/s11837-020-04013-x

[90] M.-S. Kim, J.-K. Heo, H. Rodrigue, H.-T. Lee, S. Pané, M.-W. Han, and S.-H. Ahn, “Shape memory alloy (sma) actuators: The role of material, form, and scaling effects,” *Advanced Materials*, vol. 35, no. 33, p. 2208517, 2023. [Online]. Available: https://onlinelibrary.wiley.com/doi/abs/10.1002/adma.202208517

[91] W. Huang, Z. Ding, C. Wang, J. Wei, Y. Zhao, and H. Purnawali, “Shape memory materials,” *Materials Today*, vol. 13, no. 7, pp. 54–61, 2010. [Online]. Available: https://www.sciencedirect.com/science/article/pii/S1369702110701280

[92] K. Wang, H. Si, Q. Wan, Z. Wang, A. Qin, and B. Z. Tang, “Luminescent two-way reversible shape memory polymers prepared by hydroxyl–yne click polymerization,” *J. Mater. Chem. C*, vol. 8, pp. 16 121–16 128, 2020. [Online]. Available: http://dx.doi.org/10.1039/D0TC03888A

[93] R. Regmi, S. R. Bhattarai, C. Sudakar, A. S. Wani, R. Cunningham, P. P. Vaishnava, R. Naik, D. Oupicky, and G. Lawes, “Hyperthermia controlled rapid drug release from thermosensitive magnetic microgels,” *J. Mater. Chem.*, vol. 20, pp. 6158–6163, 2010. [Online]. Available: http://dx.doi.org/10.1039/C0JM00844C

[94] F. G. Downs, D. J. Lunn, M. J. Booth, J. B. Sauer, W. J. Ramsay, R. G. Klemperer, C. J. Hawker, and H. Bayley, “Multi-responsive hydrogel structures from patterned droplet networks,” *Nature Chemistry*, vol. 12, no. 4, pp. 363–371, Apr 2020. [Online]. Available: https://doi.org/10.1038/s41557-020-0444-1

[95] Y. S. Kim, M. Liu, Y. Ishida, Y. Ebina, M. Osada, T. Sasaki, T. Hikima, M. Takata, and T. Aida, “Thermoresponsive actuation enabled by permittivity switching in an electrostatically anisotropic hydrogel,” *Nature Materials*, vol. 14, no. 10, pp. 1002–1007, Oct 2015. [Online]. Available: https://doi.org/10.1038/nmat4363

[96] M. Santhamoorthy, T. T. Vy Phan, V. Ramkumar, C. J. Raorane, K. Thirupathi, and S.-C. Kim, “Thermo-sensitive poly (n-isopropylacrylamide-co-polyacrylamide) hydrogel for ph-responsive therapeutic delivery,” *Polymers*, vol. 14, no. 19, 2022. [Online]. Available: https://www.mdpi.com/2073-4360/14/19/4128

[97] S. M. Mirvakili and R. Langer, “Wireless on-demand drug delivery,” *Nature Electronics*, vol. 4, no. 7, pp. 464–477, 2021.

[98] C. Löwenberg, M. Balk, C. Wischke, M. Behl, and A. Lendlein, “Shape-memory hydrogels: Evolution of structural principles to enable shape switching of hydrophilic polymer networks,” *Accounts of Chemical Research*, vol. 50, no. 4, pp. 723–732, 2017. [Online]. Available: https://doi.org/10.1021/acs.accounts.6b00584

[99] A. Razmjou, M. R. Barati, G. P. Simon, K. Suzuki, and H. Wang, “Fast deswelling of nanocomposite polymer hydrogels via magnetic field-induced heating for emerging fo desalination,” *Environmental Science & Technology*, vol. 47, no. 12, pp. 6297–6305, 2013, pMID: 23663180. [Online]. Available: https://doi.org/10.1021/es4005152

[100] Y. Liu, B. Shaw, M. D. Dickey, and J. Genzer, “Sequential self-folding of polymer sheets,” *Science Advances*, vol. 3, no. 3, p. e1602417, 2017. [Online]. Available: https://www.science.org/doi/abs/10.1126/sciadv.1602417

[101] M. Boyvat and M. Sitti, “Remote modular electronics for wireless magnetic devices,” *Advanced Science*, vol. 8, no. 17, p. 2101198, 2021. [Online]. Available: https://onlinelibrary.wiley.com/doi/abs/10.1002/advs.202101198

[102] J. Baltrusaitis and V. H. Grassian, “Carbonic acid formation from reaction of carbon dioxide and water coordinated to al(oh)3: A quantum chemical study,” *The Journal of Physical Chemistry A*, vol. 114, no. 6, pp. 2350–2356, 2010.

[103] V. Vallem, E. Roosa, T. Ledinh, S. Rashid Nadimi, A. Kiani, and M. D. Dickey, “Soft electrochemical bubble actuator with liquid metal electrode using an embodied hydrogel pneumatic source,” *Soft Matter*, vol. 18, pp. 9291–9298, 2022. [Online]. Available: http://dx.doi.org/10.1039/D2SM00874B

[104] S. M. Mirvakili, D. Sim, I. W. Hunter, and R. Langer, "Actuation of untethered pneumatic artificial muscles and soft robots using magnetically induced liquid-to-gas phase transitions," *Science Robotics*, vol. 5, no. 41, 2020.

[105] S. Hirai, T. Nagatomo, T. Hiraki, H. Ishizuka, Y. Kawahara, and N. Miki, "Micro elastic pouch motors: Elastically deformable and miniaturized soft actuators using liquid-to-gas phase change," *IEEE Robotics and Automation Letters*, vol. 6, no. 3, pp. 5373–5380, 2021.

[106] S. T. Brittain, O. J. A. Schueller, H. Wu, S. Whitesides, and G. M. Whitesides, "Microorigami: Fabrication of small, three-dimensional, metallic structures," *The Journal of Physical Chemistry B*, vol. 105, no. 2, pp. 347–350, 2001. [Online]. Available: https://doi.org/10.1021/jp002556e

[107] T. Tachi, "Origamizer," 2010, accessed on October 31, 2024. [Online]. Available: www.tsg.ne.jp/TT/software/

[108] ——, "Origamizing polyhedral surfaces," *IEEE transactions on visualization and computer graphics*, vol. 16, pp. 298–311, 03 2010.

[109] E. D. Demaine, M. L. Demaine, D. Koschitz, and T. Tachi, "Curved crease folding - a review on art, design and mathematics," in *Semantic Scholar*, 2011. [Online]. Available: https://api.semanticscholar.org/CorpusID:15416501

[110] N. Benbernou, E. D. Demaine, M. L. Demaine, and A. Ovadya, "A universal crease pattern for folding orthogonal shapes," 2009. [Online]. Available: https://arxiv.org/abs/0909.5388

[111] T. Tachi, "3d origami design based on tucking molecule," in *Semantic Scholar*, 2008. [Online]. Available: https://api.semanticscholar.org/CorpusID:15986677

[112] A. Yellowhorse and L. L. Howell, "Creating rigid foldability to enable mobility of origami-inspired mechanisms," *Journal of Mechanisms and Robotics*, vol. 8, no. 1, p. 011011, 08 2015. [Online]. Available: https://doi.org/10.1115/1.4029923

[113] K. Miura, "Method of packaging and deployment of large membranes in space," in *Semantic Scholar*, 1985. [Online]. Available: https://api.semanticscholar.org/CorpusID:109375609

[114] D. Rus and M. T. Tolley, "Design, fabrication and control of origami robots," *Nature Reviews Materials*, vol. 3, no. 6, pp. 101–112, Jun 2018. [Online]. Available: https://doi.org/10.1038/s41578-018-0009-8

[115] D. A. McAdams and W. Li, "A novel method to design and optimize flat-foldable origami structures through a genetic algorithm," *Journal of Computing and Information Science in Engineering*, vol. 14, no. 3, p. 031008, 06 2014. [Online]. Available: https://doi.org/10.1115/1.4026509

[116] J. T. Overvelde, T. A. de Jong, Y. Shevchenko, S. A. Becerra, G. M. Whitesides, J. C. Weaver, C. Hoberman, and K. Bertoldi, "A three-dimensional actuated origami-inspired transformable metamaterial with multiple degrees of freedom,"

Nature Communications, vol. 7, no. 1, p. 10929, Mar 2016. [Online]. Available: https://doi.org/10.1038/ncomms10929

[117] S. Wu, Q. Ze, J. Dai, N. Udipi, G. H. Paulino, and R. Zhao, "Stretchable origami robotic arm with omnidirectional bending and twisting," *Proceedings of the National Academy of Sciences*, vol. 118, no. 36, p. e2110023118, 2021. [Online]. Available: https://www.pnas.org/doi/abs/10.1073/pnas.2110023118

[118] J. Liu, X. Chen, Q. Lahondes, K. Esendag, D. Damian, and S. Miyashita, "Origami robot self-folding by magnetic induction," in *2022 IEEE/RSJ International Conference on Intelligent Robots and Systems (IROS)*, 2022, pp. 2519–2525.

[119] S. Miyashita, S. Guitron, M. Ludersdorfer, C. R. Sung, and D. Rus, "An untethered miniature origami robot that self-folds, walks, swims, and degrades," in *2015 IEEE International Conference on Robotics and Automation (ICRA)*, 2015, pp. 1490–1496.

[120] K. Zhu, H. Nii, O. N. N. Fernando, and A. D. Cheok, "Selective inductive powering system for paper computing," in *Proceedings of the 8th International Conference on Advances in Computer Entertainment Technology*, ser. ACE '11. New York, NY, USA: Association for Computing Machinery, 2011. [Online]. Available: https://doi.org/10.1145/2071423.2071497

[121] M. Boyvat, J.-S. Koh, and R. J. Wood, "Addressable wireless actuation for multijoint folding robots and devices," *Science Robotics*, vol. 2, no. 8, p. eaan1544, 2017. [Online]. Available: https://www.science.org/doi/abs/10.1126/scirobotics.aan1544

[122] J. O. Jacobsen, B. G. Winder, L. L. Howell, and S. P. Magleby, "Lamina emergent mechanisms and their basic elements," *Journal of Mechanisms and Robotics*, vol. 2, no. 1, p. 011003, 11 2009. [Online]. Available: https://doi.org/10.1115/1.4000523

[123] P. S. Gollnick, S. P. Magleby, and L. L. Howell, "An introduction to multilayer lamina emergent mechanisms," *Journal of Mechanical Design*, vol. 133, no. 8, p. 081006, 08 2011. [Online]. Available: https://doi.org/10.1115/1.4004542

[124] I. L. Delimont, S. P. Magleby, and L. L. Howell, "Evaluating compliant hinge geometries for origami-inspired mechanisms," *Journal of Mechanisms and Robotics*, vol. 7, no. 1, p. 011009, 02 2015. [Online]. Available: https://doi.org/10.1115/1.4029325

[125] H. Shigemune, S. Maeda, Y. Hara, and S. Hashimoto, "Design of paper mechatronics: Towards a fully printed robot," in *2014 IEEE/RSJ International Conference on Intelligent Robots and Systems*, 2014, pp. 536–541.

[126] H. Shigemune, S. Maeda, Y. Hara, N. Hosoya, and S. Hashimoto, "Origami robot: A self-folding paper robot with an electrothermal actuator created by printing," *IEEE/ASME Transactions on Mechatronics*, vol. 21, no. 6, pp. 2746–2754, 2016.

[127] Y. Li, R. Torah, S. Beeby, and J. Tudor, "An all-inkjet printed flexible capacitor on a textile using a new poly(4-vinylphenol) dielectric ink for wearable applications," in *SENSORS, 2012 IEEE*, 2012, pp. 1–4.

[128] K. Myny, S. Smout, M. Rockelé, A. Bhoolokam, T. H. Ke, S. Steudel, B. Cobb, A. Gulati, F. G. Rodriguez, K. Obata, M. Marinkovic, D.-V. Pham, A. Hoppe, G. H. Gelinck, J. Genoe, W. Dehaene, and P. Heremans, "A thin-film microprocessor with inkjet print-programmable memory," *Scientific Reports*, vol. 4, no. 1, p. 7398, Dec 2014. [Online]. Available: https://doi.org/10.1038/srep07398

[129] H. Yasuda, T. Tachi, M. Lee, and J. Yang, "Origami-based tunable truss structures for non-volatile mechanical memory operation," *Nature Communications*, vol. 8, no. 1, p. 962, Oct 2017. [Online]. Available: https://doi.org/10.1038/s41467-017-00670-w

[130] S. Miyashita, L. Meeker, M. Go¨ldi, Y. Kawahara, and D. Rus, "Self-folding printable elastic electric devices: Resistor, capacitor, and inductor," in *2014 IEEE International Conference on Robotics and Automation (ICRA)*, 2014, pp. 1446–1453.

[131] S. Critcher and T. J. Freeborn, "Flexible pcb failures from dynamic activity and their impacts on bioimpedance measurements: A wearable case study," *IEEE Open Journal of Circuits and Systems*, vol. 2, pp. 732–742, 2021.

[132] S.-W. Hwang, H. Tao, D.-H. Kim, H. Cheng, J.-K. Song, E. Rill, M. A. Brenckle, B. Panilaitis, S. M. Won, Y.-S. Kim, Y. M. Song, K. J. Yu, A. Ameen, R. Li, Y. Su, M. Yang, D. L. Kaplan, M. R. Zakin, M. J. Slepian, Y. Huang, F. G. Omenetto, and J. A. Rogers, "A physically transient form of silicon electronics," *Science*, vol. 337, no. 6102, pp. 1640–1644, 2012. [Online]. Available: https://www.science.org/doi/abs/10.1126/science.1226325

[133] U.S. Food and Drug Administration, "Code of federal regulations, title 21, volume 6, section 582.1431," 2024.

[134] G.-Z. Yang, J. Bellingham, P. E. Dupont, P. Fischer, L. Floridi, R. Full, N. Jacobstein, V. Kumar, M. McNutt, R. Merrifield, B. J. Nelson, B. Scassellati, M. Taddeo, R. Taylor, M. Veloso, Z. L. Wang, and R. Wood, "The grand challenges of <i>science robotics</i>," *Science Robotics*, vol. 3, no. 14, p. eaar7650, 2018. [Online]. Available: https://www.science.org/doi/abs/10.1126/scirobotics.aar7650

[135] J. Gao, S. Tian, C. Yuan, Z. Ma, C. Gao, G. Yan, R. Li, Q. Tan, and L. Zhang, "Design and optimization of a novel double-layer helmholtz coil for wirelessly powering a capsule robot," *IEEE Transactions on Power Electronics*, vol. 39, no. 1, pp. 1826–1839, 2024.

[136] S. R. Khan, S. K. Pavuluri, G. Cummins, and M. P. Y. Desmulliez, "Wireless power transfer techniques for implantable medical devices: A review," *Sensors*, vol. 20, no. 12, 2020.

[137] S. R. Ruth, M. gu Kim, H. Oda, Z. Wang, Y. Khan, J. Chang, P. M. Fox, and Z. Bao, "Post-surgical wireless monitoring of arterial health progression," *iScience*, vol. 24, no. 9, p. 103079, 2021. [Online]. Available: https://www.sciencedirect.com/science/article/pii/S2589004221010476

[138] K. Obaideen, L. Albasha, U. Iqbal, and H. Mir, "Wireless power transfer: Applications, challenges, barriers, and the role of ai in achieving sustainable development goals - a bibliometric analysis," *Energy Strategy Reviews*, vol. 53, p. 101376, 2024. [Online]. Available: https://www.sciencedirect.com/science/article/pii/S2211467X2400083X

[139] K. Na, H. Jang, H. Ma, and F. Bien, "Tracking optimal efficiency of magnetic resonance wireless power transfer system for biomedical capsule endoscopy," *IEEE Transactions on Microwave Theory and Techniques*, vol. 63, no. 1, pp. 295–304, 2015.

[140] J. Zhiwei, Y. Guozheng, Jiangpingping, W. Zhiwu, and L. Hua, "Efficiency optimization of wireless power transmission systems for active capsule endoscopes," *Physiological Measurement*, vol. 32, no. 10, p. 1561, aug 2011. [Online]. Available: https://dx.doi.org/10.1088/0967-3334/32/10/005

[141] Y. Palagani, K. Mohanarangam, J. H. Shim, and J. R. Choi, "Wireless power transfer analysis of circular and spherical coils under misalignment conditions for biomedical implants," *Biosensors and Bioelectronics*, vol. 141, p. 111283, 2019. [Online]. Available: https://www.sciencedirect.com/science/article/pii/S0956566319303422

[142] Z. Jia, G. Yan, Y. Shi, and B. Zhu, "A wireless power transmission system for an active capsule endoscope for colon inspection," *J. Med. Eng. Technol.*, vol. 36, no. 5, pp. 235–241, Jul. 2012.

[143] B. Lenaerts and R. Puers, "An inductive power link for a wireless endoscope," *Biosensors and Bioelectronics*, vol. 22, no. 7, pp. 1390–1395, 2007. [Online]. Available: https://www.sciencedirect.com/science/article/pii/S0956566306002892

[144] M. R. Basar, M. Y. Ahmad, J. Cho, and F. Ibrahim, "An improved wearable resonant wireless power transfer system for biomedical capsule endoscope," *IEEE Transactions on Industrial Electronics*, vol. 65, no. 10, pp. 7772–7781, 2018.

[145] S. R. Khan, S. K. Pavuluri, G. Cummins, and M. P. Y. Desmulliez, "Miniaturized 3-d cross-type receiver for wirelessly powered capsule endoscopy," *IEEE Transactions on Microwave Theory and Techniques*, vol. 67, no. 5, pp. 1985–1993, 2019.

[146] S. Aldhaher, P. C. K. Luk, and J. F. Whidborne, "Wireless power transfer using class e inverter with saturable dc-feed inductor," in *2013 IEEE Energy Conversion Congress and Exposition*, 2013, pp. 1902–1909.

[147] H. Liu, Q. Shao, and X. Fang, "Modeling and optimization of class-e amplifier at subnominal condition in a wireless power transfer system for biomedical implants," *IEEE Transactions on Biomedical Circuits and Systems*, vol. 11, no. 1, pp. 35–43, 2017.

[148] J. Wu, C. Zhao, Z. Lin, J. Du, Y. Hu, and X. He, "Wireless power and data transfer via a common inductive link using frequency division multiplexing," *IEEE Transactions on Industrial Electronics*, vol. 62, no. 12, pp. 7810–7820, 2015.

[149] P. Wang, Y. Sun, X. Li, and Z. Ye, "An optimization method for simultaneous wireless power and data transfer systems," *Electronics*, vol. 9, no. 12, 2020. [Online]. Available: https://www.mdpi.com/2079-9292/9/12/2073

[150] H. Wang and J. Xu, "Research on the efficiency of multiphase wireless power transfer system with phase-shift control and magnetic field superposition," *International Journal of Electronics*, vol. 108, no. 4, pp. 636–646, 2021. [Online]. Available: https://doi.org/10.1080/00207217.2020.1793410

[151] A. Abramson, E. Caffarel-Salvador, V. Soares, D. Minahan, R. Y. Tian, X. Lu, D. Dellal, Y. Gao, S. Kim, J. Wainer, J. Collins, S. Tamang, A. Hayward, T. Yoshitake, H.-C. Lee, J. Fujimoto, J. Fels, M. R. Frederiksen, N. Rahbek, Ulrikand Roxhed, R. Langer, and G. Traverso, "A luminal unfolding microneedle injector for oral delivery of macromolecules," *Nature Medicine*, vol. 25, no. 10, pp. 1512–1518, Oct 2019.

[152] U.S. Food and Drug Administration, "Code of federal regulations, title 21, volume 3, section 184.1033," 1994.

[153] ——, "Code of federal regulations, title 21, volume 3, section 184.1736," 1983.

[154] F. Fiorillo, *Soft Magnetic Materials in Characterization and Measurement of Magnetic Materials*. Elsevier, 2004.

[155] H. B. Bohidar, "Hydrodynamic properties of gelatin in dilute solutions," *Int. J. Biol. Macromol.*, vol. 23, no. 1, pp. 1–6, Jul. 1998.

[156] J. Kestin, M. Sokolov, and W. A. Wakeham, "Viscosity of liquid water in the range -8 °c to 150 °c," *Journal of Physical and Chemical Reference Data*, vol. 7, no. 3, pp. 941–948, 1978.

[157] B. T. Smith, *Solubility and Dissolution in Remington Education: Physical Pharmacy*. London: Pharmaceutical Press, 2016.

[158] W. J. Bae, J. B. Choi, K. S. Kim, S. J. Kim, H. J. Cho, U. S. Ha, S. H. Hong, J. Y. Lee, and S. W. Kim, "Ab168. evaluation of the biocompatibility of packing materials for a catheter," *Translational Andrology and Urology*, vol. 4, no. Suppl 1, 2015.

[159] Y. Yang, J. Wang, L. Wang, Q. Wu, L. Ling, Y. Yang, S. Ning, Y. Xie, Q. Cao, L. Li, J. Liu, Q. Ling, and J. Zang, "Magnetic soft robotic bladder for assisted urination," *Science Advances*, vol. 8, no. 34, 2022.

[160] H. Yuk, C. E. Varela, C. S. Nabzdyk, X. Mao, R. F. Padera, E. T. Roche, and X. Zhao, "Dry double-sided tape for adhesion of wet tissues and devices," *Nature*, vol. 575, no. 7781, pp. 169–174, Nov 2019.

[161] H. Tang and M. Mayersohn, "Porcine prediction of pharmacokinetic parameters in people: A pig in a poke?" *Drug Metabolism and Disposition*, vol. 46, no. 11, pp. 1712–1724, 2018.

[162] G. Bandini, A. Buffi, M. Marracci, B. Tellini, T. Rizzo, M. Macucci, S. Strangio, and G. Iannaccone, "Electromagnetic design of an inductive wireless power transfer system for endoscopic capsule," in *2023 IEEE International Instrumentation and Measurement Technology Conference (I2MTC)*, 2023, pp. 1–6.